



POLITECNICO DI MILANO
DEPARTMENT OF PHYSICS
DOCTORAL PROGRAMME IN PHYSICS

CALCIUM IMAGING BY LIGHT SHEET FLUORESCENCE MICROSCOPY

Doctoral Dissertation of:
Alessia Candeo

Supervisor:
Prof. Cosimo D'Andrea

Tutor:
Prof. Paola Taroni

The Chair of the Doctoral Program:
Prof. Paola Taroni

11th March 2016 – XXVIII cycle

*The eye of a human being is a microscope,
which makes the world seem bigger than it really is.*

Khalil Gibran

Acknowledgment

I WOULD LIKE TO THANK who gave me the possibility to do this PhD. Cosimo D'Andrea, for being my supervisor and especially teaching me a lot about time resolved spectroscopy, and Paola Taroni for being my tutor and organizing the PhD program. I am strongly in debt with Andrea Bassi for introducing me to the light sheet microscopy, for picking me up randomly one day and working with me from then on, always promoting me. With Gianluca Valentini, for always being helpful and for supporting me, with his patience, kindness and exaggerate knowledge. You both have my deep gratitude. I am grateful to all the external people I have collaborated with during these years. Alex Costa is for sure the best collaborator ever, he thought me everything I know about plant biology without him even realizing it. Thanks also to Gandolfo, who is now working with the light sheet setup. A special thank goes to German Sumbre, who welcomed me from the first day, and all his team in Paris which made me discover a whole new field. I want to especially thank Adrien Jouary, who worked together with me, thought me and was my mentor in the Parisian lab, Jonathan Boulanger-Weill and Selma Mehyaoui who helped with the softwares. I hope to work and hang out with you guys again. I would like to thank the people that spent these 3 years with me in the department. Firstly, my office mates, Luca, Rebecca, Lucia, Valentina and Edoardo. Thanks for all the advice, the discussions, the fights, the laughs. Edo and Vale, a special thank you for the amazing lunches! And of course the people of the office next door, Laura, Sara, Sara, Sanathana and all the others. Thanks also to the people from the administration and the technicians, who somehow helped in this PhD. Of course, I want to thank all the people that supported me in a way or another in this adventure, my friends, among which Petra stands, and all my family, mom and dad in particular, that always stayed by my side.

Milano, March 2016
Alessia Candeo

Abstract

OVER THE LAST DECADES there has been an impressive progression in optical microscopy to explore fundamental issues in life science. The understanding of complex phenomena like the mechanisms of calcium signalling requires a multiscale method, to be applied from cells to organs in physiological condition, with minimum damage for the sample. An innovative approach for the field was provided by Light Sheet Fluorescence Microscopy (LSFM), a technique that introduces optical sectioning in wide-field microscopy.

In the following work, an overview of the main calcium pathways is presented, along with a review of fluorescence probes for calcium imaging. This is followed by the description of the theoretical basis and the design features of three LSFM systems: a Selective Plane Illumination Microscope (SPIM), a Digital Scanned laser Light sheet based fluorescence Microscope (DSLIM) and a two-photon DSLIM.

The first system was employed in the study of Arabidopsis plant roots in the context of improving the growth of crops and their tolerance to stresses. Fingerprints of calcium signalling related to the application of specific stimuli were observed across the whole plant root, for extended periods of time, with single cell resolution and low photodamage. Spontaneous calcium oscillations in root hairs were correlated to their growth by tree-dimensional screenings and validated by the analysis of knockout mutants showing growth issues.

The DSLIM was used for neuroimaging in the study of spontaneous activity in the brain of zebrafish larva. Spontaneous activity could be recorded at high frame rate and for many hours, over different brain areas, with neuronal resolution. This provided insights on the activity patterns of neurons and on the possibility of predicting behavioural effects of the fish. Two-photon excitation was instead implemented to observe visually evoked responses and understand how visuomotor behaviours are processed.

Contents

Introduction	1
1 The Ion Calcium: from the Primordial Soup to Signals	5
1.1 Introduction	6
1.2 Calcium stores and sources	8
1.3 The signalling toolkit	9
1.4 General Ca ²⁺ encoding	12
1.5 Calcium channels in plants	13
1.6 Calcium channels in neurons	15
1.7 Seeing the calcium	16
1.7.1 Calcium probes	18
1.7.2 Strategy of calcium evaluation	19
1.7.3 Families of indicators	20
2 Light Sheet Fluorescence Microscopy	25
2.1 Fluorescence microscopy for calcium imaging	26
2.2 A novel approach to microscopy	29
2.2.1 Light sheet fluorescence microscopy	29
2.2.2 The long story of LSFM	33
2.2.3 Different illumination techniques	35
2.2.4 Light sheet detection	42

Contents

3	Calcium Dynamics in Plant Root	47
3.1	Introduction	48
3.1.1	From the improvement of crops to the imaging of roots	48
3.1.2	State of the art of calcium imaging in plant biology	49
3.1.3	Plant description	50
3.2	Material and methods	51
3.2.1	Plant preparation	51
3.2.2	Experimental setup	52
3.2.3	Seedling mounting	54
3.2.4	Plant root treatments	56
3.3	Results and discussion	56
3.3.1	Image quality	56
3.3.2	Ca ²⁺ dynamics observation through SPIM-FRET	59
3.3.3	Calcium oscillations in root hair of <i>Arabidopsis thaliana</i>	67
3.4	Conclusions	74
4	Calcium Imaging in the Brain of Zebrafish Larva	77
4.1	Introduction	78
4.1.1	Recording the brain activity	80
4.1.2	Zebrafish as a model organism	81
4.2	Experimental setup	83
4.2.1	Zebrafish preparation	83
4.2.2	The Digital Scanned laser Light sheet based fluorescence Microscope	84
4.2.3	Sample mounting	88
4.2.4	Imaging performances	89
4.2.5	Preprocessing and signal extraction	94
4.3	Experimental results	97
4.3.1	High speed recording of neuronal pattern in the optic tectum	97
4.3.2	Long-term recording for the study of neuronal patterns predictive of spontaneous behaviours	105
4.3.3	Two-photon excitation for visual stimulation analysis	108
4.4	Conclusions	114
	Bibliography	117

List of Figures

0	Statistics of the Method of the year 2014	2
1.1	The Ca ²⁺ signalling toolkit	10
1.2	Schematic evolution of an action potential	16
1.3	Ca ²⁺ pathways in neurons	17
1.4	FRET-based calcium indicators	20
1.5	Families of indicators	22
2.1	Standard microscopes	27
2.2	Light sheet fluorescence microscopy principle	30
2.3	Gaussian beam profile	31
2.4	Advantages of LSFM	33
2.5	The ultramicroscope	34
2.6	Different types of light sheet	36
2.7	Principle of DSLM	38
2.8	Further illumination techniques	41
2.9	Detectors	44
3.1	<i>Arabidopsis thaliana</i> plants	51
3.2	SPIM setup	53
3.3	Seedling mounting	55
3.4	Image quality of the SPIM-FRET setup for plant imaging	57
3.5	Three-dimensional reconstructions of <i>Arabidopsis</i> root	58

List of Figures

3.6	Single-plane FRET response to L-Glu of plants expressing the nuclear targeted cameleon	60
3.7	Single-plane FRET response to eATP of plants expressing the nuclear targeted cameleon	61
3.8	Statistical analysis of the response amplitude and duration . . .	62
3.9	Single-plane FRET response to L-Glu and eATP of plants expressing the cytosolic targeted cameleon	63
3.10	Four-dimensional imaging in seedlings expressing the nuclear targeted cameleon during eATP stimulus	65
3.11	Four-dimensional imaging in seedlings expressing the cytosolic targeted cameleon during eATP stimulus	66
3.12	Root hairs growing steps	68
3.13	Autocorrelation of Ca^{2+} oscillations	70
3.14	Correlation between growth rate and Ca^{2+} oscillations	70
3.15	Knock-out mutant shows a clear phenotype in the root hairs . .	71
3.16	Comparison of Ca^{2+} oscillations in root hairs wild-type and mutant seedlings	72
3.17	Fourier analysis of Ca^{2+} oscillations	73
3.18	Three-dimensional CICR	75
4.1	Animal models in neuroscience	79
4.2	Adult zebrafishes of different transgenic lines	82
4.3	Coarse brain anatomy of a 6 dpf zebrafish larva	82
4.4	Top view of the excitation path of the DSLM setup	85
4.5	Side view of the detection path of the DSLM setup	87
4.6	Zebrafish larva embedded in agarose	89
4.7	One and two-photon 2D images of zebrafish brain	91
4.8	3D imaging of zebrafish brain	92
4.9	Axial light sheet profile	93
4.10	Inference of fluorescence events	96
4.11	Retinotopic organization of the optic tectum	99
4.12	PCA- <i>promax</i> functional assemblies in the optic tectum	100
4.13	Raster plot and threshold from null model of spontaneous activity in the optic tectum	101
4.14	Single events maps	102
4.15	Wave-like patterns in the optic tectum	103
4.16	Repeated events of coactivation	103
4.17	Analysis of the lag of neuronal firing during activation events .	104

List of Figures

4.18 Increase in activity prior to spontaneous movement	106
4.19 Specificity for the directionality of routine turns	107
4.20 Raster plot of visually evoked activity	109
4.21 Orientation selectivity map	110
4.22 Orientation selectivity graphs	111
4.23 Polar plots of orientation selectivity	112
4.24 Clusterization of the activity with K-means algorithm	113

Introduction

EVERY TIME WE LOOK AT LIFE ON EARTH, we remain fascinated by how incredibly perfect, yet complex, it is. From our childhood to oldness, we all remain amazed by the majesty of life. Even simple actions, like taking a picture of a flower, imply a series of complicated events, taking place both in the macroscopic and microscopic scale, happening in extremely short time but that can have long term effect and are moulded by experience. We need to see images of the flower with our eye, while the eye muscles keep the field of view centred on the flower, with the retinas sending images of the flower to the brain; this latter, at the same time decides when to take a picture, communicating with the muscle of our arm and our finger to press the shutter button. Then, we press in a fast, controlled way, converting energy to mechanical motion. And the image remains impressed also in our memory.

From the primordial soup, an ubiquitous element involved in all these processes is the calcium ion. It is so effective that it became necessary, early in the evolution of life, to create mechanisms to reduce calcium ions concentration from the cell cytosol. The existence of large concentration gradients across cell membranes created the perfect conditions to enable calcium signalling, spatiotemporal calcium patterns that encode a variety of process taking place in an organism.

These patterns can be explored thanks to increasingly refined techniques, which ideally should allow the measure of calcium concentration in a single cell surrounded by a large number of other cells, in order to understand its func-

Introduction

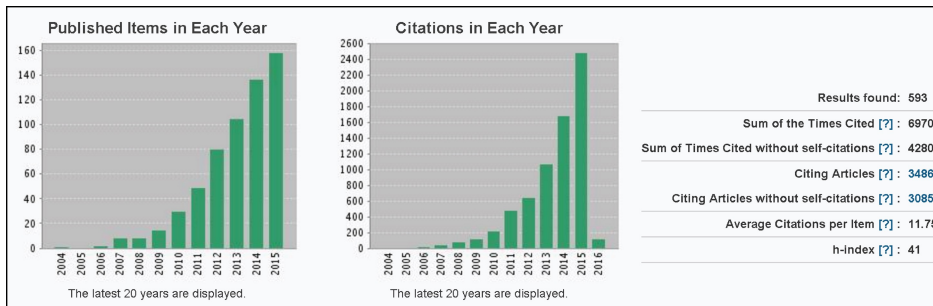


Figure 0: *Light sheet microscopy statistics from Web of Knowledge. The number of the published and especially cited papers about light sheet fluorescence microscopy has increased exponentially in the last decade.*

tional role. Among these techniques, fluorescence microscopy has always had a prominent role. Lots of progresses have been made in calcium imaging techniques in the last decades, leading even to the formulation of new questions about decoding and improving life conditions on earth.

This thesis describes a novel approach to study calcium dynamics in living samples, called light sheet fluorescence microscopy. This technique puts the sample at the very centre of the microscope, approaching it with a multiscale scheme, under different points of view. It allows one to observe a wide field of view with single cell resolution and sectioning capability, with the possibility to record at high speed, for long time an organism in non-damaging conditions. This method comes from a century-old idea, though the first biologically relevant application only arrived in 1993 and the scientific community discovered it in 2004. But, after that, the number of publications (more than 500) and of citations (11.7 per paper on average) increased exponentially, till it was named the *Method of the year 2014* by Nature (Figure 0).

This tomographic device, running in the visible or near-infrared ranges, offers the possibility to investigate a variety of living biological samples, mainly small (in the order of one millimetre) translucent specimens. The two research topics that I faced during my PhD, deal with plant roots of *Arabidopsis thaliana* and zebrafish (*Denio rerio*) brain.

In Chapter 1, the main motivations about the importance of the ion calcium are highlighted, and a review of the main calcium channels is presented, with emphasis to plant roots and neurons. This is followed by a report on calcium indicators, the tools that allow one to actually see calcium dynamics.

Chapter 2 explains the principle of light sheet fluorescence imaging with com-

parison to standard techniques. Three main implementations of light sheet microscopy are discussed to lay the theoretical bases of the systems that I have implemented: static light sheet, digitally scanned light sheet and two-photon digitally scanned light sheet.

The third and fourth chapters discuss the two main subjects that I had dealt with. Chapter 3 concerns the improvement of crop yield and their tolerance to diverse stresses. Arabidopsis roots have been used as a model specimen and have been studied by static light sheet microscopy. The variety of benefits of using such a technique for the characterization of the response to the application of different stimuli are highlighted. Calcium signalling in the root cells across the whole plant organ has been observed, revealing specific fingerprints related to the application of different stimuli. The possibility to observe also spontaneous activations in single cells, allowed us to correlate root hair growth and spontaneous calcium oscillations in the root hair apex by tree-dimensional screenings. The deregulation of these calcium variations observed in knockout mutants was indeed linked to altered plant health.

Chapter 4 deals with a field born two decades ago and strongly emerged since then: neuroimaging. The brain is an intricate network, whose understanding cannot disregard its interaction with the external world, as well as its spontaneous intrinsic dynamic. Decoding the brain would open incredible new opportunities both in medical research and artificial intelligence studies. A key model for optical neuroimaging is the zebrafish larva, a small transparent behaving vertebrate. Neuronal activity from different brain regions of larvae was acquired with neuronal resolution and minimal photodamage by digital scanned laser light sheet based fluorescence microscopy. Spontaneous activity was recorded with one-photon illumination at high frame rate and in the long term, providing insights on the structure of large neuronal circuits and on the possibility of predicting behavioural outcomes. Two-photon excitation was instead implemented to observe visually evoked responses and to understand how orientation selectivity is encoded to process visuomotor behaviours.

All the experiments were run with specially designed light sheet microscopes, giving results that could have been hardly obtained with standard techniques. The achieved results shed new light on both the fields of investigation, opening new perspectives for further studies.

These projects are the outcome of a synergy with the Dipartimento di Bioscienze of Università degli Studi in Milano for the plant biology project and with the Institut de Biologie of the École Normale Supérieure in Paris for the neuroimaging part.

CHAPTER *1*

**The Ion Calcium: from the Primordial Soup to
Signals**

IN THE LAST DECADES, there has been a great emphasis in life science on the study of calcium dynamics. This ubiquitous ion is involved in all the basic processes that can take place in an organism from cells to organs. The changes in its cellular concentration occur with refined spatial and/or temporal patterns, essential for most functional processes.

The following chapter gives an overview of the main calcium pathways to understand this signalling toolkit, with specific reference to plant roots and neurons. Since the interest is on calcium imaging, a review of the principal calcium indicators is given.

Chapter 1. The Ion Calcium: from the Primordial Soup to Signals

1.1 Introduction

Life science investigates the diversity, complexity, and interconnectedness of life on earth. The study of a cell, tissue, organ or entire organism requires a multiscale approach from microscopy to macroscopic observation of the sample under test. Understanding the interaction among cells as well as the one with the external environment requires the capability to comprehend how cells process information. The gathering and processing of this information takes place through the modulation of membrane potentials. These are electric potential differences between the sides of cellular membranes, created by the different concentration of ions between the inside environment and the outside one. The migrations of ions are regulated by the opening of pore-forming proteins, or channels, positioned not only on the plasma membrane, but also in the ones of internal compartments, which selectively change their conformation according to the electrochemical gradient. At the same time, the opening of a channel influences the membrane potential by locally varying the ion concentration. This complex interaction between channels opening and membrane potential variation creates an intricate feedback pattern, which can lead to different physiological outcomes, like adaption, growth, or even apoptosis of the cells.

Knowledge of the intracellular concentration of ions is thus fundamental. Monovalent ions (Na^+ , K^+ , H^+ , and Cl^-) generally provide for electrical excitability and energy production, while divalent cations (Ca^{2+} , Mg^{2+} , Zn^{2+}) are crucial for cellular biochemistry and regulation. In this whole mechanism of cellular signal processing, the calcium Ca^{2+} ion plays a central and fundamental role. The unique biophysical properties of Ca^{2+} has been known from more than a century, and, since their discovery, millions of experiments aided in building up the fame of intracellular Ca^{2+} as a “universal signalling molecule” [95]. For this reason, in the last decades the study of the dynamics of intracellular calcium concentration [Ca^{2+}] has been a major focus in life science, and the knowledge of calcium signalling and of its corresponding physiological outcome has grown significantly. As a matter of fact, Ca^{2+} ions are used as transducing molecules, or second messengers, by almost all cell types, from prokaryotic to eukaryotic ones. Many endogenous stimuli and stress signals of both biotic and abiotic nature lead to transient variations in the intracellular calcium concentration [Ca^{2+}], which in turn activate specific downstream signalling cascades, triggering or mediating a wide variety of cellular processes. From an evolutionary point of view, why the Ca^{2+} has been chosen to be so

unique among all the possible ions is still not completely understood, but its universality and effectiveness has an important evolutionary implication. As a matter of fact, specificities of ATP-based energetics of primordial cells required tight control over $[Ca^{2+}]$. An excess of Ca^{2+} inside the cell would have been toxic: high $[Ca^{2+}]$ would induce aggregation of proteins and nucleic acids affecting the integrity of lipid membranes, and would initiate precipitation of phosphates [15]. As a result, cells developed a highly sophisticated system to maintain the equilibrium. First of all, the activatory actions of Ca^{2+} ions are usually accomplished not directly by the ions alone, but through their binding to a number of high-affinity binding proteins (CaBPs), like calmodulin (CaM), troponin C, etc. These proteins are negatively charged at physiological pH and can be highly Ca^{2+} -selective. Moreover, Ca^{2+} is favoured as a regulatory molecule thanks to its double positive charge, which results in a higher affinity when binding to negatively charged proteins than monovalent cations such as Na^+ or K^+ . At the same time, Ca^{2+} has a lower affinity compared to larger divalent cations such as Cu^{2+} , Zn^{2+} or Mn^{2+} , but also a lower dissociation constant. Finally, Ca^{2+} has a higher and more flexible coordination chemistry than that of Mg^{2+} for example. Concentration of free Ca^{2+} ions in the cytosol of all cells is maintained at approximately 50 to 150 nM, around 20000 times lower than that in the extracellular space, even lower when compared to that of intracellular domains or organelles. Considering that for a good signalling system the intrinsic signal-to-noise ratio is essential, it is possible to understand the importance of Ca^{2+} in this context. The existence of a large concentration gradient across membranes created the ideal condition for calcium to be the signalling molecule *par excellence*. Indeed, because of this large electrochemical Ca^{2+} gradient always directed towards the cytosol, even very short-lived changes in the Ca^{2+} permeability of the membranes will rapidly generate considerable signals. Obviously, to allow cells to be always prompt for the activation, an effective mechanism of cytosolic Ca^{2+} removal has been developed during the evolution process, permitting the return of $[Ca^{2+}]$ to the low basal level for the system to be primed again. The combination of Ca^{2+} movements between intracellular compartments and the cell and extracellular environment produce spatiotemporally organized fluctuations that are generally referred to as “ Ca^{2+} signals”.

Chapter 1. The Ion Calcium: from the Primordial Soup to Signals

1.2 Calcium stores and sources

The stores of Ca^{2+} during these ion movements include not only the extracellular environment, but also some intracellular compartments such as the mitochondria, the nucleus, the endoplasmic reticulum (ER) and sarcoplasmic reticulum (SR). Mitochondria can actually both accumulate excess of Ca^{2+} during periods of intense cellular activity and release it after stimulation, sustaining calcium signals. While the nucleus and the mitochondria are just stores of Ca^{2+} , the ER and SR can be seen as the main intracellular source for initiating Ca^{2+} signalling, and in fact the majority of the eukaryotic cells prefers using these intracellular Ca^{2+} stores as their primary source for Ca^{2+} signal generation.

Cells that exclusively use these stores are generally known as non-excitabile cells and, since their membrane depolarization is not followed by a subsequent regenerative depolarization, they cannot generate or propagate electrical signals. In this case, the general mechanisms for Ca^{2+} signal generation involves activation of plasma membrane (PM) receptors and the synthesis of an intermediate signalling molecule, which then acts on specific Ca^{2+} release channels situated on the ER membranes. This first signal can then be followed by a secondary release of intracellular Ca^{2+} mediated by other channels sensitive to the cytosolic $[\text{Ca}^{2+}]$, which acts like a signal amplifier.

On the other hand, also the extracellular Ca^{2+} alone can initiate signalling. For example neurons, considered as the ultimate excitable cells, primarily exploit extracellular Ca^{2+} for their signal generation, though the possibility of contribution of intracellular Ca^{2+} stores is still being debated. In functional terms, it makes sense that neurons, which require a rapid speed of processing, have developed a system of using preferentially the extracellular Ca^{2+} : in this way, the activation and full Ca^{2+} response is completed within milliseconds, while intracellular Ca^{2+} can still participate in regulation and excessive Ca^{2+} buffering.

Nonetheless, in some cells the shaping of the Ca^{2+} signal involves extracellular and intracellular Ca^{2+} at the same time, for example by means of store-operated Ca^{2+} channels or SOCC, (as discussed below) in the PM, sensitive to the exhaustion of the finite amount of Ca^{2+} in the ER. Anyway, every type of cell has its specific mechanism of interplay between intracellular and extracellular Ca^{2+} sources.

1.3 The signalling toolkit

By analysing the temporal behaviour of these processes, we can distinguish between immediate and delayed responses activated by Ca^{2+} signals. The immediate response is the one taking place in the milliseconds-to-seconds range, with a short delay between signalling and execution and, as a consequence, in short spatial ranges and primed pathways. It is the case for example of muscle contraction, exocytosis and neurotransmitters. The delayed responses are more varied and less defined, since the lag time between the signalling and the final response could vary from seconds to even months. This response could include regulation of intracellular enzymes, gene expression, cellular development, growth and death. Since in the same cell multiple different responses can take place at the same time to provide a functional continuum, every Ca^{2+} signal triggering specific responses must be finely encoded, to be in the end decoded by the system. In this sense, the versatility of Ca^{2+} arises from the use of an extensive molecular repertoire of signalling components, which creates a “toolkit” of signals whose simultaneous interplay produces a large variety of different spatial and temporal output profiles. This toolkit basically relies on “ON” mechanisms of increase of the $[\text{Ca}^{2+}]$ in the cytoplasm and “OFF” mechanisms that remove Ca^{2+} to restore the basal state. A graphical representation of the toolkit is given in Figure 1.1.

The “ON” mechanisms

The “ON” mechanisms depend on Ca^{2+} channels that are built up by a heterogeneous family of proteins, providing Ca^{2+} entry from the extracellular environment and/or release of ions from intracellular organelles. In the PM it can be found the best known typology of channels, the voltage-operated calcium channels (VOCCs), which are activated by the depolarization of the membrane. The VOCCs are highly Ca^{2+} permeable and consist of a set of protein subunits, where usually one acts as the real channel while the others regulate the gating, but a wide variety of isoforms of these protein and, of course, of combinations, have been detected. The binding of a specific agonist (e.g. ATP, glutamate, serotonin etc.) to the extracellular domain instead activates ligand-gated or receptor-operated Ca^{2+} channels (ROCCs). These have a lower permeability for Ca^{2+} and include an assortment of structurally and functionally various channels. Many cell types show mechanically activated Ca^{2+} channels, which respond to stress/shape changes that the cell is undergoing. Finally, on the PM we can find the already mentioned store-operated Ca^{2+} channels (SOCCs), ac-

Chapter 1. The Ion Calcium: from the Primordial Soup to Signals

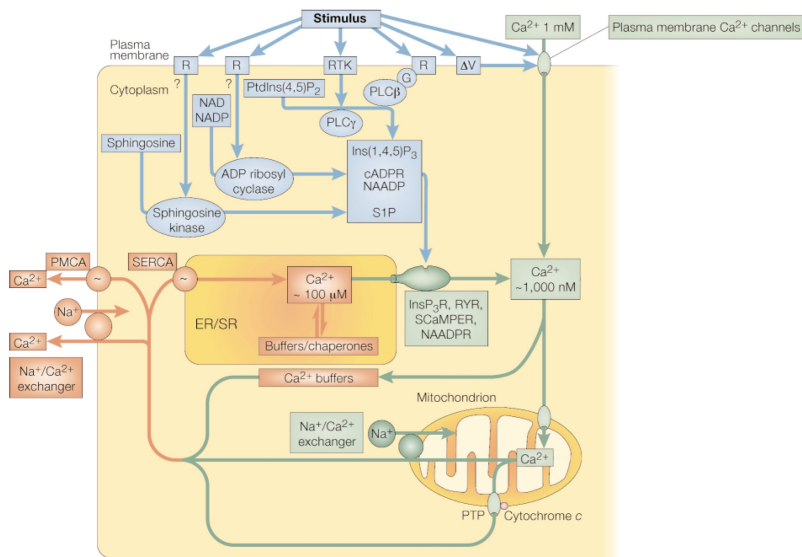


Figure 1.1: Elements of the Ca^{2+} signalling toolkit. Ca^{2+} -mobilizing signals (blue) are generated by stimuli acting through a variety of cell-surface receptors (R), including G-protein (G)-linked receptors and receptor tyrosine kinases (RTK). The signals generated include: inositol-1,4,5-trisphosphate ($\text{Ins}(1,4,5)\text{P}_3$), generated by the hydrolysis of phosphatidylinositol-4,5-bisphosphate ($\text{PtdIns}(4,5)\text{P}_2$) by a family of phospholipase C enzymes ($\text{PLC}\beta$, $\text{PLC}\gamma$); cyclic ADP ribose (cADPR) and nicotinic acid dinucleotide phosphate (NAADP), both generated from nicotinamide-adenine dinucleotide (NAD) and its phosphorylated derivative NADP by ADP ribosyl cyclase; and sphingosine 1-phosphate (S1P), generated from sphingosine by a sphingosine kinase. ON mechanisms (green) include plasma membrane Ca^{2+} channels, responsive to transmitters or to membrane depolarization, and intracellular Ca^{2+} channels like the $\text{Ins}(1,4,5)\text{P}_3$ receptor (InsP_3R), ryanodine receptor (RYR), NAADP receptor and sphingolipid Ca^{2+} release-mediating protein of the ER (SCaMPEP). The Ca^{2+} released into the cytoplasm activates different Ca^{2+} sensors and processes, depending on cell type and context. OFF mechanisms (red) pump Ca^{2+} out of the cytoplasm: the $\text{Na}^+/\text{Ca}^{2+}$ exchanger and the plasma membrane Ca^{2+} ATPase (PMCA) pumps Ca^{2+} out of the cell and the sarco-endoplasmic reticulum Ca^{2+} ATPase (SERCA) pumps it back into the ER/SR. (CAM, calmodulin; PTP, permeability transition pore). Adapted from Berridge and coworkers [9].

tivated in response to depletion of the intracellular Ca^{2+} store, whose effect is to sustain and shape the signal. How the exhaustion of the organelles is perceived is still unknown.

Other sets of Ca^{2+} channels are expressed in intracellular stores membrane. Their Ca^{2+} release is mediated by several types of intermediate messengers: the binding of many hormones or growth factors to specific receptors on the PM leads to the production of the intracellular messengers inositol 1,4,5-trisphosphate (InsP3) and diacylglycerol. InsP3 moves in the cytoplasm where it encounters specific receptors (InsP3Rs) on the ER/SR, which change their conformation, opening and releasing Ca^{2+} . The InsP3Rs activation is however modulated by the $[\text{Ca}^{2+}]$ itself: an increase in $[\text{Ca}^{2+}]$ within a specific threshold enhances the channel opening, whereas a higher $[\text{Ca}^{2+}]$ inhibits it. A structurally and functionally analogues family of ER/SR receptors are the Ryanodine (RyRs) or Ca^{2+} -gated Ca^{2+} channels. Also these channels are sensitive to cytosolic Ca^{2+} concentrations, although in their case the Ca^{2+} concentration must be higher, and they are actually the main responsible of the phenomenon known as Ca^{2+} -induced Ca^{2+} release (CICR). The capability of RyRs to sense Ca^{2+} variations is mediated by cyclic ADP ribose (cADPR), while a related messenger, nicotinic acid dinucleotide phosphate (NAADP), acts on a separate channel still under study. The RyRs can also act like signal amplifiers, since their activation can follow the Ca^{2+} release from InsP3Rs. Finally, also mitochondria can participate in CICR, though they have to accumulate Ca^{2+} before it. A further channel is the sphingolipid Ca^{2+} -release mediating protein of endoplasmic reticulum (SCaMPER), whose physiologic function is under strong research.

The “OFF” mechanisms

The second step in the signalling toolkit is the removal of the Ca^{2+} from the cytoplasm by various pumps and exchangers, the “OFF” mechanism. Firstly, in the cytosol we can find various Ca^{2+} binding proteins, some fixed and some mobile, buffering the Ca^{2+} and participating in the spatial coding mechanism. The recovery of the basal state is mainly mediated by high-affinity ATP-dependent Ca^{2+} pumps present in membranes: the plasma membrane Ca^{2+} -ATPase (PMCA) pumps and $\text{Na}^+/\text{Ca}^{2+}$ exchangers return Ca^{2+} to the extracellular environment, while the sarco-endoplasmic reticulum ATPase (SERCA) pumps segregate Ca^{2+} in the internal stores. Once the cytosolic Ca^{2+} has returned to its resting level, a mitochondrial $\text{Na}^+/\text{Ca}^{2+}$ exchanger can pump the

Chapter 1. The Ion Calcium: from the Primordial Soup to Signals

large load of Ca^{2+} back into the cytoplasm, from which it is either returned to the ER or removed from the cell. Lastly, a permeability transition pore (PTP) can form on mitochondria, activated by the build-up of Ca^{2+} within the mitochondrial matrix and hence participating in CICR. Two functional states of PTP are known: a reversible low conductance state, allowing mitochondria to become excitable, and an irreversible high conductance state, which can make the mitochondrion collapse and lead to apoptosis.

1.4 General Ca^{2+} encoding

On a coarse level, further versatility of the signalling toolkit is achieved through both a spatial and temporal encoding. The spatial properties are due to an amplitude modulation of the Ca^{2+} signals, each prompting a different specific effect, determined by the affinity with the intracellular Ca^{2+} sensors. Moreover, variations in the Ca^{2+} signal are determined not only by the changes in the total amount of cytosolic Ca^{2+} , but also by the type and distribution of the various Ca^{2+} buffers and sensors, which are not homogenous in the cells and indeed create local Ca^{2+} domains or “ Ca^{2+} gradients”. This heterogeneity accounts for the directionality in the intracellular propagation of the Ca^{2+} signal, which follows specific pathways producing a sort of vectorial code. The propagation of the signalling appears as a cytosolic “ Ca^{2+} wave”, with specific spatial and temporal properties. For waves to occur, most of the InsP3Rs and the RyRs respond to each other through the process of CICR: Ca^{2+} emitted from one receptor diffuses to the neighbouring one exciting further release, therefore setting up a regenerative process. For example, since InsP3Rs and/or RyRs have different degrees of excitability depending on the levels of the appropriate Ca^{2+} -mobilizing messenger, their opening depends on how small, but higher than a threshold, the level of calcium is. These single-channel events of InsP3Rs and RyRs have been known as quarks or blips, respectively, and may be considered the building blocks of more complex Ca^{2+} signals. At higher $[\text{Ca}^{2+}]$, coordinated opening of clusters of InsP3Rs or RyRs, known as puffs or sparks, respectively, can be reached, and the amplitude of the signal can be linked to the number of opened channel involved. Also, increasing sparks frequency can result in a cascade and become regenerative, setting up two- or three-dimensional waves of changes in $[\text{Ca}^{2+}]$ that propagate within cells. From a temporal point of view, this repeated activation of the Ca^{2+} -mobilizing receptors can evoke oscillatory patterns of $[\text{Ca}^{2+}]$. This temporal coding can be analyzed at three main levels: i) the shape of these oscillations; ii) the de-

1.5. Calcium channels in plants

pendency of the frequency of Ca^{2+} oscillations on stimuli; iii) the specificity of the cytosolic oscillation of an individual cell compared to that of a population. Variations of the basic pattern from cell to cell is a phenomenon called “ Ca^{2+} fingerprint”.

When looking at a whole tissue or organism, it becomes of more interest the mechanism of intercellular communication. In fact, intracellular waves can spread to neighbouring cells, coordinating the activity of many cells. How the waves traverse the gap junction is a matter of considerable debate.

Cell-to-cell signalling can occur thanks to the presence of gap junction channels, which circumvent cellular Ca^{2+} autonomy. For some cells types, the messenger seems instead to be InsP_3 or even ATP. Intercellular signals can also be prompted by VOCCs, which rapidly rise periplasmic $[\text{Ca}^{2+}]$ triggering protein fusion and enabling vesicles containing transmitter molecules to fuse to the plasma membrane. Whatever the mechanism, the molecules released in the external environment can gate channels and receptors on adjacent cell membranes. These Ca^{2+} -mediated events are of great interest in neuroscience, where VOCCs create a local pulse of Ca^{2+} to trigger vesicle release in the process of exocytosis at synaptic endings, but corollaries have been formulated in intercellular communication in almost all cell types.

1.5 Calcium channels in plants

In resting plant cells, the cytosolic $[\text{Ca}^{2+}]$ is maintained around 100 nM by the activity of Ca^{2+} -ATPases and $\text{Ca}^{2+}/\text{H}^+$ antiporters in cell membrane. Ca^{2+} channels have been characterized in the PM, the SR, the vacuole, nuclear and plastid membranes. In the PM, the channels can be divided into depolarisation-activated, hyperpolarization-activated and voltage-insensitive channels. Depolarisation-activated Ca^{2+} -permeable channels (DACC) have been found in the PM of all plant root, leaf mesophyll and suspension-cultured cells, in which a characteristic Ca^{2+} current has been identified. This current is activated by membrane depolarisation to voltages more positive than about -140 mV, whereas at extreme negative voltages it shows a slow and reversible inactivation. In general, these channels are thought to regulate stress-related signals like environmental, developmental and pathological stimuli, generating a global signal. As an example, the distribution and activation of proteins in the PM can be coordinated by the cytoskeleton, which can regulate the direction of growth of root hairs.

Hyperpolarisation-activated Ca^{2+} channels have been characterized in proto-

Chapter 1. The Ion Calcium: from the Primordial Soup to Signals

plasts from various cell types. In the PM of onion epidermal cells they act as mechanoreceptors activated by stretch. In guard cells they appear to trigger PM depolarization, coordinating the loss of solutes and initiating stomatal closure. In root endodermal cells they are supposed to take part in the mineral nutrition process. Mechanosensitive ion channels may serve a role in the regulation of turgor as a response to gravity, touch or flexure stimulation.

An interesting case is the elongation of root hairs [100] and pollen tubes, studied by analogy with the tip-growth of algal rhizoids and fungal hyphae. The proposed mechanism of growth for polarized cell is that the PM stretches as a consequence of cell wall yielding and local turgor-driven evagination; this opens locally stretch-activated Ca^{2+} channels, which makes the extracellular Ca^{2+} enters into the cytosol generating a Ca^{2+} gradient in the tip. Finally, movements of secretory-vesicles and exocytosis reduces the elevated $[\text{Ca}^{2+}]$. However, the actual Ca^{2+} channels involved in these processes have not yet been elucidated. In *Arabidopsis thaliana* root, depolarization-activated Ca^{2+} -current was observed in all cell types, while hyperpolarization was observed in a subgroup of cells in the elongation zone, including endodermal cells. It has indeed been suggested that the ubiquitous depolarization-activated channels are involved in cell signalling, while the hyperpolarization one may have a role in mineral nutrition.

Two elicitor-activated, plasma-membrane Ca^{2+} -permeable channels have been documented, triggering the Ca^{2+} influx as an early event in the initiation of defence responses to pathogens. The first type activates at voltages more negative than -120 mV, while the activity of the second, termed large-conductance elicitor-activated channel (LEAC), does not appear to depend on the membrane potential (between -30 and -150 mV).

The vacuole may occupy more than 90% of the volume of a plant cell and constitutes a major source of Ca^{2+} . Both the resting membrane potential (-20 mV to -50 mV) and the difference between cytosolic (100 to 500 nM) and vacuolar $[\text{Ca}^{2+}]$ (micromolar to millimolar) favour the entering of Ca^{2+} in the cytoplasm. This Ca^{2+} efflux from the vacuole could sustain large and prolonged elevations in the cytosolic $[\text{Ca}^{2+}]$ by propagating and amplifying an initial signal. When the initiation comes from a cytosolic $[\text{Ca}^{2+}]$ rise, a CICR appears, but the role of the different channels in this event is still of great debate. Also in the case of vacuole membrane, there are several classes of channels like depolarization activated Ca^{2+} channels, comprehending the slow vacuolar channels with still an unclear physiological role, and the hyperpolarization activated Ca^{2+} channels, which catalyse Ca^{2+} influx to the cytoplasm. These channels

1.6. Calcium channels in neurons

may serve a role in cell signalling. Several classes of second-messenger activated Ca^{2+} channels have also been found, like those activated by the InsP3 and the cADPR, highly selective for divalent cations.

Calcium channels have also been characterized in the SR and the calcium efflux from them has been shown to be implicated in cell signalling. For example, it has been shown that in *Brassica oleracea* Ca^{2+} can be released by the application of cADPR, NAADP and possibly InsP3, suggesting the presence of Ca^{2+} channels dependent on these molecules.

Finally, a channel permeable to Ca^{2+} , Mg^{2+} and K^+ has been found in swollen thylakoids from spinach chloroplasts and one permeable to K^+ , Na^+ , Cs^+ and Ca^{2+} in the nuclear envelope of nuclei from red beet. For a wide variety of Ca^{2+} channels, an electrical characterization have been done. However, the physiological role as well as the stimuli activating many of them is still under study.

1.6 Calcium channels in neurons

Neurons are the excitable cell *par excellence*. They present numerous Ca^{2+} channels with different localizations and different functions. As in all cells, the different concentration of ions in the intracellular and extracellular environment, creates an electric potential difference between the sides of the cellular membrane, leading, for most neurons, at a resting state of about -70 mV. All neuron types are able to generate a stereotyped event, called an “action potential” (Figure 1.2).

An action potential occurs in the cell when the membrane potential increases up to a threshold, generally around -55 mV, at which VOCCs for Na^+ open. Since the concentration of sodium is much higher outside the cell than inside it, this causes a rapid increase in the membrane potential, up to positive values, where VOCCs for K^+ open and Na^+ channels close. The concentration of K^+ is higher inside the cell, so that the opening of the channels abruptly lowers the membrane potential towards negative values. The action potential propagates along the axon at high speeds (up to 100 m/s) through the serial opening of VOCCs for Na^+ equally spaced along the axon. At its termination the axon ramifies, and contacts other neurons by synapses. Here local VOCCs open, with the influx of Ca^{2+} triggering exocytosis of a neurotransmitter in the synaptic space, passing information between neurons. ROCCs on the adjacent neuron can open and receive the neurotransmitter, altering the membrane potential. The described event results in a fast spike in membrane potential, which

Chapter 1. The Ion Calcium: from the Primordial Soup to Signals

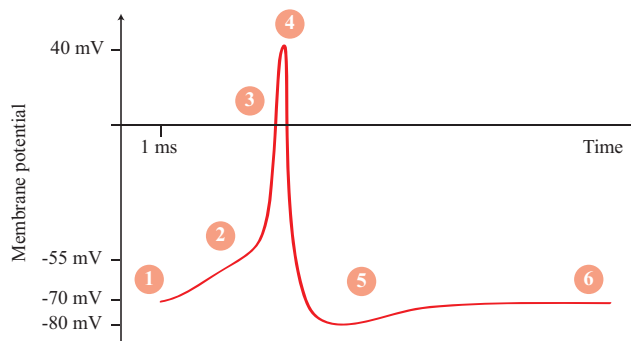


Figure 1.2: *Schematic evolution of an action potential. 1. Resting state. 2. Sodium channels opening threshold. 3. Potassium channels open. 4. Sodium channels close. 5. Refractory period. 6. Resting state.*

lasts, in most vertebrate organisms, humans included, around one millisecond. Neurons also have internal Ca^{2+} stores. The store function is usually attributed to the ER, where the InsP3Rs and of RyRs have been found. Internal Ca^{2+} release have been documented in various types of neurons at different developmental stages. While InsP3-mediated calcium release is mostly triggered by some neurotransmitters, RyRs can be activated by elevations of the cytosolic $[\text{Ca}^{2+}]$, which by CICR amplifies the neuron activation or firing. Both InsP3Rs and RyRs are regulated by calcium itself along with other intracellular factors. In the case of InsP3Rs, calcium influx plays an essential role in generating Ca^{2+} waves in neocortical and other types of neurons. In hippocampal neurons, for example, electrical activity resulting in Ca^{2+} entry through VOCCs acts together with InsP3 produced by metabotropic glutamate receptors (mGluR1) to produce a synergistic release of internal Ca^{2+} (see Figure 1.3).

Communication between neurons is actually an intricate subject not only from the point of view of the channels that can be found expressed on them, but also for the wire of communication they can establish. The study of how and why these connections form, is becoming more and more of interest and is making neuroscience an incredibly wide interdisciplinary field.

1.7 Seeing the calcium

The understanding of the biological complexity of calcium signalling has been dependent on the methodologies of measuring the calcium concentration $[\text{Ca}^{2+}]$ in living cells. Nowadays the ideal technique for Ca^{2+} evaluation should allow

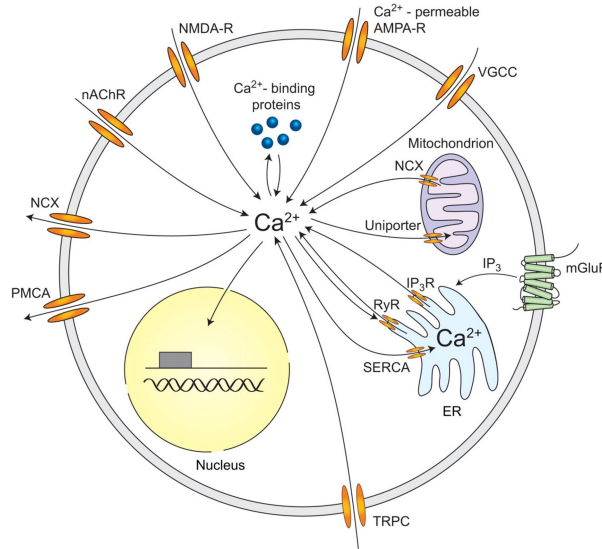


Figure 1.3: Ca^{2+} pathways in neurons. Sources of Ca^{2+} influx are calcium-permeable α -amino-3-hydroxy-5-methyl-4-isoxazolepropionic acid (AMPA) and *N*-methyl-*D*-aspartate (NMDA) glutamate-type receptors, voltage-gated calcium channels (VGCC), nicotinic acetylcholine receptors (nAChR), and transient receptor potential type C (TRPC) channels. Calcium release from internal stores is mediated by inositol trisphosphate receptors (InsP3Rs) and ryanodine receptors (RyRs). InsP3 can be generated by metabotropic glutamate receptors (mGluR). Calcium efflux is mediated by the plasma membrane calcium ATPase (PMCA), the sodium-calcium exchanger (NCX), and the sarco-endoplasmic reticulum calcium ATPase (SERCA). Also the mitochondria are important for neuronal calcium homeostasis. Reproduced from Grienberger and coworkers, [32].

one to measure $[Ca^{2+}]$ in a single cell (microscopic level), as well as in a large number of cells surrounding it, to understand the effect of calcium signalling (macroscopic level). The two main techniques to study the functional output of Ca^{2+} signals over a population of cells are electrophysiology and fluorescence imaging. The first one involves the use of microelectrodes inside the cells to provide direct measurements of the voltage changes in the channels. The disadvantage however is its complexity and invasiveness, as well as its intrinsic incapability to record signals from many cells. Although single-cell patch-clamp techniques can nowadays be parallelized to enable recordings from even 200 cells using multi-electrode arrays [13], a powerful alternative for record-

Chapter 1. The Ion Calcium: from the Primordial Soup to Signals

ing the activity of hundreds of cells at the same time is calcium imaging. This strategy is based on fluorescence microscopy and has a lower temporal resolution compared to electrophysiology, but balances this with the advantage of being non-invasive and providing precise spatial localization of each of the cells being monitored. In the last decades, the advances of optical methods and sensors increased tremendously the attention on fluorescent Ca^{2+} probes and microscopy development.

1.7.1 Calcium probes

Ca^{2+} probes (also known as indicators, reporters or sensors) are molecules that can selectively and reversibly bind with Ca^{2+} ions. These indicators estimate the amount of free and bound ions. The concentration of free Ca^{2+} is indirectly calculated taking into account the effective dissociation constant (K_d) of the probe for Ca^{2+} in the environment where it is located. Inevitably, since all indicators act as Ca^{2+} buffers, their use leads to an increase in the Ca^{2+} buffering capacity.

The first measurements of this type were done with organic fluorescent dyes like murexide, azo dyes and chlortetracycline, whose spectral properties changes when binding to Ca^{2+} , but had several limitations. For example, azo dyes have complex and variable Ca^{2+} -dye stoichiometries, small signal-to-noise ratio and had to be introduced into cells by technically tough methods (microinjection or intracellular perfusion). Chlortetracycline shows instead large increases in fluorescence on Ca^{2+} binding but is mainly sensitive to $[\text{Ca}^{2+}]$ changes only in membrane as well as to several other parameters ($[\text{Mg}^{2+}]$, membrane potential, pH). In 1980 Roger Tsien presented the first fluorescent probe for intracellular use specifically designed for Ca^{2+} imaging, called BAPTA [94]. These fluorescent polycarboxylate dyes are based on modifications of the best known selective Ca^{2+} -chelator available, ethylene glycol tetraacetic acid (EGTA), properly revised to change its excitation and/or emission characteristics when binding to Ca^{2+} . By the way, BAPTA itself is not satisfactory as an indicator since its absorption spectrum is peaked in far ultraviolet range, but its improved derivatives became soon popular probes. This led to the synthesis of their acetoxymethyl esters [93], which allowed the trapping of these indicators in living cells in a technically simple way in fundamentally all cell types with minimal side effects.

The field experienced an even bigger burst with the investigation of the phenomenon of bioluminescence in the medusa *Aequora Victoria*, which brought

to the identification of aequorin (AEQ) [87] and green fluorescent protein (GFP) [59] by Shimomura, Nobel Prize in Chemistry in 2008, as well as altered version of these to produce variants with different excitation and emission spectra. The big improvement introduced by these proteins is that they can be selectively targeted to most subcellular compartments by genetically encoding them (GECIs, Genetically Encoded Calcium Indicators). While AEQ has a small fluorescence, affecting space and time imaging resolution, encoded GFPs maintains their strong signal, which explains their great diffusion. Indeed, starting from the 1997, three main families of Ca^{2+} sensors were developed based on GFPs: the camelons [56], the camgaroos [6] and the pericams [62]. These probes are all linked to a Ca^{2+} -binding protein, calmodulin, which undergoes a conformation change in presence of Ca^{2+} . This variation in the molecular structure of the sensor alters the fluorescence characteristics of the GFP, and the quantification of this variation gives an indirect estimation of the Ca^{2+} concentration around the indicator.

1.7.2 Strategy of calcium evaluation

We can distinguish two main classes of Ca^{2+} sensors, the non-ratiometric and the ratiometric one. Non-ratiometric probes can be excited with a single wavelength and the $[\text{Ca}^{2+}]$ is determined by looking at relative variations in the fluorescence intensity as follows

$$[\text{Ca}^{2+}] = K_d \times \frac{F - F_{min}}{F_{max} - F} \quad (1.1)$$

where K_d is the dissociation constant; F is the fluorescence intensity; F_{max} is F at saturating $[\text{Ca}^{2+}]$; F_{min} is F at zero $[\text{Ca}^{2+}]$.

Ratiometric dyes experience instead a substantial change in the excitation (emission) spectrum when the $[\text{Ca}^{2+}]$ varies, for example a spectral shift. The $[\text{Ca}^{2+}]$ is therefore evaluated as the ratio between two different fluorescence intensity values, taken at two different wavelengths of the altered excitation (emission) spectrum. In this case, $[\text{Ca}^{2+}]$ is calculated as

$$[\text{Ca}^{2+}] = K_d \times \frac{R - R_{min}}{R_{max} - R} \times \frac{S_{b2}}{S_{f2}} \quad (1.2)$$

where R is the ratio between the fluorescence of the acceptor and that of the donor; R_{max} is R at saturating $[\text{Ca}^{2+}]$; R_{min} is R at zero $[\text{Ca}^{2+}]$; S_{b2} and S_{f2} are the values of the fluorescence at saturating $[\text{Ca}^{2+}]$ and at zero $[\text{Ca}^{2+}]$ at the

Chapter 1. The Ion Calcium: from the Primordial Soup to Signals

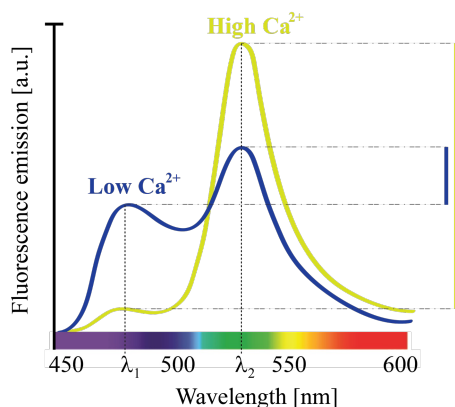


Figure 1.4: Emission spectrum of FRET-based ratiometric dyes, here the cameleon YC3.6. An increase in the $[Ca^{2+}]$ shifts the emission to higher wavelengths, changing the ratio between the emission at two wavelengths λ_1 and λ_2 .

wavelength λ_2 , which is the one used in the denominator. The advantage of this last class of indicators is that they are intrinsically correct, for example, for unequal dye loading, bleaching and focal-plane shifts, as the ratio does not depend on the absolute intensity of the two signals, allowing to calculate an exact value of the $[Ca^{2+}]$. Despite of that, non-ratiometric sensors usually have a stronger fluorescence change when binding to Ca^{2+} , allowing faster recordings, and since just one wavelength is acquired, they require simpler instrumentation and analysis. Moreover, it must be considered that usually only relative $[Ca^{2+}]$ variations are of interest.

1.7.3 Families of indicators

The first two probes based on GFP that has been developed belong to the family of cameleons (Figure 1.5(A)) and are ratiometric: they both rely on the phenomenon of Forster Resonant Energy Transfer (FRET) between two different GFP mutants, whose reciprocal distance changes with the $[Ca^{2+}]$. FRET occurs between an excited donor molecule and an acceptor molecule in the ground state. Depending on the distance between the donor and acceptor, as well as other parameters like the extent of overlap of the emission spectrum of the donor with the absorption spectrum of the acceptor, the quantum yield of the donor and the relative orientation of the donor and acceptor transition dipole, there can be an energy transfer between the two molecules. It is worth noting that FRET relies on a long range dipole-dipole interactions between the

donor and acceptor and consequently the energy transfer by definition takes place without the presence of a photon [49]. In the first cameleon, designed by Tsien and coworkers [56], a blue (or cyan) and a green (or yellow) variants of GFP are expressed at the termini of a construct made of the fusion of the CaM-binding peptide M13 and CaM. An increase in $[Ca^{2+}]$ makes the CaM wrap around the M13 domain, like the tongue of a chameleon, reducing the distance between the two fluorophores and therefore changing colour, thus increasing the efficiency of FRET (Figure 1.4). In FIP-CB_{SM} developed by Persechini [79], the two fluorophores are linked only by the M13 peptide, which elongates when binding to CaM in presence of high $[Ca^{2+}]$, reducing the FRET phenomenon.

All the experiments on plants described in the following Chapters were performed taking advantage of the Yellow Cameleon YC3.6, which is the most popular for plant biology [63], whose spectrum is depicted in Figure 1.4. It has been specifically designed to improve the brightness and energy transfer between the FRET couple, CFP and cpVenus. In fact, with respect to other yellow cameleons, the YC3.6 uses as an acceptor cpVenus, which is a circularly permuted variant of YFP. This chromophore proved to be more resistant to the cellular environment and to have a higher fluorescence expression. More prominently, the relative orientation of CFP and cpVenus transition dipoles is improved, increasing the dynamic range of the indicator. The YC3.6 probe properties that fit well the needs of plant biology can be indeed resumes in: i) high signal-to-noise ratio; ii) high dynamic range; iii) pH stability in the physiological range; iv) an *in vitro* K_d for Ca^{2+} of 250 nM. In this ratiometric indicator, the two fluorescent proteins sandwich the calmodulin and the M13. When there is an increase in the $[Ca^{2+}]$ around it, the M13 domain binds the calmodulin peptide reducing the distance between the two fluorophores and, therefore, increasing the efficiency of FRET.

However, in general one of the main disadvantages of cameleons is their small changes in signal when binding to Ca^{2+} . Besides, their large size and molecular complexity in some cases might weaken their targeting efficiency, though on the contrary the associated low diffusion rate can help when high spatial accuracy is pursued, for example, to localize Ca^{2+} puffs or sparks.

As an answer to these issues, non-ratiometric probes based on a single GFP variant were designed. The general mechanism is the alteration of the pK_a (the pH at which 50% of the probe is protonated) of the fluorescent protein, which follows the binding of Ca^{2+} to CaM, that is in one way or another fused to the GFP. This results in a consistent fluorescence variation in pres-

Chapter 1. The Ion Calcium: from the Primordial Soup to Signals

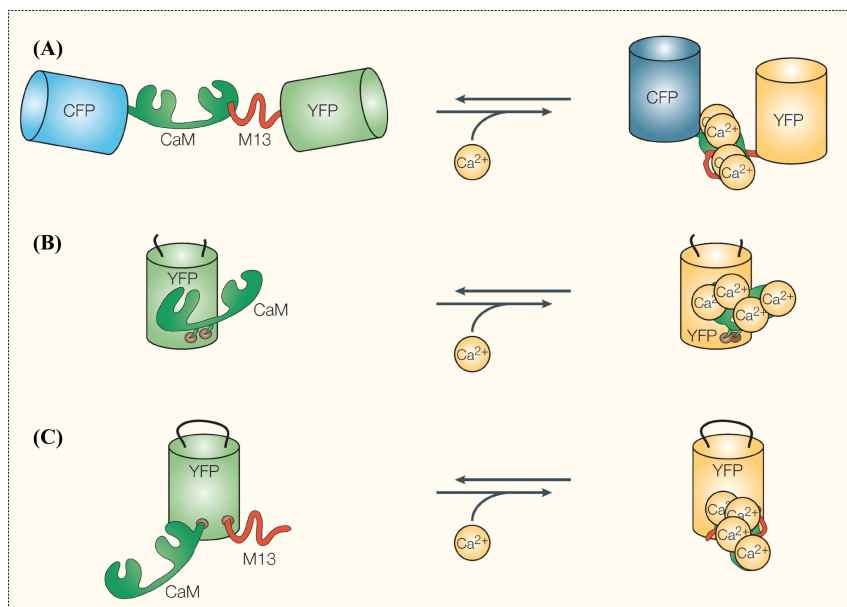


Figure 1.5: Families of GFP-based indicators: in the cameleon (A), a Ca^{2+} -induced interaction between CaM and the CaM-binding peptide M13 increases the rate of FRET leading to a decrease in the fluorescence of the CFP and an increase in the fluorescence of the YFP; in the camgaroo probe (B), the Ca^{2+} -induced conformational change in CaM increases the fluorescence of YFP; the Ca^{2+} -induced interaction between CaM and M13 of pericam (C) leads to changes in the fluorescence characteristics of the cpYFP. Reproduced from Rudolf and coworkers [80].

ence of even subtle changes in the protein structure, which however depends to the compartment pH. Moreover, thanks to the discovery that the termini of a yellow-emitting GFP (YFP) can be rearranged without negatively affecting the fluorescence properties of the protein, CaM started to be inserted within GFP-based proteins themselves. In camgaroos [6] CaM is interleaved in a site in between YFP, which makes its fluorescence “bounce” high when interacting with Ca^{2+} (Figure 1.5(B)). In pericams [62] a variant of YFP is circularly permuted, meaning that a peptide linker is inserted between the termini of the protein and that a new terminal pair is created elsewhere in the sequence, and sandwiched between CaM and M13 (Figure 1.5(C)). There are three main variants of pericam, one of which, known as ratiometric pericam, has an excitation spectrum that shifts on Ca^{2+} binding, thereby allowing ratiometric measurement. The issue with ratiometric pericams is that they must be excited at two

different wavelengths, which makes them not adequate for fast imaging. To the family of pericams also belong GCaMP indicators, single wavelength non-ratiometric sensors based on circularly permuted GFP instead of YFP, where again the termini are concatenated to M13 and CaM [64]. These indicators have improved rapidly, and as an example, the GCaMP5G variant has an improved sensitivity compared to its predecessors, with a fluorescence increase by a factor relative to the baseline up to 1000, with a decay and rise half-time of 667 ± 43 ms and 166 ± 20 ms respectively. At the time of redacting this manuscript, an even more sensitive and faster probe, the GCaMP6, is already available.

So far, most research in Ca^{2+} signalling has been carried out in cultured cells or ex vivo tissues. However, the final goal of modern biology is to investigate life on earth, ultimately researching highly complex systems and whole living organisms. This is probably one of the reasons why the genetically encoded probes are rapidly becoming popular, given that they can be exploited in cultured cells and be ready for the following in vivo measurements. By the way, improving $[\text{Ca}^{2+}]$ imaging means not only to develop new and better probes, but also instruments that can benefit from the innovative probes and that, at the same time, are powerful and flexible enough to permit the study of a whole living specimen.

CHAPTER 2

Light Sheet Fluorescence Microscopy

THE 20TH CENTURY has seen major advances in optical microscopy. The main struggle was to be able to see the smallest details of biological samples. While huge advances in the knowledge of how things are made were achieved, new quests for functional investigation has emerged. Over the past decades, light sheet fluorescence microscopy showed its unique ability to image large biological specimens with single cell resolution and minimum damage, for long time periods, shedding new light on biological functions. In the following chapter, the principles underlying this technique will be discussed with comparison to standard microscopy for life science, and a detailed description of three implementations of light sheet microscopy i.e. static, digitally scanned and two photon light sheet microscopy will be discussed.

2.1 Fluorescence microscopy for calcium imaging

The easiest and most used technique for general-purpose fluorescence imaging is of course epifluorescence microscopy. An epifluorescence microscope is based on a standard microscope, with an incoherent light source reflected by a dichroic mirror making it pass through the objective. At the focal plane of the objective, where the sample is placed, the fluorescence signal is excited and collected by the same objective, which sends it through the dichroic mirror and the tube lens which finally projects it on a pixelated detector. The main issue with this approach is the contribution of out of focus fluorescence, which limits its usage only to thin samples, like cultured cells or tissue slices. Looking at thick samples leads to blurred images, with no possibility of recovering the lost information. Therefore, making an image of a volume requires the elimination of the unwanted photons from out-of-focus regions, operating an optical sectioning of the sample. The sectioning capability provides greater contrast and permits three-dimensional (3D) reconstructions by computationally combining images from different planes of a sample.

The confocal microscope [85] is the most diffused microscope able to do so, which brought a first huge contribution to calcium imaging. Basically, the light from a point source, usually coherent, is focalized on a single point in the focal plane of the objective and a pinhole is placed on an image plane in front of a single-point detector, such as a photomultiplier. The pinhole let only the light coming from the very on-focus plane to reach the detector, while blocking all the rest of the light, as depicted in Figure 2.1(A). The illuminated spot is then scanned across the whole field of view and the complete image is generated by a computer. The scanning can be achieved in two main ways: by using a couple of galvanometric mirrors to actually move the beam in a raster way, or by means of the so-called spinning disk. In this last approach, a rotating disk with multiple pinholes is placed in a position conjugated with both the focal plane of the objective and a pixelated detector, creating an array of excitation spots and of pinholes at the same time. Three-dimensional images can be created by moving the objective in the axial direction. Nevertheless, confocal microscopy suffers from few drawbacks. First of all, the time required for the acquisition of an image is proportional to the number of sampling points that compose it. Since it is a point-scanning technique (or array-scanning with the spinning disk) it is intrinsically slow, and, as the image quality also depends on the pinhole size, obtaining one image can take even few seconds. This means that the sample remains exposed to a large dose of excitation light, with a big

2.1. Fluorescence microscopy for calcium imaging

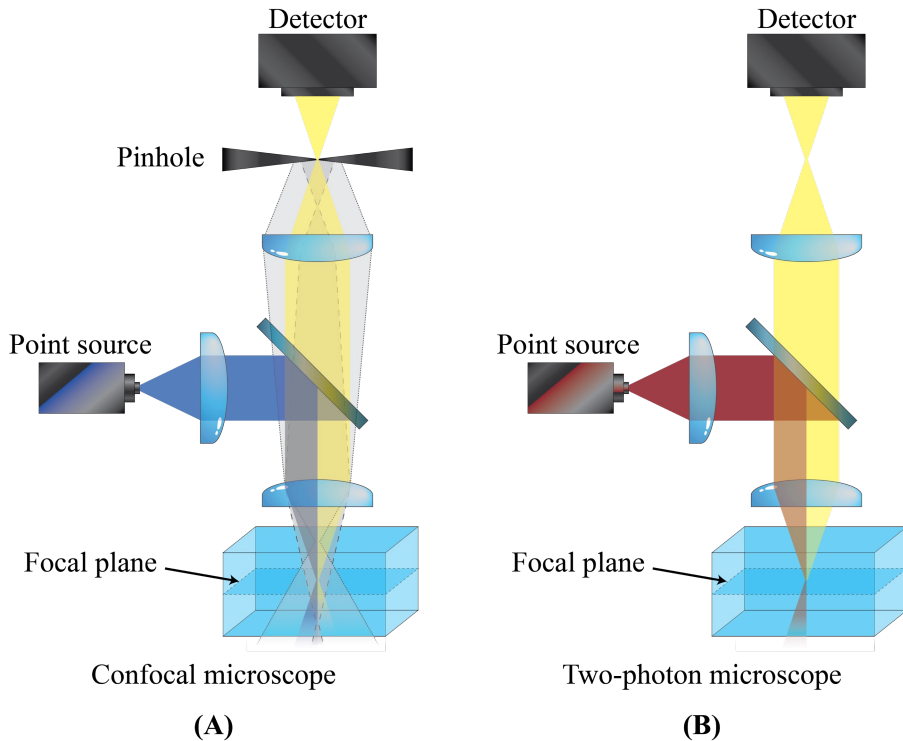


Figure 2.1: Standard point scanning microscopy techniques: confocal microscope (A) and two-photon microscope (B). Note that the fluorescence in (A) is generated also on the cones below and above the focal plane, being rejected later by the pinhole, while in (B) is generated only in the focal point.

contribution to the bleaching of the specimen. To reduce the acquisition time maintaining a good sampling in an image, one can either reduce the field of view or use an even higher and damaging excitation power, but anyway up to a saturation level for the fluorescent molecules. What is more important, out of focus fluorescence is rejected, but still excited: this means that the sample is being bleached on planes that are not even being recorded. Since the excitation light is being absorbed and also scattered by out of focus molecules, the photons that reach the focal plane are only a fraction of the initial ones, further decreasing the total useful signal and the acquisition speed, along with the penetration depth.

A more suitable approach to image thick and scattering media is to avoid the excitation of the out of focus fluorescence from the beginning. This is

Chapter 2. Light Sheet Fluorescence Microscopy

the idea behind two-photon (Figure 2.1(B)) [18] and multiphoton microscopy in general, tools that have become crucial for research in biology in general, and calcium imaging in particular. Two-photon fluorescence excitation consists in the simultaneous absorption of two photons by a fluorophore in a single event. The two photons absorbed have roughly twice the wavelength of the one of single photon absorption. The process is nonlinear, as the probability of this phenomenon to happen is quadratically dependent on the excitation power. This means that to increase this probability a high photon density is needed: this is achievable by focusing the excitation light in a tight, diffraction-limited volume at the focal point of a high numerical aperture (NA) objective, together with a high repetition rate femtosecond lasers for the excitation. These pulsed sources, usually tunable Ti:Sapph laser, provide a high peak intensity while keeping the average power relatively low. In this way, only the fluorophores at the focal point are excited, while the rest of the sample does not absorb any photon. Like in confocal microscopy, the focal point is necessarily scanned over the whole field of view to create the full picture. The purpose of employing the two-photon effect is that the axial point spread function is substantially lower than for single-photon excitation. As a result, the axial resolution is improved, allowing thin optical sections to be recorded without the use of the pinhole. Moreover, since most fluorescent molecules used in biology have absorption spectra in the visible range, the typical light used in two-photon imaging is in the near infrared range of the spectrum. This leads to a higher penetration depth for this technique, as light scattering is proportional to $1/\lambda^4$ and the absorption properties of water, haemoglobin and melanin are minimum in the near infrared region. The weakness in the use of infrared excitation light is the loss in lateral resolution, which is directly proportional to the excitation wavelength.

Although technical improvements (such as the acquisition parallelization [11]) or refinements in measurement strategy [83] (scanning the beam only across area of interest of the field of view) allow to gain in speed while maintaining the sequential scanning, a real jump in the performances could only come from a radical change in the geometry of the microscope.

It is worth mentioning that optical microscopes have an inherent limitation in spatial resolution because of the wave nature of light. The effect of light diffraction limits the optical resolution to approximately half of the wavelength of the light used, meaning that many fine cellular structures cannot be resolved. In 1994 Stefan W. Hell, who received the Nobel Prize in Chemistry in 2014, and Jan Wichmann [33] developed the STimulated Emission Depletion

2.2. A novel approach to microscopy

(STED) microscopy, creating super-resolution images by the selective deactivation of fluorophores. In 2006, three research groups independently demonstrated super-resolution microscopy using high-precision localization of single fluorophores, named as PhotoActivated Localization Microscopy (PALM) [10] STochastic Optical Reconstruction Microscopy (STORM) [81] and Fluorescence PhotoActivation Localization Microscopy (FPALM) [35]. These techniques allowed to look at cellular structures with a resolution of even 20 nm, but at the cost of the acquisition speed, which is limiting their diffusion for *in vivo* imaging.

2.2 A novel approach to microscopy

2.2.1 Light sheet fluorescence microscopy

In the 80s the confocal configuration led to a breakthrough in microscopy, improving resolution and introducing optical sectioning. Confocal imaging relies on diffraction-limited scanning spot and spatial filtering, which make the method intrinsically slow and prone to photodamage, due to the high light dose required. As already stated in Chapter 1, life science and in particular calcium imaging require multiscale observation from cell level to systemic level of entire organs, which means having a wide Field Of View (FOV) with still at least single cell resolution and sectioning capability. Since we also want to look at dynamic behaviours, the image acquisition must be fast enough to record them, without damaging the sample.

Confocal imaging limitations can be overcome by using a different geometry of the microscope. A promising approach relies on the selective excitation of a thin plane of the sample, matched with the focal plane of a wide field objective. It is then possible to image an entire plane of the sample in one shot using a pixelated detector, still preserving optical sectioning. This is the principle behind Light Sheet Fluorescence Microscopy (LSFM), a technique based on two different optical paths for the excitation and the detection paths, as shown in Figure 2.2. In LSFM a thin sheet of laser light illuminates the sample, while the fluorescence is collected orthogonally to the excitation path and recorded by a camera.

This geometry gives an inherent sectioning capability even in its simplest configuration, with no need for pinholes or expensive femtosecond lasers. By moving the specimen through the light sheet or the light sheet through the sample, many 2D images at different depth can be acquired, allowing the reconstruction

Chapter 2. Light Sheet Fluorescence Microscopy

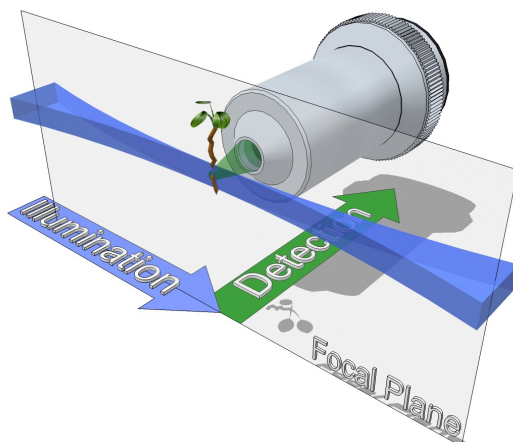


Figure 2.2: *Light sheet fluorescence microscopy principle: a thin sheet of laser light illuminates the sample, while the fluorescence from the whole bidimensional plane is collected orthogonally to the excitation path.*

of the sample in 3D. Since this technique is not point scanning, the field of view and the frame rate are not (at least directly) related. In fact, the first depends on the FOV of the observation objective, while the frame rate primarily depends on the signal to noise ratio at the imaging detector, which in turns depends on the excitation power and on the camera performances. The recent development of objectives with intermediate magnification and high NA and especially of scientific cameras with very large sensor, high speed and high sensitivity have been crucial for the development of LSFM, maximizing the efficiency of this technique and helping in obtaining a high data rate. In particular, new pixelated detectors provide a parallelized data acquisition which gives an advantage of more than 500 times with respect to standard confocal and two-photon fluorescence microscopes, not to mention the far higher dynamic range.

The blade of laser light can be generated using different methods, usually involving gaussian beams, shaped in a plane-like manner through cylindrical lenses or scanned rapidly through galvanometric mirrors to create *quasi*-planar excitation. Therefore, the light sheet can be described in terms of its waist, or minimum thickness, and of its Rayleigh length, that is the distance over which the thickness can be considered approximately constant. The beam profile w (Figure 2.3) evolves along the x direction as

2.2. A novel approach to microscopy

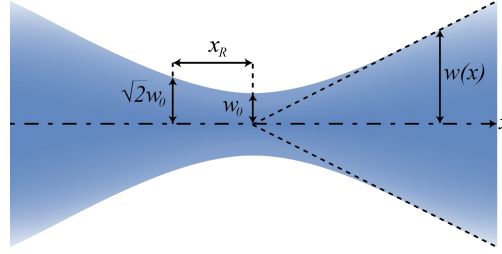


Figure 2.3: Gaussian beam profile: $w(x)$ is the evolution of the beam profile along the x direction, w_0 is the beam waist, x_R is the Rayleigh length.

$$w(x) = w_0 \sqrt{1 + \left(\frac{\lambda x}{n\pi w_0^2} \right)^2} \quad (2.1)$$

where n is the refraction index of the medium, $w_0 = \frac{\lambda}{\pi NA}$ is the beam waist and λ is the laser wavelength. The Rayleigh length is the path over which the spot size increases by a factor $\sqrt{2}$ with respect to the waist and, according to Eq. 2.1, is given by

$$x_R = \frac{n\pi w_0^2}{\lambda} \quad (2.2)$$

It is clear that the smaller w_0 , the shorter is the Rayleigh length and the more the beam diverges. Since the thickness of the light sheet defines the axial resolution (usually 2 – 6 μm) of the microscope, the trade-off between the light sheet waist and its Rayleigh length must be chosen wisely, in order to have reasonably homogeneous imaging conditions and a good axial resolution across the required field of view. The axial resolution in LSFM is in theory better than that of epifluorescence and two-photon microscopy and in some cases ($NA < 0.8$ assuming a FOV of 66 μm .) it can be better than that of confocal microscopy [22].

Through LSFM it is thus possible to image a very large field of view (hundreds of microns to millimetres) with still a theoretical diffraction-limited lateral resolution, which usually spans from 0.5 to 2 μm and depends primarily on the NA of the detection optics and the wavelength of the fluorescence emission, like in epifluorescence microscopy. In practice, however, the lateral resolution of LSFM is often better than that of epifluorescence, because of the optical sectioning, which improves the contrast and allows resolving fine structures that would be hidden by the out-of-focus haze. Furthermore, thanks to the high

Chapter 2. Light Sheet Fluorescence Microscopy

signal-to-noise ratio of LSFM, the images result particularly appropriate for image deconvolution, which provides a further increase in resolutions. Finally, it is worth noting that in LSFM, differently from confocal microscopy, the lateral and axial resolutions are decoupled. This means that even if the detection objective had a long focal depth, the sectioning capability would not be affected.

In addition to the benefits in terms of imaging performance, the main advantage is for the sample preservation. With conventional and confocal microscopy, the sample absorbs unnecessary radiation, since the whole specimen is illuminated in the axial direction while looking at a single focal plane (Figure 2.4). In LSFM, only the fluorophores in the plane of interest are illuminated, which minimizes the effects of phototoxicity and photobleaching, opening new opportunities for long recording. In fact, thanks to the low dose of light and the fast acquisition through cameras, it is feasible to make time-lapse imaging for hours without damaging the sample. If we consider a 3D stack, the advantage of LSFM, in terms of light dose, over confocal microscopy can be roughly expressed by a factor n , given by the ratio between the depth of the volume to be imaged and the thickness of the light sheet. In fact, confocal microscopy illuminates all the volume of the sample every time it images each of the n planes. For a $500\ \mu\text{m}$ volume and a light sheet of $5\ \mu\text{m}$, the reduction of photodamage brought by LSFM is of 100 times compared to confocal microscopy.

As a final point, the special geometry of light sheet opens the possibility to reinvent the conditions in which the sample is held during an experiment, although someone could say that changing the way of holding the specimen from the century-old well-established glass slide can be a disadvantage. As a matter of fact, the excitation and detection paths can be rotated creating new space for the sample holder, in order to keep a living organism as much as possible in physiological conditions. For example, plants can be held vertically in a medium-filled chamber, while fish embryos should be kept horizontal. In fact, it could be said that LSFM places the sample in the centre of an experiment and arranges the optics and mountings around it.

Obviously, LSFM has some drawbacks: because of the side illumination, point like absorbers in the sample cast shadows behind them within the light sheet, while scattering makes the image of planes deep inside the sample dark and blurred. As a result, the lateral image quality is, on average, worse than that of a confocal microscope. Last but not least, the image data size is large, the stacks are huge, and an uncontrolled recording not guided by well thought questions can easily lead to huge amount of data (even 300 GB per hour), that

2.2. A novel approach to microscopy

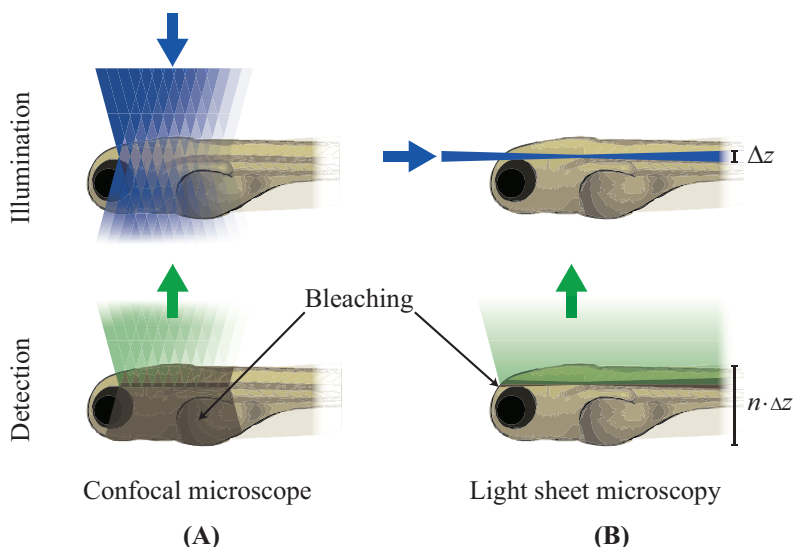


Figure 2.4: *Advantages of LSFM: while confocal microscopy (A) is point scanning and illuminates the whole volume of the sample, with useless photodamage for the sample, LSFM (B) has an intrinsic sectioning capability and induces a reduced photodamage.*

not only have to be stored but also processed.

2.2.2 The long story of LSFM

The first description of a light sheet microscope dates back to 1902 and can be found in the work of an optical physicist and a physical chemist, Siedentopf and Zsigmondy [88], who were trying to visualize small colloidal gold particles. Darkfield condensers were not powerful enough at the time, so they tried to illuminate their particles from the side. In order to illuminate a well-defined volume, they created somehow a thin sheet of light by using lenses, slit apertures and a second objective held at 90° with respect to the standard one. However, laser light was not available at those times and the so-called “ultramicroscope” (Figure 2.5) did not stimulate further development in the microscopy community, which focused instead on more proficient darkfield condensers. Light sheet fluorescence microscopy was employed much later in the sixties to image large macroscopic specimens in the field of macrography and photomicrography. Nonetheless, only the imaging of surface structures of minerals, insects and metallic objects was realized.

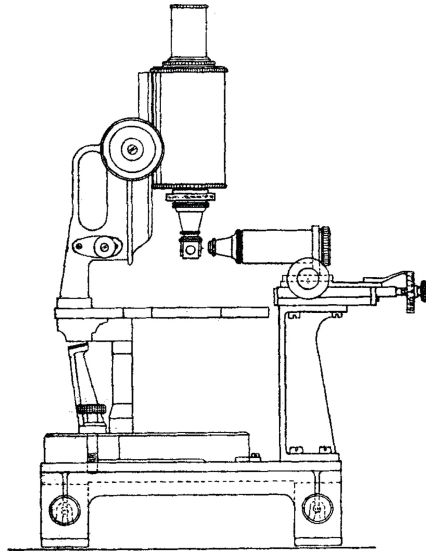


Figure 2.5: *The original design of the ultramicroscope by Zsigmondy and Siedentopf from their paper dating back to 1902. Reproduced from Zsigmondy and Siedentopf [88].*

The first relevant biological use of such a technique was made after David Burns saw a sectioned pig embryo on the cover of a photomacrography book (White 1987). In 1993, Arne Voie with David Burns and Francis Spelman reported the first application of light sheet illumination for fluorescence excitation in a biological specimen. They called the technique Orthogonal Plane Fluorescence Optical Sectioning (OPFOS) and used as a sample a guinea pig cochlea [99], a complex organ because of its spiral anatomy. Since the cochlea is also thick and scattering, they made it transparent using a clearing solution developed by Werner Spalteholz in the beginning of the century [90], and afterwards they made it fluorescent by immersion in rhodamine. In this way, they obtained quantitative morphological information of the inner ear, difficult to obtain with histological methods. One year later, a confocal microscope with a second oblique illumination objective called confocal theta microscope, was developed in the laboratory of Ernst Stelzer, who was carrying on studies on axial resolution improvement. This laid the foundation for their subsequent version of a light sheet fluorescence microscope called Selective or Single-Plane Illumination Microscope (SPIM), which one decade after attracted the interest of developmental biologists [38]. LSFM proved extremely well suited for

2.2. A novel approach to microscopy

investigating embryonic development, like for example, the transgenic GFP-expressing *medaka* fish larva and the *Drosophila melanogaster* embryos imaged for over 17 hours. In this case, the team combined multiple views acquired sequentially in order to image large fixed samples, with an axial resolution of $6\ \mu\text{m}$ and a field of view of $1.5 \times 0.9\ \text{mm}^2$. From this on, the appealing of the technique grew exponentially and a lot of research was done around this new microscopy idea, both for *in vivo* and *ex vivo* cleared samples. About this latter typology of experiment, it must be said that LSFM gave new life to the research on clearing methods, promoting even the discovery of a method to maintain GFP expression in cleared specimens [17, 21]. Especially for *in vivo* measurement, the great improvements brought by LSFM are the high imaging speed, high signal-to-noise ratio and low levels of phototoxicity, not counting its simplicity and low cost compared to confocal microscopes. This is way a lot of research is being done on light sheet-based microscopy, whose basic concepts and advanced implementations will be highlighted in the following paragraphs. Since the illumination and the detection stages are decoupled, they will be separately discussed.

2.2.3 Different illumination techniques

Single-Plane Illumination Microscopy

One elementary way to generate the excitation light sheet is the so-called single-plane (or selective-plane) illumination, from where it comes the name Single-Plane (or Selective-Plane) Illumination Microscopy (SPIM) [30, 38], which employs a cylindrical lens as a core component. Through that, a collimated laser beam is focused along the direction parallel to the detection axis, while it remains collimated along the orthogonal axis, as shown in Figure 2.6(A). The light sheet is indeed static, and no optical parts need to be moved during the acquisition. This scheme is well suited to be used with massively parallel detectors, like fast cameras. To match the required field of view, the beam must properly expanded before impinging on the cylindrical lens, while to reduce the illuminated area, the beam can be easily cropped with apertures positioned in proper image planes. To get 3D information, the sample must be scanned through the light sheet by means of a translation stage, which has to be synchronized with the camera. In some cases the oscillations induced to the sample may affect the stability of the recording or may alter the functional state of the specimen, that can be a living and behaving organism. The strategy with almost no moving parts is particularly useful when implementing

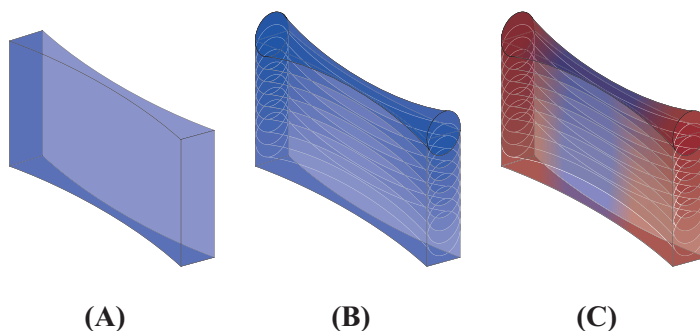


Figure 2.6: *Different types of light sheet: static light sheet (A); digital scanned light sheet (B); two-photon digital scanned light sheet (C).*

miniaturized instruments.

Digital scanned laser light sheet

The second basic approach is exploited by the Digital Scanned laser Light sheet based fluorescence Microscope (DSLIM) [43]. The light sheet is created by focusing a gaussian beam along a line and rapidly moving it through the focal plane of a large NA detection objective (Figure 2.6(B)). This can be accomplished for example by appropriately tilting a galvanometric mirror, whose angular displacement is converted into position shift through a scan lens and then pivoted by a tube lens on the back-focal plane of an objective, as shown in Figure 2.7. This objective must have a low NA to get a good compromise between the light sheet waist and the Rayleigh length. To obtain a 2D image, a camera synchronized with the scanning elements integrates the signal while the laser illuminates with a constant scan speed the whole field of view during the exposure time. In contrast to SPIM, the illumination intensity profile is more uniform, resulting in fewer artifacts: each voxel line in the specimen is excited by the same light intensity, a key requirement for quantitative imaging of large samples, whereas in SPIM, the illumination is reminiscent of its gaussian profile. Moreover, DSLIM does not rely on apertures to shape the light sheet profile, but it is possible to set the field of view by controlling the scan mirrors via computer, which lessens diffraction effects. In fact, cropping the beam in one dimension to reduce its size results in side lobes that increase the light sheet thickness. The sequential line illumination of DSLIM implies that only a stripe of the sample is excited at a time. Hence, the light intensity must be higher, compared to SPIM, in order to get the same fluorescence signal in

2.2. A novel approach to microscopy

the same exposure time. If we consider an illumination field Nw_0 large, where w_0 is the light sheet waist and N the number of lines to cover the whole field (for a $600\ \mu\text{m}$ field of view and a $3\ \mu\text{m}$ -thick light sheet N would be 200), the excitation intensity for SPIM and for DSLM is

$$I \propto \frac{P}{w_0^2} \quad (\text{scanned light sheet}) \quad (2.3)$$

$$I' \propto \frac{P}{Nw_0^2} \quad (\text{static light sheet}) \quad (2.4)$$

where P is the same average excitation power. This means that, to obtain the same fluorescence signal $S \propto P/Nw_0^2$, the excitation intensity in DSLM must be N times higher. The main limitation of this approach is that the exposure time of recent cameras can be shorter than the scan time of galvanometric mirror, while with a static light sheet it is possible to take full advantage of fast cameras and freeze rapid dynamics within big samples. Three-dimensional acquisitions can still be done by moving the sample through the light sheet or by using a second galvanometric mirror, which displaces the beam orthogonally, with respect to the first scanning direction. Obviously, the detection objective must be shifted in order to follow the light sheet: indeed, it is usually mounted on a piezoelectric stage, synchronized with the moving mirrors. This approach, though more complicated from a technical point of view, leaves the specimen steady in a less stressed and more physiological condition. Lastly, DSLM permits to create more easily structured illumination patterns and other illumination strategies used to improve the penetration depth and contrast in highly scattering samples, although these have been demonstrated also for SPIM [12].

Two-photon light sheet

One possibility that can be applied to both the discussed techniques to increase the penetration depth and reduce scattering effects, especially to image thick and highly scattering samples, is to combine LSFM and two-photon excitation provided by high repetition rate IR femtosecond lasers [92]. In the IR range, the scattering of the excitation light is smaller than at visible wavelengths, preserving the light sheet thinness in biological tissues. Moreover, the quadratic dependence of the fluorescence signal on the excitation light intensity confines the excitation volume only in the part of the beam at highest energy density (Figure 2.6(C)), preserving the axial resolution and making scattered photons of the illumination beam less important. Therefore, the background fluorescence is lower, enhancing the lateral resolution and contrast. Moreover, many

Chapter 2. Light Sheet Fluorescence Microscopy

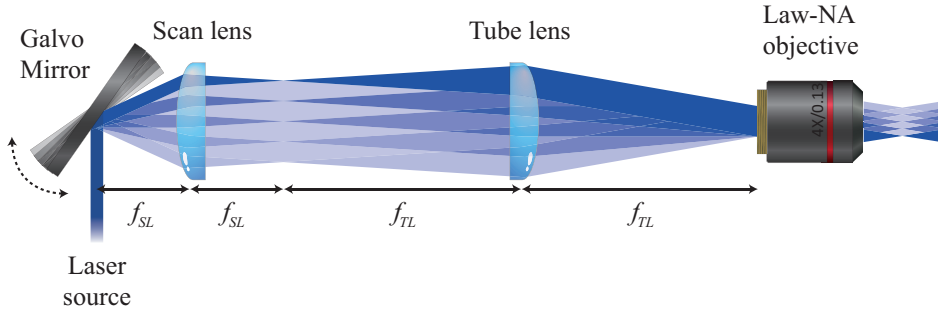


Figure 2.7: Principle of DSLM: the light sheet is created by appropriately tilting a galvanometric mirror, whose angular displacement is converted into position shift through a scan lens placed at his focal distance f_{SL} from the mirrors. A tube lens, positioned at $f_{SL} + f_{TL}$ from the previous optic element, pivots the beam to the entrance pupil of a low-NA objective, placed at its focal distance f_{TL} .

animals cannot see IR light, so a two-photon excitation is more convenient when performing behavioural experiments without the impact of the visible laser light to the animal response.

This concept has been applied to static light sheets (2p-SPIM) in living *C. elegans* specimens [69]. By the way, the field of view was reduced because of the non linear nature of the phenomenon, fact that was somehow compensated by the longer penetration depth of the IR excitation light, with indeed no big improvement. More significantly, the fluorescent was rather low because the peak power of the excitation laser was not enough to achieve high two-photon absorption efficiency which depends on the square of the intensity. Therefore, in order not to increase the photobleaching nor the heating of the sample by simply rising the laser power, the exposure time had to be increased, fact that limited the maximum imaging speed of the 2p-SPIM. Two-photon DSLM [92] (here called 2p-DSLIM) overcomes this problem thanks to the high power densities achieved with the scanned pencil-focused laser beam, which enables to reach higher local excitation intensity for the same average excitation power. Taking into account that the intensity profile of the beam is defined as

$$I(r, x) = \frac{2P}{\pi w^2} e^{-2r^2/w^2} \quad (2.5)$$

where r is the radial dimension in the plane orthogonal to the propagation of the illumination beam, the two-photon excited fluorescence signal S_{2p} becomes

$$S_{2p} \propto \frac{1}{N} \cdot \frac{4P^2}{\pi w^4} e^{-2r^2/(w/\sqrt{2})^2} \quad (\text{scanned light sheet}) \quad (2.6)$$

2.2. A novel approach to microscopy

$$S'_{2p} \propto \frac{1}{N^2} \cdot \frac{4P^2}{\pi w^4} e^{-2r^2/(w/\sqrt{2})^2} \quad (\text{static light sheet}) \quad (2.7)$$

thus, with the same amount of average excitation power P , 2p-DSLM gives a signal N times larger, with N in the range of a few hundreds.

Comparing the resolution and field of view in 2p-DSLM and one-photon DSLM (1p-DSLM), in the latter the fluorescence signal is proportional to the illumination light intensity $S_{1p} \propto I$ while the wavelength is about half the one of two-photon excitation $\lambda_{1p} \simeq \lambda_{2p}/2$. Hence, to get the same axial resolution, i.e. the same width of the gaussian signal, the two exponentials must be the same, condition that gives

$$\frac{4r^2}{w_{0,2p}^2} = \frac{2r^2}{w_{0,1p}^2} \quad (2.8)$$

Given the definition of w_0 , to get the same axial resolution then $NA_{2p} \simeq \sqrt{2}NA_{1p}$. In this situation the field of view is the same for the two modalities, but the ratio of the average signal at the centre and at the edge is 2 for 1p-DSLM and 4 for 2p-DSLM. This variation needs to be taken into account when performing absolute quantitative analysis of the fluorescence emission.

Compared to the one-photon counterpart, the main disadvantage of two-photon LSFM arises from the significantly higher excitation peak intensity, which leads to more potential photodamage, although this latter should be compensated by the longer illumination wavelength. Since 2p-SPIM has a lower peak intensity, the phototoxicity should be lower, but the heating effect could be higher compared to the scanned light sheet. Whether one excitation regime is more suitable for a specific imaging application has therefore to be determined according to the sample, depending on the type of fluorophore as well as the water content. Also, because of the high and localized peak energy, pigmentation or highly absorbing features of a specimen can heat up or even reach the ablation threshold, with irreversible damages. Last but not least, another disadvantage of 2p-DSLM that should not be forgotten comes from the high cost of ultrafast lasers and the lower availability of suitable fluorophores.

Further improvements of the illumination path

In large and highly scattering samples, the image quality deteriorates with the propagation of the light sheet inside the tissue. The amount of light reaching high penetration depth may be reduced not only because of scattering of illumination beam, which blurs the image reducing the contrast, but also because of its absorption. This latter makes the light sheet attenuate along its path,

Chapter 2. Light Sheet Fluorescence Microscopy

leading to a darker image in the exit side of the light sheet. If the absorption centres are really concentrated (i.e. pigmentation), they cast shadows behind them, obscuring part of the sample (Figure 2.8(B)). In case they move, like red blood cells inside a vessel, the shadow could create artifacts when looking at signal dynamics.

Multidirectional SPIM (mSPIM) provides an equally illuminated focal plane by sequentially illuminating the sample from two opposite sides [8, 21] (Figure 2.8(A)) and/or by rotating the sample. This reduces both absorption and scattering artifacts of the excitation beam. The collected images must then be combined in post processing. A further method which eliminates most of the stripes and shadows artifacts is tilting the light sheet pivoting it on its focus, which coupled with the mSPIM obviously works even better [37] (Figure 2.8(C)). Anyway, proper alignment of two different light sheets at the same time is not that straightforward.

Other advances more specific to DSLM are the application of structured illumination to light sheet microscopy: Bessel beams, adaptive optics, pulse splitters and combinations of these. In structured-illumination microscopy based on scanned light sheet [42] the sample is illuminated with a periodic and symmetric pattern, typically sinusoidal. Multiple images are acquired with different modulated patterns, thus the resulting image is a product of the illumination pattern and the fluorescence of the sample. By demodulating the acquired signal, an image with improved resolution can be obtained, as previously shown with a SPIM setup [12]. Self-reconstructing Bessel beams [24] are beams that do not diffract and spread out as they propagated. They can be created using annular apertures or axicons before scanning the beam and provide a substantial increase of the axial resolution, of the depth of focus, and hence of the field of view, in highly diffusive media. Thanks to their “self-healing” nature, they reconstruct their initial profile behind obstacles, suppressing shadow artifacts. However, the photons necessary for “self-healing” are contained in Bessel rings that extend radially from the central spot and illuminate out-of-focus regions, as pictured in Figure 2.8(E), resulting in lower contrast images. A good way to get rid of this issue, is to combine the benefits of Bessel beams and two-photon fluorescence excitation [23]. In this way, thanks to the quadratic dependence of the fluorescence signal on the illumination intensity, the fluorescence from the rings is suppressed, which leads to an increase of nearly two times in axial resolution and of 5-10 times in contrast, with respect to linear Bessel beam excitation. Moreover, thanks to the improved thinness of the central spot, Bessel beams in general are well suited for confocal-line detection, where out-of-focus

2.2. A novel approach to microscopy

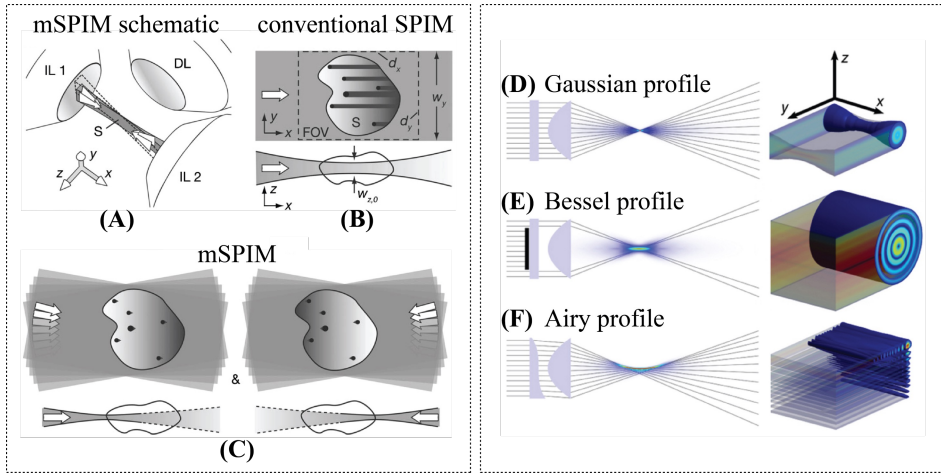


Figure 2.8: Further improvements of the illumination path: schematic of mSPIM (A); shadows and attenuation across the FOV due to the parallel illumination of conventional SPIM (B); reduction of shadow and attenuation artifacts by two-sided and pivoted light sheet illumination (C); adapted from Huisken and Stainier [37]. Generation of conventional gaussian (D), Bessel (E) and Airy profile (F); adapted from Vettenburg and coworkers [96].

fluorescence excited by the ring system is largely blocked. The confocal line detection can be achieved by a slit in the detection path or cleverly by rolling shutter modalities of new cameras, where a single line of active pixels is synchronized with the scanned beam.

Other improvements arise from the application of wavefront control. Liquid crystal spatial light modulator (SLM) or custom designed cubic phase mask can be used to generate Airy beams [96], another type of propagation-invariant intensity profile that exhibit “self-healing” whose profile is shown in Figure 2.8(F). In contrast to the Bessel beam, the Airy beam does not need to be scanned to create the light sheet and shows an even longer depth of field. Moreover, as in all microscopy, the variations in the refractive index of the specimen induces changes to the light path, creating aberrations in the final image. Adaptive optics like acousto-optic deflectors (AOD) and deformable mirrors and have been used to compensate even for complex wavefront distortions (waoSPIM, [39]).

Another series of technical advances include the combination of light sheet microscopy with: i) the principle of stimulated emission depletion (STED) to

Chapter 2. Light Sheet Fluorescence Microscopy

improve the axial resolution [27]; ii) the fluorescence correlation spectroscopy method to measure diffusion properties of small particles in living embryos [101]; iii) tunable lenses to rapidly change the focal length along the illumination and detection paths; iv) the miniaturization of system, for example by implementing all the components on lab-on-a-chip, for high throughput analysis.

2.2.4 Light sheet detection

The detection system of light-sheet microscopy is basically the same of an epifluorescence microscope. It mainly consists of an objective, an emission filter, a tube lens and a camera. The axial point spread function of the detection objective together with the thickness of the illumination determine the axial resolution of the recorded image. In the case of the basic SPIM, all the parts are fixed, while in the case of DSLM the detection objective is mounted on a piezoelectric stage synchronized with the galvanometric mirrors to adjust its position accordingly to the light sheet translations along the detection axis for 3D imaging. Moreover, the camera acquisition must be synchronized with the oscillation frequency of the galvanometric mirrors, that must complete an integer number of scans during the exposure time. The recent improvement in semiconductor technology led to the development of a new class of scientific cameras (CCD, EMCCD, sCMOS) with very large sensor, high speed and high sensitivity. The new pixelated detectors can record images of 1024x1024 pixels at a rate of 1000 frames per second (fps), leading to an acquisition rate of 1050 million pixels/sec. Such performances demonstrated a key factor to allow and boost the development of LSFM. State-of-the-art confocal and two-photon microscopes record images of 512x512 pixels at 5 fps (and at 120 fps with spinning disk), corresponding to 1.3 million pixels/sec (31 million pixels/sec with the spinning disk). In a nutshell, LSFM is 500 times faster than standard confocal and two-photon fluorescence microscopy and is still 30 times faster than spinning disk confocal microscopy. Moreover, this type of acquisition provides a high dynamic range since the recorded images are up to 16 bits, providing images with 65536 gray levels, a big improvement compared to the 6 – 8 bits and 64 – 256 at best of confocal microscopy.

The detection path can be enriched with the acquisition of more than one wavelength by adding a second camera and a dichroic mirror, which creates two replicas of the image based on the different spectral content. Another approach to spectral imaging uses a dual wavelength viewer, which after separating the

2.2. A novel approach to microscopy

two images by a dichroic mirror focalizes each of them simultaneously on half sensor of a single camera, without the need of any synchronization.

Another improvement of the detection path is aimed to moderate the scattering of the fluorescence signal. In fact, the thicker the sample, the higher the volume the emitted photons have to go through in order to reach the detector. A “multiview” approach [47] reduces this blurring effect by adding a second detection path opposite to the first one and/or by rotating the sample to get different views of the specimen. In this way, the fluorescence photons will travel across a thinner sample thickness. Lastly, confocal detection can be made by using a the so-called rolling shutter, an acquisition modality implemented in new camera where only one pixel line is active and moves following the pencil of light of DSLM. This technique is usually coupled with Bessel illumination and helps in getting rid of scattered photons. However, both Multiview and confocal approach improve the image at the cost of a speed reduction.

Development of pixelated sensors

The great progress in imaging detectors occurred in recent years is a major key factor that has allowed and fostered the development of LSFM. Amongst the variety of devices presently available for scientific imaging, the ones used in light sheet microscopy belong to two major families, namely CCD and CMOS. Even if great differences exist between the two technologies, they share an important common feature. In fact, these pixelated imaging detectors are based on the charge storage capability provided by the depletion layer of a properly biased semiconductor substrate. The electrons generated by photons absorbed by silicon are accumulated in each pixel of the sensor proportionally to the light intensity. Then, after the exposure of CCDs, a charge transfer process takes place to move the electrons accumulated in the matrix of sensitive elements to an equal matrix of charge storage, which is arranged in a different architecture according to the device type: either frame transfer or interline transfer (Figure 2.9). The readout process continues with the sequential shift of the charges stored in all the pixels toward a unique charge-to-voltage conversion unit. The readout circuit provides an analogue signal that is buffered and amplified before conversion to a digital output. In scientific grade CCDs, which are usually cooled to reduce the dark current down to a fraction of $e^-/(\text{pixel}\cdot\text{s})$, the operative frequency of the readout circuit is selectable and sets the main source of noise. In CMOS sensors, at variance with CCDs, each pixel has its own charge-to-voltage conversion unit, and the sensor often includes amplifiers,

Chapter 2. Light Sheet Fluorescence Microscopy

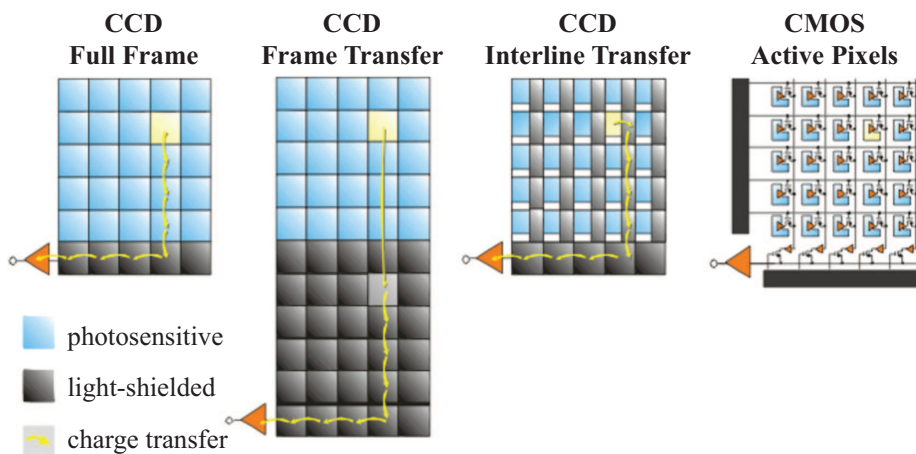


Figure 2.9: Representative images of the principal detectors for imaging.

noise-correction, and ADC circuits, so that the chip outputs digital signals. These additional functions increase the design complexity and reduce the area available for light capture, affecting the fill factor. Since each pixel does its own charge-to-voltage conversion, the uniformity is lower. Yet, the readout is massively parallel, which allows higher speed compared to CCDs. Moreover, CMOS sensors are more versatile than CCDs for advanced windowing and binning. The first feature is exploited to increase the frame rate, while the latter is used to reduce the effective readout noise (at a price of a lower spatial resolution) by combining the charges of adjacent pixels. The sensors of both families can be designed for higher quantum efficiency and wider spectral sensitivity through the back thinning technology, which allows light to enter the sensor from the substrate side, with direct access to the charge accumulation layer, thus reducing photon loss.

Further, the technology that gives the best performance in terms to signal to noise ratio is the Electron Multiplication CCD (EMCCD). In EMCCD the readout register that is devoted to transfer the charge of each pixel to the output node is operated with high voltage bias in such a way that electron multiplication takes place by impact ionization. This provides a tunable gain that can be high enough (e.g. X100) to make the readout noise negligible. High gain leads to single photon sensitivity reducing the noise close to the quantum limit set by the poisson statistic of photons.

Finally it is worth doing a brief comparison of the two detectors families for scientific applications. In general, CCDs provide lower noise, especially in

2.2. A novel approach to microscopy

the EMCCD configuration, better uniformity and higher dynamic range. Yet, high-end devices are still expensive. CMOS sensors, on the other hand, grant higher frame rate, great pixel density, unbeatable versatility and, last but not least, lower cost. For these reasons, CMOS sensors are widening their share in scientific applications.

The major strengths of the CMOS technology make these sensors definitely more suitable than CCDs for LSFM, because of the high speed and the advanced operating modes that include the running shutter, an important feature in some DSLM configurations, as it has been previously mentioned.

CHAPTER 3

Calcium Dynamics in Plant Root

IMPROVING CROP YIELDS and their tolerance to diverse stresses is a global challenge to face population increase. In order to learn more about how plants grow and sense the environment, a model specimen, *Arabidopsis thaliana* was studied with selective plane illumination microscopy. The attention was first focused on the root tip to evaluate the systemic and cellular response to different applied stimuli. Root hairs oscillation were then analysed to understand the role of specific gene expressions on the healthiness of the growth.

The project is a collaboration with Alex Costa from Università degli Studi di Milano, who took care of the whole biological development.

3.1 Introduction

3.1.1 From the improvement of crops to the imaging of roots

Agriculture distribution on the earth surface is effected by environmental factors like water distribution, ground nutrients concentration, microbes temperature, etc. The identification of the physiological mechanisms behind plant adaption to adverse conditions is essential for future improvement of crop species in their tolerance to diverse stresses. Plants are indeed sessile organism living in variable conditions. For plants, the constant sensing of the outer environment is critical: external stimuli have to be perceived and transduced to prompt rapid responses as well as long-term acclimatization. A multifaceted second messenger in plants is the ion Ca^{2+} . It takes part into different regulatory processes [20, 48] and is considered to play a central role in transducing environmental and endogenous signals in order to regulate defense-related gene expression, developmental processes, biotic and abiotic stress responses, symbiotic plant-microbe interactions, water level regulation.

In fact, plant cells react to various environmental stimuli, like light, temperature, hormones, microbes, and touch, by changing the intracellular free Ca^{2+} concentration. Each external stimulus locally induces oscillations of the cytosolic $[\text{Ca}^{2+}]$ that vary in amplitude, duration and frequency, with a specific Ca^{2+} fingerprint, building up the stimulus related “ Ca^{2+} signature”. It is now clear that Ca^{2+} signalling is one of the expedients that plants developed to adapt to a changing environment, but identifying the genes that encode specific Ca^{2+} signatures remains one of the focal point of plant research.

Interestingly, the healthy growth of root hairs has been shown to reflect the growing status of the whole plant, since they are responsible for nutrient uptake and for plant-soil interactions. Root hairs are single cells elongating at the tip. Previous work done on other apical-growing cells have shown that their tip growth is Ca^{2+} -dependent, which leads to the hypothesis that this is also the case for root hairs (see Section 1.5). However, root hairs have the complication of a 3D development all around the root.

Among all the possible plants, *Arabidopsis thaliana* emerged as a model in the plant biology community mainly thanks to its advantages for genome analysis. Interestingly, it was found that the *Arabidopsis* genome has 20 genes encoding for putative ionotropic Glutamate-Like Receptors (GLRs) [50]. Screening of GLRs expression level in plant root led to the observation of a strong expression for some of them in the root hairs, whose growth is an indicator of health

and adaption capability. In addition, in the animal central nervous system, the ionotropic glutamate receptors are ligand-activated ion channels mediating neurotransmission [73]. The analysis of Arabidopsis GLR members suggested that plant and animal GLR genes diverged from a common ancestor. By the way, up to now only few Arabidopsis GLRs have extensively been studied and, for many of these receptors, neither their physiological roles nor their intracellular localization is known.

In order to be able to study with imaging methods such a variegate scenario, a technique which allows the observation of a whole tissue or organ of a plant in condition as physiological as possible at high spatial resolution and over various time scales, from seconds to days, is required. Light sheet fluorescence microscopy has proved particularly suitable to accomplish these requirements. In the following, work done through LSM on the study of Ca^{2+} fingerprints and of its role in root hair growth, with a glance to one GLRs knock out mutant, will be described.

3.1.2 State of the art of calcium imaging in plant biology

For decades the golden standard for the study of the activity of ion channels in plants was the complex and invasive electrophysiology. The arrival of GFP and fluorescence-based sensors revolutionized also plant biology, opening the possibility to follow signalling dynamics with cellular and subcellular resolution over a wide population of cells. Thanks to fluorescence imaging, the type of questions that could be undertaken increased exponentially, especially those regarding Ca^{2+} signalling. The *in-vivo* measurement of $[\text{Ca}^{2+}]$ has been possible thanks to the use of ratiometric probes, providing insights into the intricate spatial and temporal signalling system.

The visualization of ratiometric sensors in complex plant tissues and organs such as the root is feasible with standard microscopy modalities. Wide-field epifluorescence microscopy has been successfully used to visualize Ca^{2+} dynamics, but with the main limitation of absent sectioning capability [46, 53]. Moreover, when performing root hair studies, the signal from the thick primary root saturates the detector, covering the small hair signal. Single cell resolution in the root can be reached through confocal microscopy, the routine technique to visualize fluorescent probes, and multi-photon microscopy, both allowing the visualization of calcium response to both biotic and abiotic stimuli [75, 91]. However, the main issue remains the high photodamage and the confinement of the analysis to small volumes [41, 57].

Chapter 3. Calcium Dynamics in Plant Root

Moreover, during imaging experiments with standard microscopy procedures, the plants are usually placed horizontally on a slide, with some channels and pumps delivering stimuli or changing the medium. Although widely used, such preparation can induce stress conditions or physiological reactions and the horizontal position is even more problematic for an organ such as the root, whose growth is biased by gravity [7] and whose hairs develop in a 3D-like manner. Light sheet fluorescence microscopy tries to overcome the limitation of standard fluorescence microscopy techniques by combining the advantages of different approaches to get images at high speed and with high dynamic range of calcium signals with single cell resolution over a wide field of view. Because of the use of pixelated detectors instead of photodiodes, it is easier to get multicolour signals for ratiometric imaging on just one detector. LSFM is indeed well suited for fast 3D *in-vivo* imaging of plants with minimal photo-damage to the sample [55, 84]. Thanks to the low dose of light needed to image one plane (and, of course, a volume too) it is possible to perform long-term time-lapse imaging, permitting developmental considerations. A noticeable feature of LSFM for plant biology is its flexibility, which makes it possible to image structures ranging from whole organs to organelles over time ranging from seconds to days. Last but not least, long-term imaging is possible also because, all through the acquisition, the seedlings are placed vertically in conditions similar to those used for their growth, with the shoot in the air and the root floating and growing in their medium. The near physiological imaging conditions represent a considerable benefit, reducing significantly the invasiveness of the mounting procedure and of the whole acquisition.

3.1.3 Plant description

Arabidopsis thaliana is a small flowering plant with translucent roots (Figure 3.1(C)) native to Europe, Asia and northern Africa. It is considered an infesting weed and can be found by roadsides and in every garden (Figure 3.1(A)). From the early twentieth century, *Arabidopsis* plants started to be used for research purpose, with the first mutants being produced starting from 1948, until in 1998 it has been designated as the model organism for plant biology and especially for genetic research. The reasons of its success are numerous: thanks to its small size, to the short development cycle of the beans (six weeks), the production of about 40000 seeds per plant, its resistance and its ability to self-fertilize, *Arabidopsis* can be easily grown in huge number even in small laboratories (Figure 3.1(B) and (C)). Its genome is one of the smallest in the

3.2. Material and methods

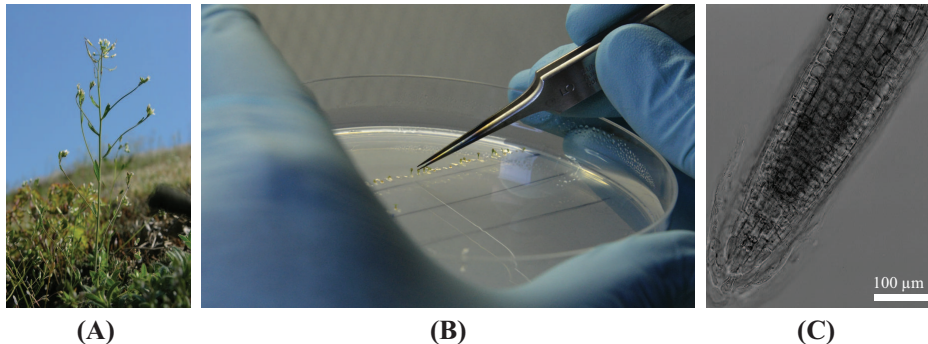


Figure 3.1: *Arabidopsis thaliana* plants. *Arabidopsis* is a small flowering plant considered an infesting weed (A). They can be easily grown in laboratory, where the seeds are usually placed in petri dishes filled with plant agar (B). Their roots appear translucent at the microscope (C). Copyright for (A): <http://creativecommons.org/licenses/by-nc/3.0/>.

plant kingdom, and the lack of economic interest on this species facilitates the spreading of information in the scientific community. Indeed, in 2000 *Arabidopsis* became the first plant with a completely sequenced genome [5]. By focusing on this single system, the scientific plant biology community has made dramatic advances. Moreover, discoveries in *Arabidopsis* have been readily translated to other plant species and even to crops, thanks to the close evolutionary relationship among all flowering plants, with some disclosures impacting even the animal research.

3.2 Material and methods

3.2.1 Plant preparation

The introduction of genetically encoded Ca^{2+} indicators allowed one to observe intracellular Ca^{2+} dynamics in living plants [4, 45]. In the present work, FRET-based Yellow Cameleon YC3.6 [63], the most popular indicator in plant biology, has been used. This indicator, which is excited with light around 440 nm, requires the detection of both the CFP and cpVenus emission (at 480 nm and 530 nm, respectively). By evaluating the variations of the ratio of the cpVenus emission over the CFP one, it is possible to measure the variation in the $[\text{Ca}^{2+}]$.

Chapter 3. Calcium Dynamics in Plant Root

The sample consisted of 8-14 day-old transgenic *Arabidopsis* seedlings expressing the cytosolic (NES-YC3.6) or nuclear (NLSYC3.6) localized cameleon YC3.6. Den Herder and coworkers previously reported a full description of the generation of these lines and of the targeting strategies [46]. Knockout mutants lacking a glutamate-like receptor were also developed.

All *Arabidopsis thaliana* plants used in this study were of the Columbia-0 ecotype (Col-0). Plants were grown on 16/8 h cycles of light at 22° C and 75% Relative Humidity. Seeds of *Arabidopsis* were surface sterilized by vapor-phase sterilization and plated individually in sterile conditions using a sterile toothpick on half strength Murashige and Skoog medium (MS, Duchefa, Netherlands) supplemented with 0.1% sucrose, 0.05% buffering agent (MES), pH 5.8 and solidified with 0.8% of plant agar (Duchefa, Netherlands) [61]. After stratification at 4°C in the dark for 3 days, seeds were ready to be transferred in the sample holder for imaging measurements. Plates were always kept vertically. All the plants were developed and provided by Alex Costa and coworkers in Università degli Studi di Milano.

3.2.2 Experimental setup

The light sheet setup implemented is a SPIM based on the OpenSPIM project and its schematic is represented in Figure 3.2. The system has been designed to be easy to use even by inexperienced users, for screening routines of large number of samples with the almost no need of realignment. The output of a single mode fiber, coupled to a laser emitting at 442 nm (MDL-III-442, CNI), is collimated and then focalized through a cylindrical lens ($f_{CL} = 50$ mm) in a horizontal plane. A 1X telescope ($f_1 = f_2 = 50$ mm, Thorlabs) conjugates the focal plane of the cylindrical lens to the back focal plane of a 10X water-dipping microscope objective (UMPLFLN 10XW, Olympus), which provides a vertical light-sheet in its front focal plane. The use of an objective after the cylindrical lens helps reducing the light sheet dimension without the use of apertures, minimizing the possible beam aberrations. The height of the light sheet is matched with the acquired field of view, but the illuminated area in principle can still be further reduced by a slit in the centre of the telescope. As a result, a single plane of the sample is illuminated. The detection stage is composed by a 20X water-dipping microscope objective (UMPLFLN 20XW, Olympus) held orthogonally to the excitation axis. Since the calcium indicator is FRET-based, a two-wavelength detection is needed. Thanks to the vertical geometry of plant roots, it is practical to record two images with different spectral content on the

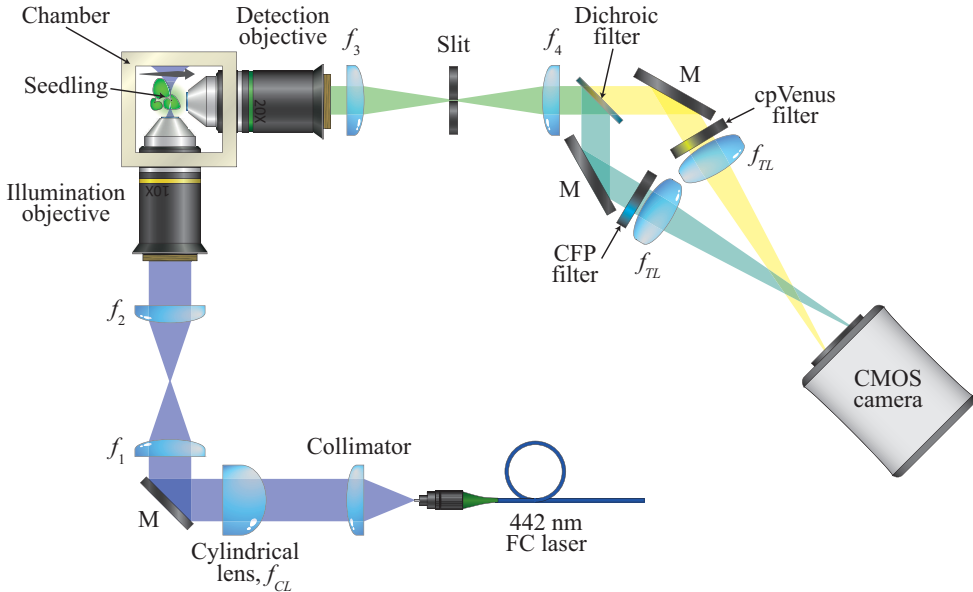


Figure 3.2: *SPIM setup: a cylindrical lens ($f_{CL} = 50$ mm) creates the light sheet from a single-mode fiber-coupled (FC) laser emitting at 442 nm, and projects it on the back-focal plane of the 10X water-dipping illumination objective through a 1X telescope ($f_1 = f_2 = 50$ mm). The seedling is held in a chamber filled with its physiological solution and can be translate through a translation stage. The 20X water-dipping detection objective is held at 90° and sends the fluorescence signal to a relay system ($f_3 = f_4 = 100$ mm) and a vertical slit to reduce the horizontal dimension of the image. A Dichroic filter at 505 nm separates the image into the CFP and cpVenus channels, which are filtered by their specific emission filters. A tube lens ($f_{TL} = 180$) creates the two images on the same CMOS sensor. M =mirror.*

same pixelated detector by splitting the detection path in two spectral channels.

The immersion objective is followed by a 1X relay lens system ($f_3 = f_4 = 100$ mm, Thorlabs), whose intermediate image plane is exploited to position a vertical slit. This slit horizontal dimension is $400 \mu\text{m}$, exactly half of the field of view. A dichroic filter at 505 nm (DMLP505, Thorlabs) creates the two-colour replicas of the field, which are then sent through two band-pass filters (MF479-40 and MF535-22 emission filters, Thorlabs) and a tube lens (U-TLU-1-2, Olympus) by two broadband mirrors (BBSQ1-E02, Thorlabs). The tube lens creates the images with the CFP and the cpVenus signals on the two sides

Chapter 3. Calcium Dynamics in Plant Root

of the CMOS sensor (Neo 5.5 sCMOS, ANDOR). The laser power was set to $20 \mu\text{W}$, which proved not to give any relevant photobleaching during continuous illumination for over half an hour experiment. To minimize the light dose to the sample, an automatic shutter switches on the laser beam only when the camera is in acquisition mode. A white LED illuminator in transmitted light configuration is used for the sample alignment. The sample is held vertically in a custom made 3D-printed chamber, filled with the growing medium of the plants. The sample is then scanned along the detection axis to acquire 3D stacks of images through a motorized translation stage (PI M-405.CG). The camera acquisition, sample translation stage and shutter are synchronized via a home-made LabVIEW software. This software permits to look at the two channels and at their ratio in real time. It also allows to record 3D stacks of images and save all the single planes and/or directly their Maximum Intensity Projection (MIP), taking advantage of the camera internal memory. It is worth mentioning that while recording a fast 3D stack, the camera is acquiring while the sample is smoothly moving, without stopping the translation stage for every frame recording. This stratagem permits to avoid the settling time of the translation stage in a stepping regime, hence allows to fast record 3D dataset. Of course, if the translation step is bigger than light sheet thickness, the obtained signal is integrated over a volume that can be thicker than the light sheet. This apparatus will be referred to as SPIM-FRET setup.

3.2.3 Seedling mounting

During imaging experiments, most microscopes oblige the operator to mount the plant horizontally on a glass slide (Figure 3.3(A)), but this procedure can induce stress conditions or physiological reactions, like hormones redistribution as a consequence of tropism. On the contrary, in the SPIM-FRET setup the sample can be held from the top of the imaging chamber in vertical position, with the roots immersed in its growing medium and the shoot in the air. The mounting procedure had to be completely reinvented.

As soon as the plants are ready to be imaged, they are checked for fluorescence signal and the good ones are quickly moved to home-made holders. These latter, shown in Figure 3.3(B), are conical plastic holders, typically a 10 mL pipette tips, coupled with properly cleaned FEP tubes and filled with another porous gel, Phytigel, supplemented with MS. The top of the FEP tubes, however, is still filled with agarose 1%. The plants are positioned over the top of the tubes, using sterilized pliers being careful to not clamp them, so that the

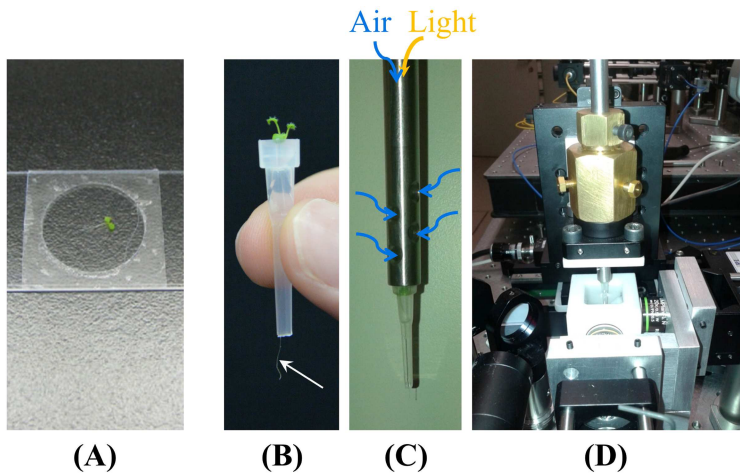


Figure 3.3: *Seedling mounting: usually seedlings are positioned horizontally on a glass slide (A), which can induce stress to the plant. Thanks to the SPIM geometry plants can be mounted vertically. Seedlings are placed on the top of pipette tips coupled with FEP tubes and filled with Phytigel (B); they grow inside the tube until they come out (white arrow). The pipette tip are attached to a hollow column, with lateral holes for the air and with a fiber inside the internal cavity to shine light when the plant is not being imaged (C). The hollow column is indeed inserted in the imaging chamber (D).*

plant roots can grow inside the tube itself. All the plant holders are placed in a pipette tip box, which can be 3D printed, with a transparent cover, filled with sterile half strength MS solution for hydroponic culture, sealed to avoid contamination and placed in a growth chamber under 16/8 hours cycles of white light at 22°C. The hydroponic system permits to the seedling roots to follow the gravitropism during their growth. Once the root reaches the desired length, the specimen is transferred to the imaging chamber of the SPIM-FRET setup, which is filled with the desired plant solution (Figure 3.3(D)). The tubes are held inside the chamber by attaching the pipette tip part to a hollow column, with lateral holes for the air to arrive to the shoot and with a fiber inside the internal cavity to shine light when the plant is not being imaged (Figure 3.3(C)). This routine prevents damages or major stress to the roots, while keeping the plant in a vertical position.

Chapter 3. Calcium Dynamics in Plant Root

3.2.4 Plant root treatments

A series of experiments with Arabidopsis seedlings expressing nuclear or cytosolic localized cameleon YC3.6 were performed in order to attest the manifestation and spatiotemporal organization of Ca^{2+} fingerprints in response to the application of different external stimuli.

During the whole experiments, the Arabidopsis seedling were held in the imaging chamber filled with 10 mM MES, 5 mM KCl, 10 mM CaCl_2 , pH 5.8 adjusted with TRIS-BASE solution. The stimuli consist in adding 120 μL of (100X) glutamate (L-Glu, final concentration 1 mM) or of external ATP (eATP, final concentration 0.1 mM) to one corner of the imaging chamber. The stock ATP solution was diluted in a TRIS buffer (pH 5.8) in order to prevent any pH change of the imaging solution.

3.3 Results and discussion

3.3.1 Image quality

The first prominent characteristic of the implemented setup is the wide field of view, which allows one to observe an area of around $800 \times 450 \mu\text{m}^2$ for each of the two simultaneously recorded channels. This area is more than enough for the imaging of plant roots, which have usually a cylindrical symmetry with a diameter of around $100 \mu\text{m}$, although secondary roots and root hairs can protruded even for millimeters at the adult stage. The sensor dimension of the used CMOS camera is $16.6 \times 14.0 \text{ mm}^2$ with 2560×2160 pixels in total. This leads to a pixel dimension of $6.48 \mu\text{m}$, corresponding to $0.367 \mu\text{m}$ on the sample.

In terms of sectioning capability, the light sheet beam waist can be calculated theoretically by gaussian optics. The illumination objective has a magnification of 10X and should be used with a tube lens with $f = 180 \text{ mm}$. We can indeed approximate this objective with a thin lens with a focal lens of 18 mm. After the collimation of the single mode fiber output, the beam has a waist of about 1.25 mm. Taking into account that in the back focal plane of the objective there is the projection of the focus of a cylindrical lens, i.e. a line, the objective will create a light sheet by magnifying the beam 0.36 times in one direction to $1/e^2$ height of $900 \mu\text{m}$ but leaving it collimated, while focalizing it in the orthogonal direction to a theoretical beam waist of $w_f = \lambda f / \pi w_i = 2.02 \mu\text{m}$. The system is not completely aberration-free, therefore to properly characterize it, fluorescent beads of a diameter of $0.1 \mu\text{m}$ (Molecular Probes) were suspended in agarose 1% in low concentration (1:4000). Given the small diameter of the

3.3. Results and discussion

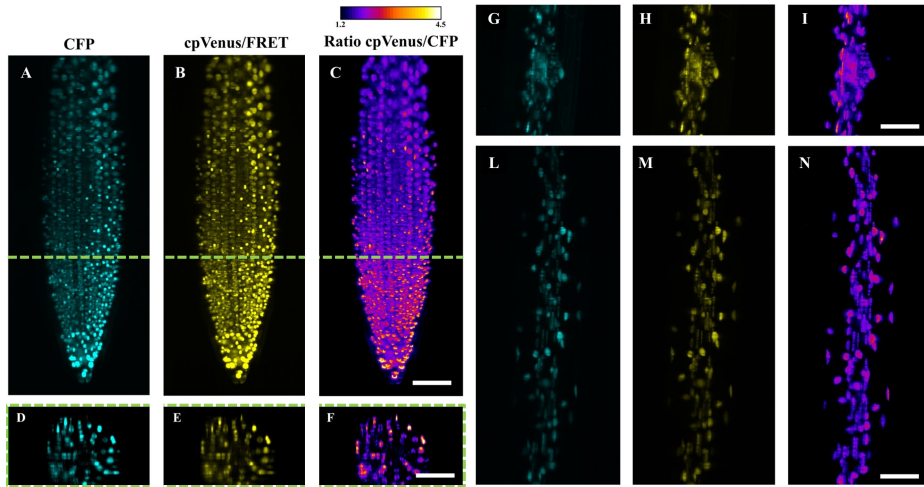


Figure 3.4: Image quality of the SPIM-FRET setup for plant imaging. Maximum intensity projections of the stacks obtained for CFP (A, D, G, L), cpVenus/FRET (B, E, H, M) and Ratio between the two channels (C, F, I, N) in different regions of the *Arabidopsis thaliana* root (from (A) to (N): primary root tip, trasverse section from the green dashed line, lateral root primordium and root mature zone) expressing the nuclear localized cameleon. Scale bars 50 μm .

beads, these can be considered as point sources. By moving this calibration sample through the light sheet and by fitting the fluorescence signal at every position with a Gaussian, it is possible to extract the profile of the light sheet and infer its thickness. The light sheet waist was found to be 2.6 μm thick, meaning that the Rayleigh range is 48 μm , which is around half the diameter of a sample plant root.

As an example of the capability of the system to be actually able to record disparate root areas, three different regions of the seedling root (primary root tip, lateral root primordium and root mature zone) are shown in (Figure 3.4, where the plants were expressing the nuclear targeted cameleon. Single nuclei can be distinguished both in the thicker mature zone and in developing organs such as the lateral root primordium (Figure 3.4(G,H,I)), where there is a high cell concentration. It is already possible to notice that some nuclei are more blurred: this is because what is shown is a MIP and the nuclei that are sharper are those closer to the detection objective. However, despite the presence of non-negligible scattering at the excitation wavelength, as can be clearly seen

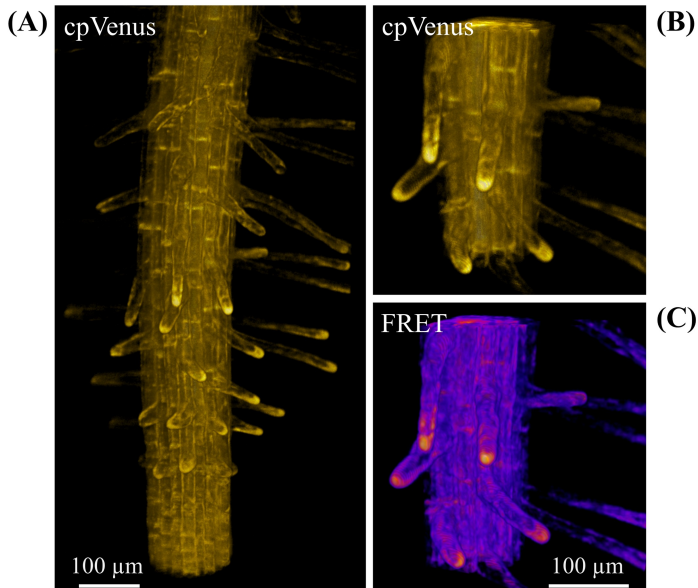


Figure 3.5: *Three-dimensional reconstructions of Arabidopsis root expressing the cytosolic targeted cameleon. Slices were acquired with a step of 1.5 μm. The single channel reconstruction (A) shows the root hairs three-dimensionally organized around the mature and elongation zone. Root hairs look straight, smooth, and usually follow gravitropism, as also shown from the detail in (B). The same consideration can be done by looking at the FRET reconstruction (C).*

from the transverse sections in Figure 3.4(D, E, F), the recorded images show sub cellular details all over a large tissue.

Figure 3.5 shows 3D reconstructions of the mature and elongation zones with root hairs of a plant expressing the cytosolic targeted cameleon. The fast acquisition and wide field of view of the microscope allowed us to image large tissue volumes: multiple root hairs can be monitored in a single experiment, producing statistically relevant data. Notably, even in the FRET reconstruction in Figure 3.5(C), it is possible to clearly distinguish cells and perform morphological inspections.

3.3.2 Ca^{2+} dynamics observation through SPIM-FRET

The fluorescence intensity was evaluated over different types of Regions Of Interests (ROIs), corresponding to large root tip areas, single cells or nuclei. No registration of the two FRET channels was needed. Background subtraction was performed in each channel before FRET ratio calculation. For the evaluation of the temporal evolution of the $[\text{Ca}^{2+}]$, the FRET ratio ΔR was normalized to the minimum value, i.e. the initial resting state value (R_0), multiplied for the K_d of the cameleon indicator and plotted versus time ($\frac{\Delta R}{R_0}$). To convert the observed FRET values to calcium concentrations, a calibration of the probe is required. The maximum FRET ratio was indeed measured under saturating Ca^{2+} conditions at the end of experiments by treating the plant with high concentration NaCl.

The first analyses were done on a single plane in the middle of the primary root tip of Arabidopsis seedlings (50 μm in depth) expressing the nuclear localized cameleon. A single plane was illuminated and imaged continuously for 60-300 s with an exposure time of 50-300 ms. This latter was decided upon photobleaching and signal to noise considerations, with the aim to get a good temporal resolution. The laser power was set to 20 μW , value set in order to get no observable photobleaching over 10 minutes of recording in experimental conditions.

In Figure 3.6 is presented the nuclear FRET response after treatment with 1 mM L-Glu, a stimulus known to induce $[\text{Ca}^{2+}]$ rises in plant cells [74]. A change in the FRET ratio in the cells of the root tip reveals that the treatment actually induces a detectable Ca^{2+} transient. Actually, the fact that the plant responds could have been seen even with a standard epifluorescence microscope. On the other hand, on a closer inspection, the use of SPIM reveals that the increase in FRET signal appears first in the nuclei of the lateral root cap cells, and only afterwards the nuclei located on the upper part of the root light up. This means that the stimulus is primarily perceived by the cells of the lateral root cap and then by those located in the transition and elongation zones. Thanks to the single cell resolution over the whole root tip area it is in fact possible to observe the individual response of distinct cells. Figure 3.6 also shows the time course (ratio versus time) of the highlighted 6 nuclei, showing differences both in amplitudes and temporal delay (lower panel, left). Averaging the response of the selected nuclei (lower panel, centre) or of the entire plane (lower panel, right), a longer response is obtained, resembling what would have been measured with a lower spatial resolution and sectioning capability [19].

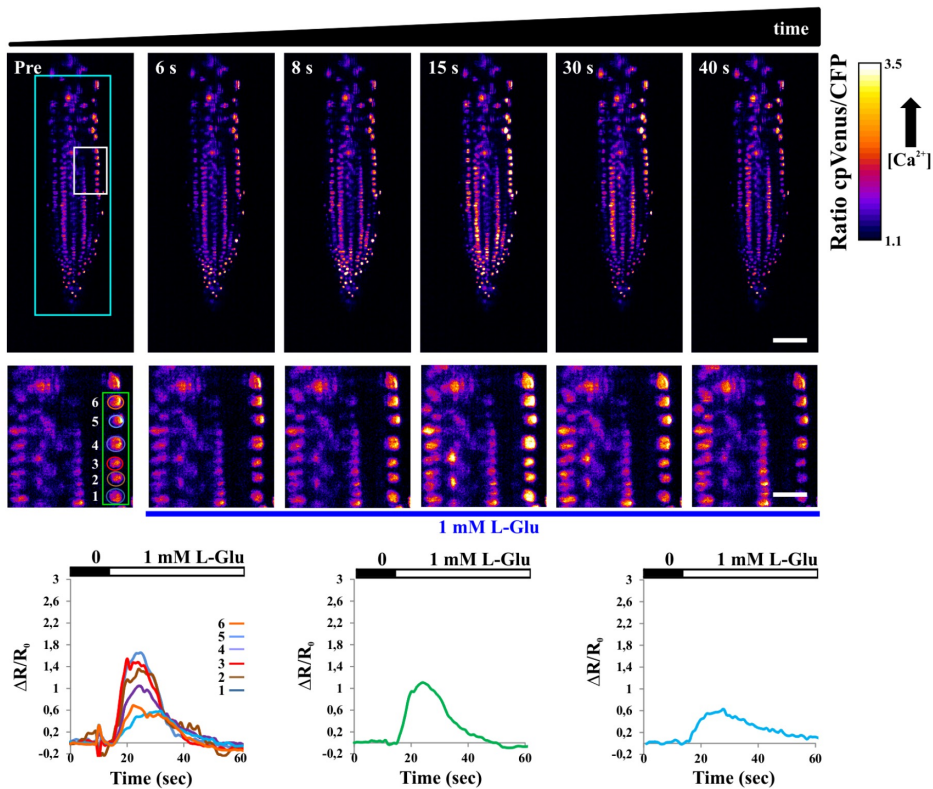


Figure 3.6: Single-plane images of the FRET ratio in root tip of *Arabidopsis* seedlings expressing the nuclear-localized cameleon. The acquisition was done at 10 Hz during the application of 1 mM L-Glu stimulus. First row: FRET ratio images at different time points from the sensing (Pre) of the L-Glu stimulus. Second row: close up (white rectangle in the top-left image) of the FRET ratios including 6 selected nuclei (green rectangle). Third row: temporal evolution of the FRET ratio in the 6 distinct nuclei (left), average on the 6 nuclei (centre), average on the entire plane (right). Scale bars are 50 μm and 10 μm for low and high magnifications, respectively. Adapted from Costa and coworkers [16].

A second treatment consisting in 0.1 mM eATP [46] was applied to the same plant after rest state recovery and is reported in Figure 3.7. Again, it is the lateral root cap that senses the stimulus first, while the other part of the root shows a delay in the response. It is worth noting that the acquired plane is exactly the same for the two experiments, which means that the SPIM-FRET system is robust for plant analysis. This consents to directly compare how a specific nu-

3.3. Results and discussion

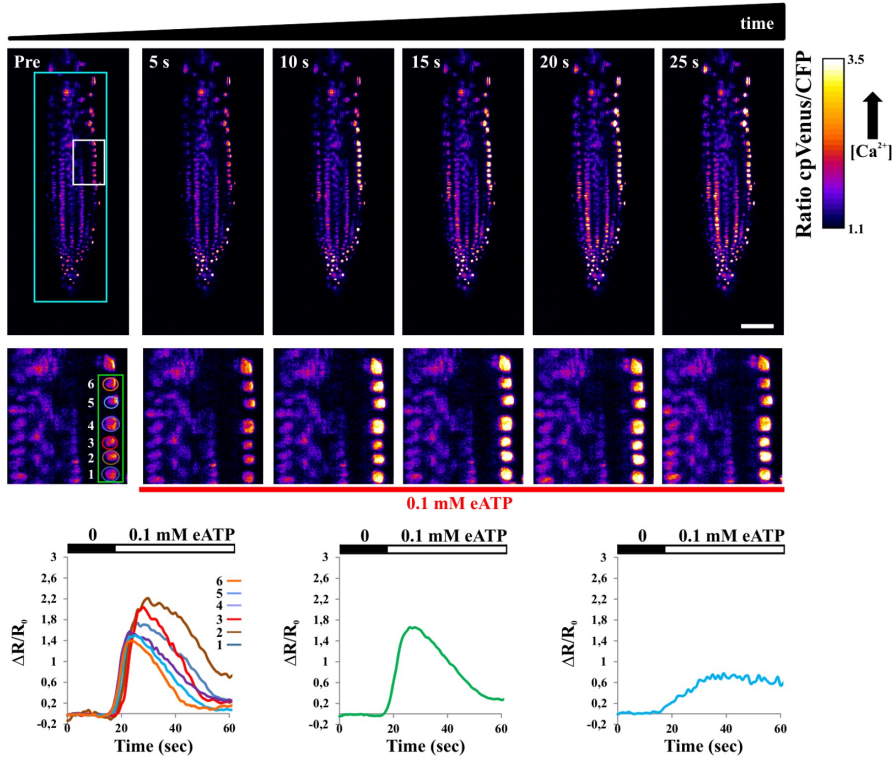


Figure 3.7: Single-plane images of the FRET ratio in root tip of *Arabidopsis* seedlings expressing the nuclear-localized cameleon. The acquisition was done at 10 Hz during the application of 0.1 mM eATP stimulus. First row: FRET ratio images at different time points from the sensing (Pre) of the L-Glu stimulus. Second row: close up (white rectangle in the top-left image) of the FRET ratios including 6 selected nuclei (green rectangle). Third row: temporal evolution of the FRET ratio in the 6 distinct nuclei (left), average on the 6 nuclei (centre), average on the entire plane (right). Scale bars are 50 μm and 10 μm for low and high magnifications, respectively. Adapted from Costa and coworkers [16].

cleus reacts to different stimuli. In the specific case of the already mentioned 6 nuclei, the Ca^{2+} elevation in response to L-Glu shows single and narrow peaks, while the one induced by eATP is more sustained; this observation points out the existence of different mechanisms responsible for the Ca^{2+} transients generation that can be triggered by different stimulations. Each experiment has been repeated $n = 6$ times and the statistical analysis of the FRET variations is shown in Figure 3.8, which highlights that after 40 s from the stimulus, the re-

Chapter 3. Calcium Dynamics in Plant Root

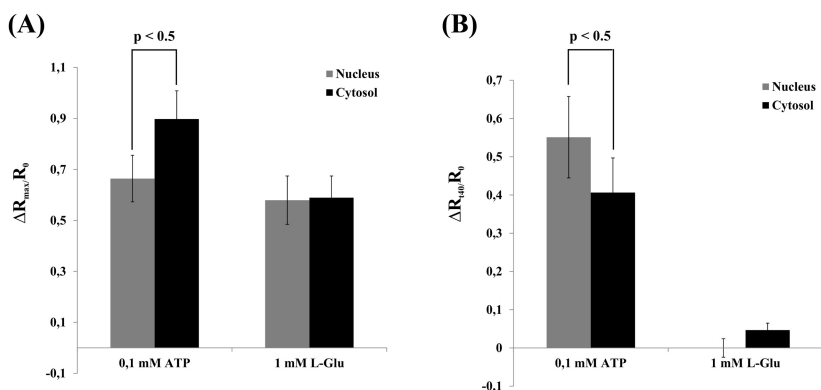


Figure 3.8: Statistical analysis of the response amplitude and duration, in root tip of *Arabidopsis* seedlings expressing the nuclear or cytosolic localized cameleon, for 0.1 mM eATP and 1 mM L-Glu stimuli. (A) Mean value of the FRET ratio changes measured on the peak of the response ($\Delta R_{max}/R_0$). (B) Mean value of the FRET ratio changes measured 40 s after the stimulus ($\Delta R_{40}/R_0$). The eATP response is still active at long times while the L-Glu response is depleted. Values are means \pm SE ($n = 6$). p -values were calculated by Student's t -test. Reproduced from Costa and coworkers [16].

sponse induced by the eATP is still active while the L-Glu response is depleted. Control experiments were also performed by applying the solution without any Ca^{2+} mobilizing agent and the FRET changes were below the camera noise.

However, most of the changes in the $[\text{Ca}^{2+}]$ take place in the cytosol. The experiments were indeed repeated in seedlings expressing the cytosolic-targeted cameleon [46]. Figure 3.9 shows the response of the same plane of the same root tip to L-Glu and eATP. In accordance to what observed with nuclei, lateral root cap cells are the first to perceive these stimuli, followed by the cells in the central part of the root as well as by those of the transition and elongation zone. Also, by comparing both the average and single cell responses, it can be noted again that, although the Ca^{2+} peaks values are similar, the shapes of the dynamics are different, with the one induced by eATP being more sustained; secondary peaks also appear at longer times, as shown later. Indeed, thanks to the fast acquisition rate (typically 3-20 Hz for a single plane depending on the fluorescence of the sample), it is possible to visualize a phenomenon still not clear in plants, the so-called “signal percolation”. What can be inferred from the data is in fact that there is not a diffusion of the stimulus inside the

3.3. Results and discussion

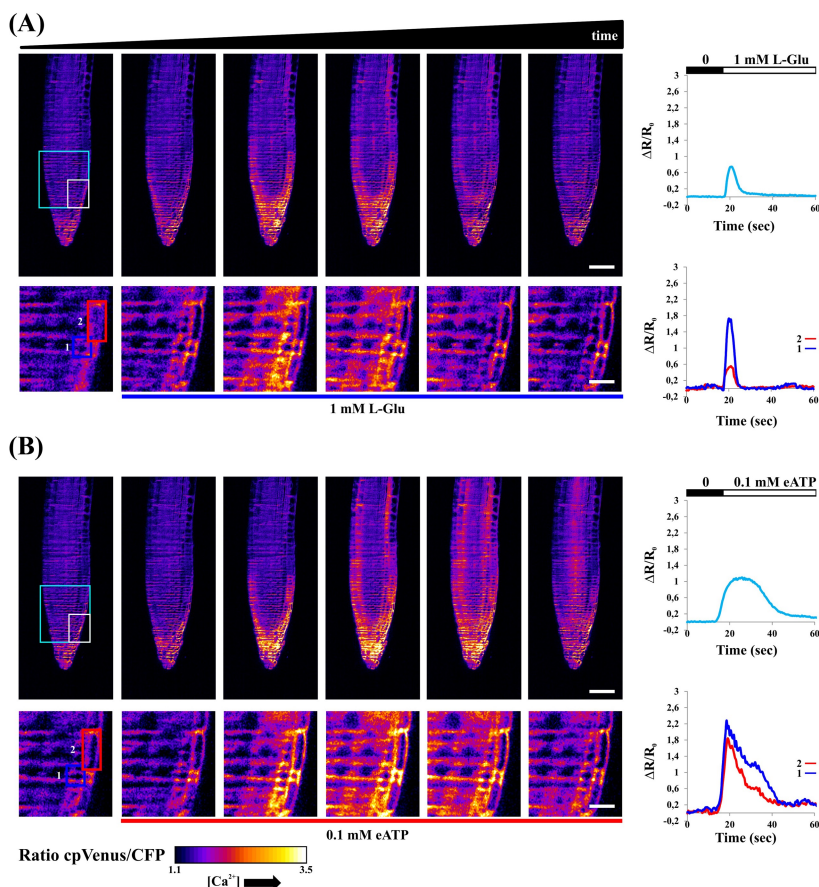


Figure 3.9: Single-plane images of the FRET ratio in root tip of *Arabidopsis* seedlings expressing the cytosolic localized cameleon, recorded at 10 Hz during the application of 1 mM L-Glu (A) and 0.1 mM eATP (B) stimuli. (A) Upper images: FRET ratio images at different time points from the sensing (Pre) of the L-Glu stimulus. Lower images: close up (white rectangle in the top-left image) of the same selected FRET ratios. Upper graph: temporal evolution of the FRET ratio for the entire region highlighted by the cyan rectangle. Bottom graph: temporal evolution of the FRET ratios for two selected cells (blue and red rectangles in the lower images). (B) Analogous for the eATP stimulus. Note that the sample and imaged plane are the same for both the experiments. Scale bars are 50 μm and 9 μm for low and high magnifications, respectively. Reproduced from Costa and coworkers [16].

plant, because the response takes place in specific cells although the stimulus

Chapter 3. Calcium Dynamics in Plant Root

reaches the whole root non-specifically and the initiation of the following cells looks like a propagation of activation with a wave-like pattern. The presence of “calcium waves” requires cell-to-cell communication so that the “late” cells indirectly sense the stimulus and build up the “Ca²⁺ signatures” [72].

An even more interesting analysis to run is the comparison of two specific lateral root cap cells (blue and red rectangles curves in Figure 3.9). The FRET signals induced by L-Glu are very different in amplitude for the two cells, while the eATP stimulated responses are similar. These data indicate that being able to look at single cells gives richer information about the Ca²⁺ dynamics, since the average response does not necessarily reflect the behaviour of a single cell, fact that is also in agreement with previous reports [19, 72]. In particular, they suggest that the two selected cells present different proteins expressed in the plasma membrane. This consideration proves that the cell-to-cell communication is also stimulus dependent, since for L-Glu and eATP we have a different fingerprints.

Three-dimensional imaging was also performed for both seedlings expressing nuclear and cytosolic target cameleon. In this case, the main focus is to understand if there the activation is not homogeneous on the different planes. Adjacent planes (typically 10-20) were acquired during the stimulation with a step of 5 to 10 μm depending on the root tilt, leading to a volume rate of recording of 0.2-2 Hz. Every 2.5-6 s the recording of the entire stack was repeated, shuttering the illumination between acquisitions. Figure 3.10 and Figure 3.11 show the FRET ratio images at different times and depths (only a subset of the acquired planes is presented) when eATP is applied. It can be observed that the entire organ responds, but every plane (and of course, every cell) has its own specificity in terms of amplitude and course (see right hand side of Figure 3.10 and Figure 3.11). Also, differences between cytosolic and nuclear Ca²⁺ dynamics can be observed, with the cytosolic Ca²⁺ presenting several oscillations and the nuclear Ca²⁺ having less resolved peaks. By creating 3D reconstructions of the acquired stack, it is feasible to look at the 4D evolution (temporal and spatial) of the systemic root tip response, with fine in-depth details of the nuclei and cytosol. This is something not possible to obtain through standard wide-field microscopy.

Even though understanding the mechanisms underlying the observed differences in terms of response to the two stimuli and in terms of nuclear and cytosolic Ca²⁺ dynamics is beyond the aim of this thesis, it has been proved that the use of a SPIM-FRET setup offers a novel and adequate approach for Ca²⁺ imaging in plants. The spatial and temporal resolution allow to perform single

3.3. Results and discussion

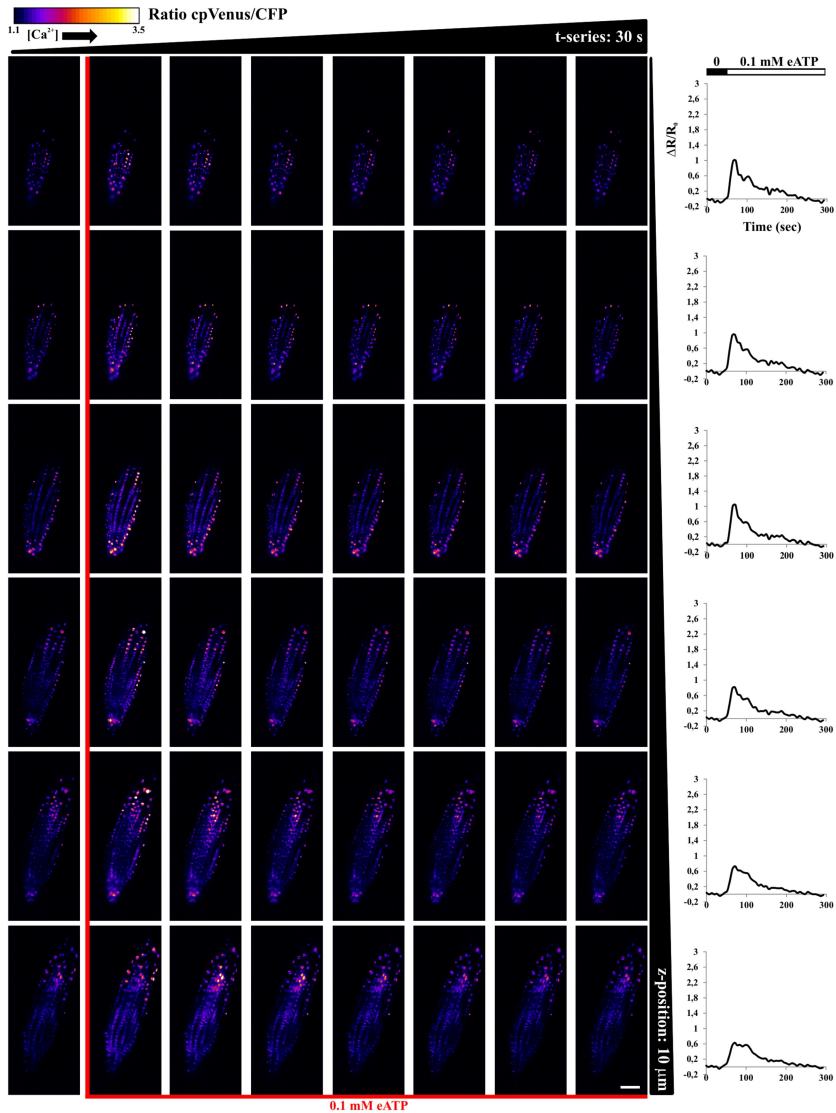


Figure 3.10: FRET ratio imaged in space and time, with 10 μm steps (columns) and every 30 s (rows), in root tip of *Arabidopsis* seedlings expressing the cytosolic localized cameleon, in the course of 0.1 mM eATP stimulus. Graphs on the right hand side report temporal evolution of the average FRET ratio for each single selected plane. Scale bar is 50 μm . Reproduced from Costa and coworkers [16].

Chapter 3. Calcium Dynamics in Plant Root

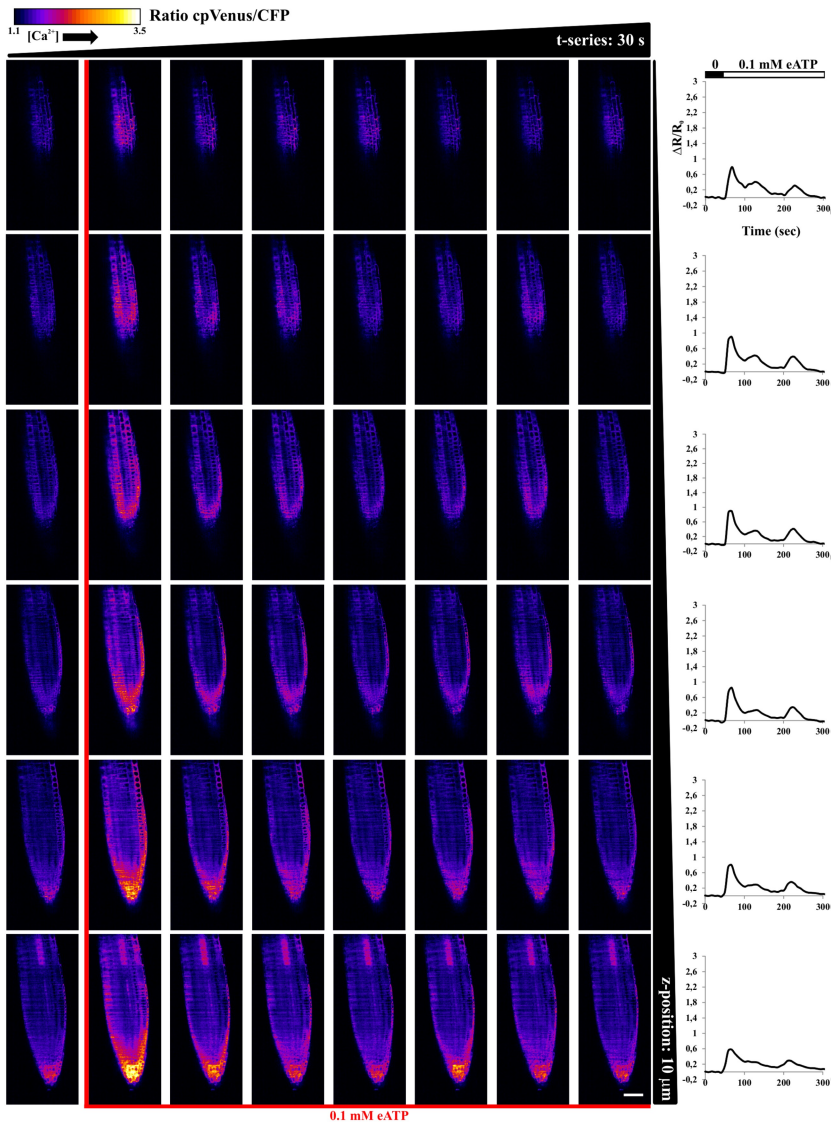


Figure 3.11: FRET ratio imaged in space and time, with 10 μm steps (columns) and every 30 s (rows), in root tip of Arabidopsis seedlings expressing the cytosolic localized cameleon, in the course of 0.1 mM eATP stimulus. Graphs on the right hand side report temporal evolution of the average FRET ratio for each single selected plane. Scale bar is 50 μm . Reproduced from Costa and coworkers [16].

cell analysis over an entire organ with minimum interference of the measurement system to the physiological conditions of the plant.

3.3.3 Calcium oscillations in root hair of *Arabidopsis thaliana*

Light sheet imaging opens indeed the possibility to record the activation of cells that are not directly stimulated, but whose Ca^{2+} elevations are triggered by other cells or by homeostasis regulation. Plants show variations in $[\text{Ca}^{2+}]$ that are not directly linked to an external stimulus, but that are spontaneous. An example of single cells that present spontaneous Ca^{2+} activity are root hairs (RH), that are cells that present a tip growing modality. The healthy growth of RH has been shown to reflect the growing status of the whole plant, since they are responsible for nutrient uptake and for plant-soil interactions.

Previous work done on other apical-growing cells show that the tip growth is Ca^{2+} -dependent. However, RH have the complication of a 3D structure extending all around the root. Because of the similarities in the elongation pattern, the SPIM-FRET setup has been used to perform screening routines of root hairs over a large population of plants, looking at the same time at the growth and at the Ca^{2+} variations. Indeed, the system was used for high throughput root hairs visualization in 3D time lapse experiments. Moreover, since one of the most expressed genes in root hairs belong to the GLR family, comparison between wild type plants and mutants with a specific GLR gene knocked out were done. This study is part of a more complex project about the understanding of the role of specific proteins to improve plant and crops growth.

Screening routines of root hairs growth were performed over a large population of plants: multiple (>20) root hairs were visualized in a single 3D experiment in time lapse, thus producing statistically relevant data about morphological phenotypes and growth of the hairs. We recorded the cpVenus fluorescence from 300 planes every $1 \mu\text{m}$ with a field of view of $800 \times 400 \mu\text{m}^2$. The 3D reconstruction of the root allowed for morphological inspection of the seedlings in order to make considerations on the RH status. It was possible to observe RHs that were mainly healthy, initiating and adapting their shape to obstacles, while rarely impaired, branching and bulging.

To monitor the root hair growth, especially in the long term, a screening routine was developed. An average of 7 RHs per time lapse experiment was imaged. A 3D stack of 15 planes with a spacing of $5 \mu\text{m}$ was acquired every 2.5 s. Since root hairs hardly grow in water, all the images were acquired when the root tip was still in the medium inside the FEP tube, whose refraction index

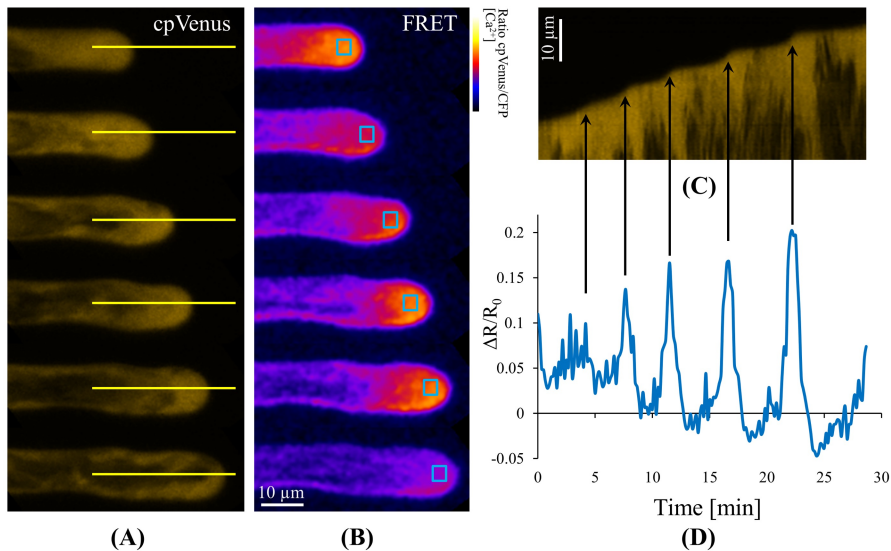


Figure 3.12: *Root hairs growing steps. The maximum intensity projections of a root hair from the cpVenus channel and of the ratio images at different instants of their growth (A and B respectively). From the cpVenus frames, by observing the temporal evolution of the pixel line highlighted in yellow, a kymograph is extracted (C), showing an apical growth at steps. On the images of the ratio, once registered, a ROI can be selected, like the one sketched in blue, and the Ca²⁺ signal can be extracted D. The Ca²⁺ peaks correspond to growing steps.*

($n = 1.344$) is close to the one of water. This tactic allows one not to in any way the three-dimensional growth of the hairs, thing that would not have been possible with standard mounting techniques employing glass slides and horizontal sample mounting. Noticeably, even if the RH were growing, they never went out of focus during the experiments. Figure 3.12(A) shows cpVenus images of the same root hair at different instants of the growth.

A simple graphical method to evaluate RHs elongation relies on a kymograph. This tool gives a space-time representation of the evolution of a line of pixels along a root hair. The same line of pixels taken from every frame is mounted next to the previous one. Figure 3.12(C) shows a kymograph of the cpVenus channel and the ratio, obtained by the observation along time of a pixel line highlighted in Figure 3.12(A). The kymograph shows an elongation of the hair that is not homogeneous over time. This step-like growth is typical of apex-growing systems, like fungal hyphae, pollen tubes, algal rhizoids. In order to

3.3. Results and discussion

quantify the root hair growth, a semi-automatic routine was applied to register the image stacks taken at different time points. To this purpose, we calculated the MIP for every time point. A ROI around every root hair apex was selected by hand on the MIP of the first time point. The registration was performed by maximizing the cross-correlation between each consecutive MIP. The vertical Δx and horizontal Δy displacements were then stored. Finally, by considering the orthogonal projection of the stacks and by computing the MIP at each time point, the registration was performed also in the axial direction and the axial displacement Δz was stored. After the image registration, the instantaneous hair growth was computed through the generalized Pythagorean theorem ($\text{growth}^2 = \Delta x^2 + \Delta y^2 + \Delta z^2$), taking into account the pixel size and the spacing between adjacent planes. The instantaneous rate of growth was estimated by computing the derivative of the growth, and showed an oscillatory behaviour, which can vary during the growing cycle and stop at the end of it. A Ca^{2+} analysis was indeed performed. Growing hairs show a tip-focused spatial Ca^{2+} gradient during growth Figure 3.12(B). The calcium concentration is in fact higher in the first 5 μm from the hair tip toward the primary root and then quickly reduces till reaching resting calcium level. This gradient persists as long as the RH grows, oscillating in time. By the way, emerging root hairs seems not to show the apex gradient from the very first moment. The expression of the cameleon protein as well as the low laser power used during the experiments has no detectable effect on root hair growth or morphology. In fact, even for day-long time lapse measurements, root hairs keep on elongating and new hairs continue to be formed during all the experiments, showing cytoplasmic streaming.

To quantify RH calcium oscillations, 3D measurement of spontaneous calcium activity were performed, with a sampling of 2.5 s. A ROI was indeed selected on registered RH apexes, as highlighted by the blue rectangle in Figure 3.12(B), and the $\frac{\Delta R}{R}$ was extracted. The signal shows variation (Figure 3.12(D) and Figure 3.16(A)) that proved to be quasi-periodic by evaluating the autocorrelation (Figure 3.13(A)) of the different signals and quantifying the oscillatory components through Fourier analysis (Figure 3.17(A)). An average of two main peaks around 0.033 Hz and at 0.007 Hz (one oscillation every 0.5 min and 2.4 min, respectively) were detected.

These elevations in the apical Ca^{2+} has been proposed to be essential in regulating RHs growth, thus they are a good screening subject in order to understand if a plant is growing correctly. Cross-correlation analysis between the calcium oscillations and the growth rates of the RHs was performed. The re-

Chapter 3. Calcium Dynamics in Plant Root

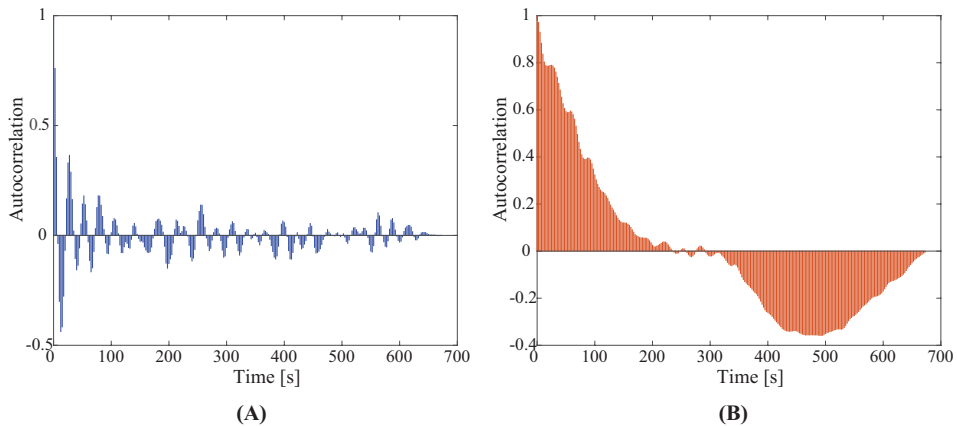


Figure 3.13: Autocorrelation of Ca^{2+} oscillations. Comparison between the autocorrelation of the Ca^{2+} signal from the wild-type (A) and from the mutant (B).

sults highlight how the calcium peaks always follow those of the growth rate, with a temporal shift of 5 s, indicating a strong temporal relationship between the cytoplasmic calcium and the growth itself (Figure 3.14). From similarity with other apex-growing systems, the proposed interpretation is that a positive feedback is present. When a RH emerges, there is no Ca^{2+} gradient in the tip, but as soon as the RH cell stretches thanks to a polar growth, Ca^{2+} channels

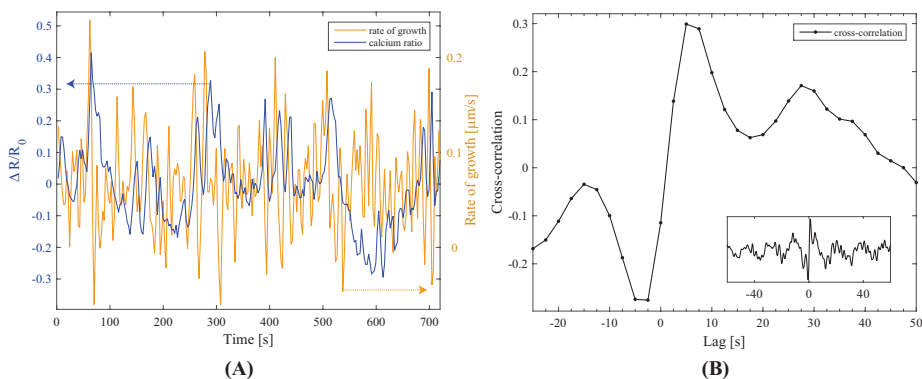


Figure 3.14: Comparison between the rate of growth of root hair and its apical Ca^{2+} oscillations (A). Cross correlation between the rate and the Ca^{2+} variations highlights a lag between the two of 5 s, with the Ca^{2+} oscillation following the step of growth (B).

3.3. Results and discussion

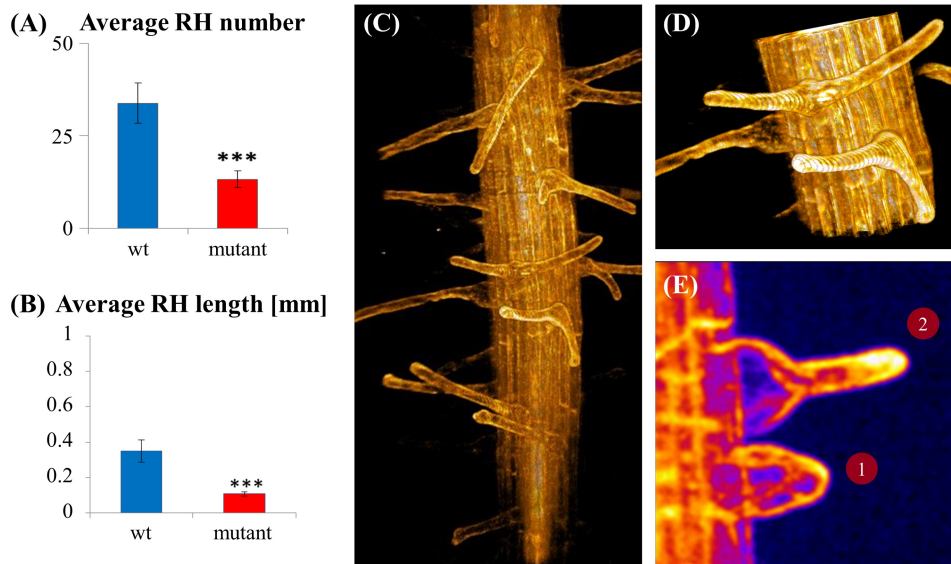


Figure 3.15: *Knock-out mutant shows a clear phenotype in the root hairs. The root hairs are reduced in number (A) and shorter of 1/3 in average (B). The 3D organization around the root looks more disordered, with root hairs sometimes growing without following the gravity (C). Some of them appeared bulgy, branched and with the lack of a defined polarity (D, E). From the Ca^{2+} analysis on MIPs (E), several “young” root hairs show the absence of the Ca^{2+} tip gradient, which leads to the bulgy shape (RH number 1 in (E)). Even when RHs were able to re-establish the polarity (RH number 2 in (E)) they showed altered Ca^{2+} tip oscillations.*

open making the extracellular Ca^{2+} enter into the cytosol. This actually blocks the RH elongation, creating a rest in the growth rate, by favouring membrane thickening and fusion. The high Ca^{2+} is then rapidly removed and a new growing step can start. Hence, Ca^{2+} oscillations are core regulatory of healthy RH growth. This observed mechanism is in perfect agreement with the suggested sequence of events proposed for polarized cell growth explained in more detail in Section 1.5.

Different *Arabidopsis* plant mutants lacking specific genes with high expression in the RH, like the GLRs, were screened following the described routine. The aim is to understand the physiological role of the knocked out genes and in particular if they are active in the Ca^{2+} -dependent tip-growth of RH.

From the morphological inspection, the mutant showed a severe phenotype

Chapter 3. Calcium Dynamics in Plant Root

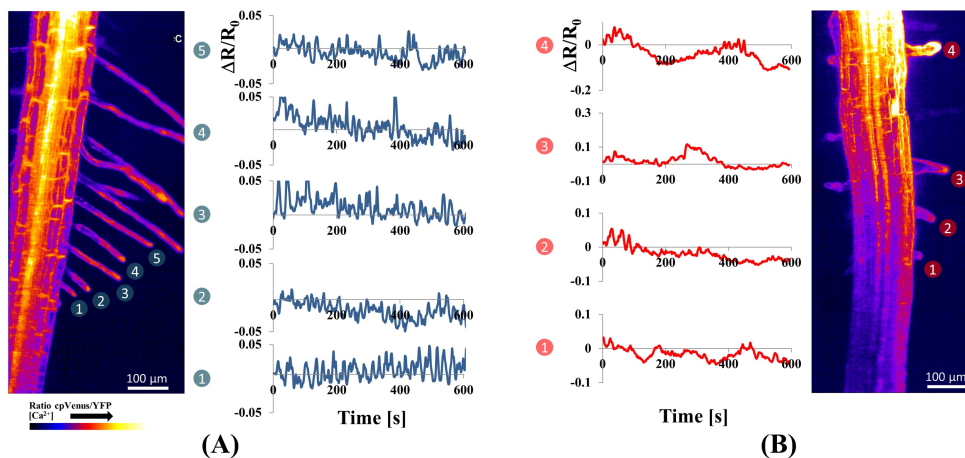


Figure 3.16: Comparison of Ca^{2+} oscillations in root hairs wild-type (A) and mutant seedlings (B). The growth of the seedlings was followed for 10 min by imaging a 3D stack of 15 planes with a spacing of $5 \mu\text{m}$ every 2.5 s. The root hairs of the mutant clearly show altered Ca^{2+} tip oscillations.

alteration in RHs when compared to the wild-type: its RHs resulted reduced in number (Figure 3.15(A)) and shorter of 1/3 in average (Figure 3.15(B)). In the complex, the three dimensional organization around the root looked more disordered, with RHs sometimes growing without following the gravity (Figure 3.15(C)). Some of them appeared bulgy, branched and with the lack of a defined polarity (Figure 3.15(D)(E)). During time lapse experiments they also often broke at the tip, making a huge concentration of Ca^{2+} enter in the intracellular environment and triggering CICR (see Section 1.5) in adjacent cells. All these observations suggest that the chosen GLR mutant is a good candidate for the study of RHs development experiments.

From the Ca^{2+} analysis, in fact, several “young” RHs showed the absence of the Ca^{2+} tip gradient, leading to the bulgy shape (RH number 1 in Figure 3.15(E)). Even when RHs were able to re-establish the polarity (RH number 2 in Figure 3.15(E)) they showed altered Ca^{2+} tip oscillations. Figure 3.16 reports a comparison between the oscillations of the wild type (left side) and the mutant (right side), while Figure 3.13(B) shows the autocorrelation of a Ca^{2+} signal, with clear differences with the one of the wild-type (Figure 3.13(A)): the high frequency oscillations are clearly less evident, while the low frequency oscillation is more important. Finally, breaking RHs show a massively elevated

3.3. Results and discussion

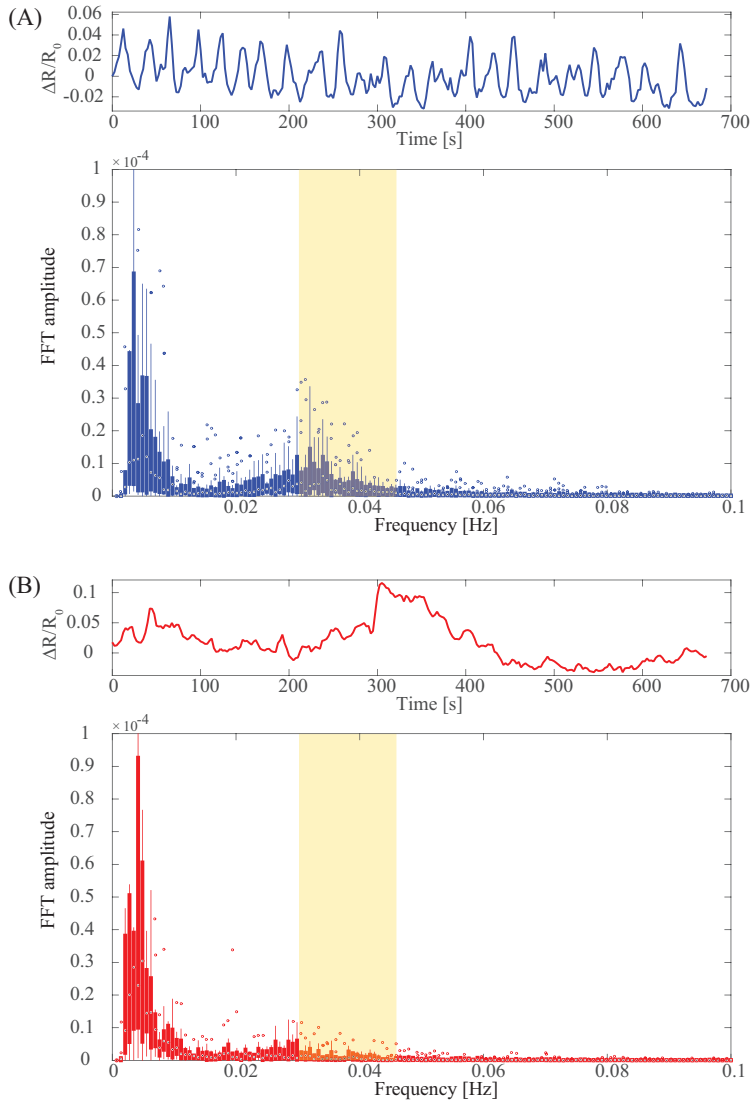


Figure 3.17: Fourier analysis of Ca^{2+} oscillations reveals that the wild-type and the mutant have a statistically different frequency behavior around 0.04 Hz (p -value < 0.05 from Mann-Whitney test). The mutant (B) shows the absence of high oscillation frequencies, highlighted in yellow, with respect to the wild-type (A), as appears clear also from a direct observation of the fluorescence signals (first rows of (A) and (B)).

Chapter 3. Calcium Dynamics in Plant Root

Ca²⁺ concentration just before disrupting.

To quantify the nature of recorded Ca²⁺ oscillations in RH, Fourier analyses were carried out to determine if characteristic frequencies of Ca²⁺ oscillations were present in the wild-type that could be missing in the knocked out mutant. Figure 3.17 shows the plots of the statistical analysis of the Fourier transform of a population of 20 samples. A Mann-Whitney test upon the wild-type and the mutant populations revealed that there is a statistically different frequency content in the mutant spectrum (p -value<0.05), specifically around 0.04 Hz, with the mutant showing an almost completely absence of these high frequencies.

At the moment, solely a correlation has been established between the absence of these high frequencies Ca²⁺ tip oscillations and the defective growth of the knocked out mutant. Nevertheless, the altered Ca²⁺ dynamics strongly suggests a direct link between the lack of the specific gene that was knocked out and the observed RH phenotype, leading to hypothesize that the knocked out gene can actively participate in the proper regulation of Ca²⁺ fluxes. However, a direct evidence in the formation of a Ca²⁺-permeable channel is still missing. In the analysis performed, it has been possible to draw considerations on the root hair status by morphological inspection of a large part of the root with single cell resolution, with the root hair in their physiological condition. It has been possible to identify a direct relationship between healthy RH growth and spontaneous Ca²⁺ oscillation in the RH apex. The Ca²⁺ oscillation lags the growth steps of 5 s, in line with other tip-growing systems. By comparison, it has been also possible to identify a gene belonging to the GLR family whose lack in the expression leads to growth issues. This gene can be said to be involved in the proper regulation of calcium in RHs.

3.4 Conclusions

In the plant biology framework, light sheet has shown many advantages with respect to other standard techniques, spanning from the general advantages of LSM to the sample mounting, which allows looking at plants really in 3D in the most physiological conditions possible. The technique has been validated by proving the possibility to perform single cell analysis over a wide organ of the plant during the application of different stimuli. This led to the observation of “calcium waves” and cell-to-cell communication, as well as the identification of cells with different receptor expressions. The capability of looking at

3.4. Conclusions

spontaneous cellular activation allowed us to easily perform root hair measurements of spontaneous oscillation over a wide number of hairs per root. Calcium oscillations at the RH apex were characterized and it was feasible to conclude that Ca^{2+} increases right after a polarized growth. Both wild-type and mutant with a GLR gene knocked out were screened, the mutant showing a deregulation in the calcium oscillation. Hence, the knocked out gene was supposed to be linked to Ca^{2+} permeable channels in the root tip cells, although further studies must be done. Specific frequencies in the Fourier spectrum of Ca^{2+} oscillations characteristic of a healthy growth were identified and will be used on large scale studies of Arabidopsis knock out mutants with the aim of identifying the functional role of specific genes.

It must be noted that the system was made as simple as possible to be easily used by biologists on their own with little adjustment. However, improvements of the setup could involve the use of a dual-view and/or a multidirectional SPIM, as well as the use of structured light to reduce the blur in the images.

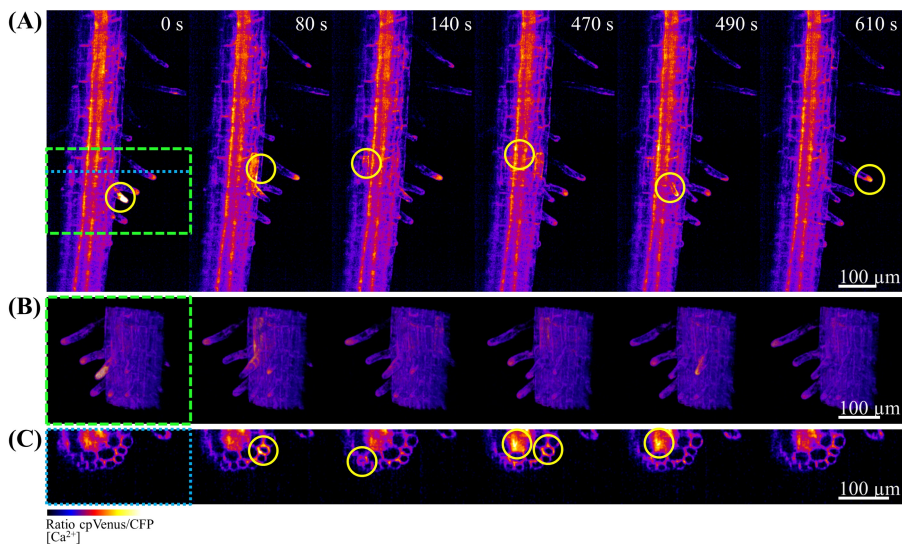


Figure 3.18: *Three-dimensional CICR. Calcium oscillations originating from the root hairs were observed and their propagation was visualized three-dimensionally in time lapse. The maximum intensity projection of the root (A), a 3D reconstruction of a detail highlighted by the green rectangle (B) and a transverse section (C) indicated by the blue dotted line are depicted. Yellow circles mark the cells where the Ca^{2+} is transmitted.*

Chapter 3. Calcium Dynamics in Plant Root

Currently, the research is focusing on the 3D analysis of calcium bursts originating from single cells (CICR). These localized Ca^{2+} increases seem to propagate inside the root through specific cells, as shown in (Figure 3.18). The cellular connections have been visualized three-dimensionally in time-lapse experiments and a proper pipeline for their mapping is presently being developed.

CHAPTER 4

Calcium Imaging in the Brain of Zebrafish Larva

THE NERVOUS SYSTEM IS A COMPLEX STRUCTURE, with a variety of levels of organization: from synapse to behaviour, passing through neural circuits. To shed light over the neuronal network, both evoked and spontaneous activity must be studied. In the following chapter, a fluorescence light sheet microscope based on a digital laser scanner was used to record the activity from different brain regions of zebrafish larvae, with neuronal resolution and minimal photodamage. High frame rate recordings were performed in the optic tectum to extract information about the dynamics of large neuronal circuits. Long term experiments were also performed, brain-wide, to assess the possibility to predict spontaneous behaviours. Finally, by using two-photon excitation, visually driven activity was recorded, in order to obtain information about the encoding of visuomotor responses.

This activity is the outcome of an internship in German Sumbre laboratory in the Institut de Biologie of the École Normale Supérieure in Paris. The light sheet setup was mostly ready at my arrival. I optimized its performances in

Chapter 4. Calcium Imaging in the Brain of Zebrafish Larva

terms in spatial and temporal resolution and added the two-photon excitation path. For the preprocessing of the data, I relied on the routines that were already available in the team, adapting them to my needs.

4.1 Introduction

The nervous system is a complex structure. Its main activity is the generation, acquisition, processing and transmission of information between body structures. To maximize the chances of an organism survival, these tasks should be performed in the fastest and most efficient way. Evolution led indeed to the development of an extremely intricate network of excitable cells, the neurons, organized in a central processing unit formed by the brain and the spinal cord, with terminations in every area of the body. In humans, the brain contains 10^{11} units, each forming on average 10^4 contacts, or synapses, to receive information through dendrites (in the short range) or to send them through axons (in the long range) in the form of electric pulses.

The understanding of the brain interaction with the external world cannot disregard the intrinsic brain dynamic, which can be studied under conditions of minimal sensory drive. Traditionally, in studies involving evoked activity the spontaneous brain activation was considered as fluctuation with no purpose in the processing of information, which averages out in statistical analysis. However, it has been observed that even when the external stimulation is completely removed, sensory brain areas remain highly active. Indeed, the traditional view has been challenged by recent findings, suggesting that spontaneous activity affects brain processing and behaviour for the following reasons: i) it is spatially and temporally structured at a coarse level; ii) it partially explains the variability observed in neural responses induced by identical stimulation trials; iii) it is influenced by the brain state; iv) it echoes fragments of former sensory experiences [76]. Describing and understanding the network which underlies the complex interaction between spontaneous and sensory-induced neural responses requires firstly an experimental pipeline to analyse the diversity of scales encountered.

Because of the huge intricacy of the brain network, it is worth focusing scientific and technological efforts on a circumscribed number of animal models. The model organisms that are being used in this context, each one with different complexity, span from *C. Elegans* (302 neurons) to the *Rhesus macaque*


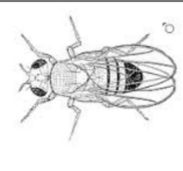



<i>Caenorhabditis elegans</i>	<i>Drosophila melanogaster</i>	Zebrafish larva	Mouse	<i>Rhesus macaque</i>
				
302	~135000	~100000	~71000000	~480000000

Figure 4.1: Animal models in neuroscience. The last row indicates the estimated number of neurons. For Rhesus macaque, only cortical neurons are considered.

($\sim 5 \cdot 10^8$ only the cortical neurons) and pass by the zebrafish (*Danio rerio*) larva ($\sim 10^5$), as shown in Figure 4.1.

In particular, the zebrafish larva is nowadays becoming the leading model for neuroimaging. Developmental and genetic research have taken advantage of the transparency of this small embryo since the late 1950s. A large library of transgenic and mutant fish lines is now available, providing a vertebrate model of neurodevelopmental, neurological and neurodegenerative diseases.

In this work, the implementation of a digital scanned light sheet fluorescence microscope finalised to study both spontaneous and evoked activity in the zebrafish larva is documented. The system has been used to record at high frequency spontaneous events at the same rate of electrophysiology. The acquisition has been performed in a specific brain area, the optic tectum, which has been found to be an ideal model to study functional visual circuits. The analysis of this dataset led to the observation of structured dynamics in the neuronal populations. Thanks to the low photobleaching of the technique, it was also possible to record brain-wide spontaneous activity in the long term (6 hours) and predict behavioural outcome of the larva from the data examination. Finally, visually evoked activity was acquired by implementing two-photon excitation not to disrupt the visual perception of the sample, and analysis finalized to extract information about the encoding of orientation selectivity was performed.

Chapter 4. Calcium Imaging in the Brain of Zebrafish Larva

4.1.1 Recording the brain activity

The oldest method to study the brain in animal models is to record neuronal activity. In neurons the signal of interest is electrical by nature. Thus, it can be directly monitored by means of electrodes inserted into the extracellular medium, as reported in 1957 for a cat [36]. The electrophysiological method has an excellent temporal resolution which allows one to sample single action potentials and resolve even subsequent trains of these. On the other hand, an electrode can, at best, record the activity of a hundred of neurons within $50\ \mu\text{m}$ around its edge, which is far from being able to analyse the whole brain. Moreover, electrodes are inserted blindly, so it is not possible to know precisely what are the recorded neurons without dissection at the end of the experiment. In fact, this is the major weakness of the method: its invasiveness.

A different approach is the one of the functional Magnetic Resonance Imaging (fMRI) [66], which associates brain activity to changes in blood flow and oxygenation. This technology is capable of measuring a whole brain and is the method of choice for human studies. It led to considerable advances in the description of human brain activity during different sensory conditions or tasks. The drawback of fMRI is the low speed (0.5 Hz) and low spatial resolution (in the order of the millimeter), although the same machine can be used to make a morphological steady image of the brain (MRI).

In between these two techniques, in the last 20 years, optical methods have emerged, combining the possibility to observe the Ca^{2+} dynamics and a spatial resolution sufficient for discriminating individual neurons. Moreover, neuroimaging includes the possibility to distinguish between different neurons by genetically targeting specific cell types and the possibility to manipulate the neuronal activity via optogenetic methods [103]. For functional studies, these methods rely on the use of fluorescent probes. Although *in vitro* results are very encouraging, the brightness of fluorescence indicators sensitive to membrane potential [51] must be improved to consent their use in *in vivo* experiments. Probing the change in ion concentration is the ruling choice, with Ca^{2+} being the ion *par excellence*, as explained in Chapter 1 [29]. During an action potential, Ca^{2+} rapidly enters the neuron, rising its concentration by a factor of 10-100, and in a few hundreds of milliseconds is slowly pumped outward. The signal to noise ratio is indeed adequate for brain imaging.

Because of the brain thickness and diffusive properties, standard epifluorescence microscopes cannot be used for brain imaging, while confocal imaging, though still being widely used, is being replaced by two-photon microscopy.

However, both these techniques suffer of the same issue: they are point scanning, hence the time necessary for the acquisition of an image is proportional to the number of points that compose it. This approach imposes a limit in the recording speed, and because of the trade-off between imaging rate and image size eventually restricts the number of cells that can be dynamically analysed. In the neuroscience framework, light sheet fluorescence microscopy offers the possibility to image neuronal activity on large-scale by monitoring a lot of cells at the same time from different brain areas. Recording the behaviour of neurons inside their population is recognized as a vital point in modern functional neuroscience, since most neurons are connected in structure called circuits [104]. The connections between different neurons can embrace multiple brain areas, for example the optical and motor ones. Therefore, measuring the neuronal activity across the whole brain (or at least a large part of it) with a multineuronal approach would be of great interest. Light-sheet imaging has already proved able to acquire large fields of view with single cell resolution and with temporal image sampling of up to the kHz range. The increase in the speed of acquisition is tremendous if compared to the 4-5 Hz of a two-photon microscope for imaging a single plane. The LSFM velocity of recording can also be exploited to create 3D functional stacks with a remarkably low photodamage for the sample, which enables one to accomplish time-lapse measurement lasting hours.

Obviously, the sample of interest must be chosen wisely to exploit all the advantages of such a technique. Whole brain imaging of mouse brain have been done in cleared samples [21, 89]. The first application of LSFM in functional neuroscience was to map olfactory responses in the mouse vomeronasal organ, but in rodent the brain is difficult to reach because the orthogonal geometry limits the area that can be imaged. LSFM has lately found a good model candidate for circuit activity in zebrafish larvae [2, 70].

4.1.2 Zebrafish as a model organism

The zebrafish (*Danio rerio*) is a promising vertebrate model for neurobehavioural research and for functional neuroimaging. Originally, the interest for this animal mainly concerned the vertebrate development thanks to the ease of breeding and its fast extra-uterine growth, with major organs recognizable already at 24 hours post-fertilization. They are easy to maintain, become fertile at 3 months and each fish can produce dozens of eggs daily. Its genome has been completely sequenced and is widely available to the community,

Chapter 4. Calcium Imaging in the Brain of Zebrafish Larva

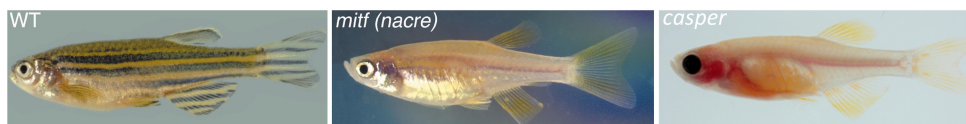


Figure 4.2: Adult zebrafishes of different transgenic lines. From the left: wild type, *nacre* and *casper*.

with thousands of existing transgenic lines. Some of these fish lines, reported in Figure 4.2, are almost pigmentation free, like the *nacre* which lacks skin melanocytes or the *casper* that is almost entirely transparent, but has vision issues.

Anyway, at the larval stage the zebrafish is naturally almost transparent, which explains why it is particularly appropriate for optical imaging. Moreover, its relative small dimension ($\sim 0.4 \times 3 \text{ mm}^2$ larva) makes it ideally suited for *in toto* imaging of the brain at cellular resolution using optical methods. Its brain

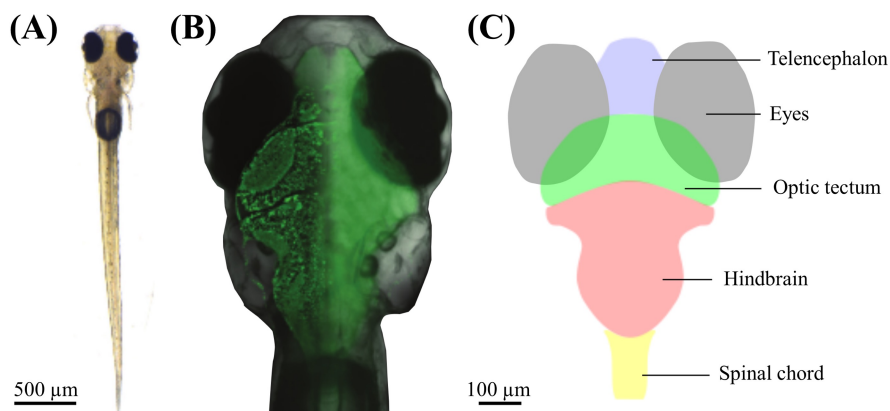


Figure 4.3: Coarse brain anatomy of a 6 dpf zebrafish larva. (A) Bright-field image of a zebrafish larva. (B) Overlay of a bright-field image of the larva head with images of its brain acquired using two-photon microscopy (left part of the brain) and fluorescence imaging (right part of the brain). Note the spatial resolution on the left part obtained with a two-photon microscopy. Neurons are labeled with the green fluorescent calcium indicator GCaMP5G. Image reproduced from Fetcho and coworkers [25]. (C) Schematic drawing of the brain of the larva showed in (B) representing the main parts of the brain (telencephalon, optic tectum, hindbrain and spinal cord) and the eyes. The 100 μm scale bar is common for (B) and (C).

contains roughly 80000 neurons, almost 6 orders of magnitude less than monkeys but more than 3 orders of magnitude more than *C. elegans*. Hence, the level of complexity of neuronal circuits is advanced. Finally, even at the larval stage, this specimen is a behaving animal. In fact, in natural environment, at 6 days post-fertilization (dpf) the larva needs to catch preys and avoid predators. This evolutionary pressure led to a fast development of a functional sensory system, especially vision as well as a wide repertoire of motor behaviours, able to perceive the external world, react or just think. At 6 dpf, the brain is $\sim 500 \mu\text{m}$ thick and $\sim 3 \text{ mm}$ long, with compact neurons. Different brain areas are well spatially separated, but still all close together, as shown in Figure 4.3(C). Hence, they can in principle be acquired all together. The larva breaths through the skin until 9 dpf. Therefore, the sample can be immobilized by embedding it into a gel instead of anesthetize or paralyze it, leaving the mobile parts unrestricted. The possibility to monitor different brain regions at the same time in a behaving animal makes zebrafish a key model for understanding how the brain is encoded and generates behaviour [1].

4.2 Experimental setup

4.2.1 Zebrafish preparation

In this work, the Nacre transgenic zebrafish line was used. This line expressed the genetically encoded calcium indicator GCaMP5G [3] under the control of the pan-neuronal HuC promoter were used. Since in neuronal activity studies the interest focuses to the relative variation of the fluorescence intensity, a non-ratiometric probe was appropriate. As discussed in Chapter 1, the GCaMP5G belongs to the pericam family. A variation in the $[\text{Ca}^{2+}]$ enhances the green fluorescence at 520 nm of the protein when excited around 485 nm. The larva brain showed homogenous distribution of the probe all over the neurons, fact that is also proof of good sample status.

Even if at the larval stage zebrafishes are naturally transparent, the Nacre present even less pigments. The line was developed by Jonathan Boulanger-Weill. Eggs were collected and raised at 28°C in E3 embryo medium and kept under a 14/10 h of on/off light cycles. After 5 dpf the embryos were fed with paramecia and at 6 dpf they were ready to be imaged. At 9 dpf, when the larvae start to use the gills to breath, they were euthanized.

All experiments were approved by *Le Comité d'Éthique pour l'Expérimentation Animal Charles Darwin* (Ce5/2009/027).

Chapter 4. Calcium Imaging in the Brain of Zebrafish Larva

4.2.2 The Digital Scanned laser Light sheet based fluorescence Microscope

The setup of choice is a Digital Scanned laser Light sheet based fluorescence Microscope (DSLIM). This system was chosen because it ensures a higher fluorescence signal upon equal average power with respect to the SPIM. The field of view is also more uniform, with the peripheral part as bright as the central one, which allows the optimization of the used power. This gains more importance when running long experiment under continuous illumination. Moreover, as discussed in Chapter 2, the lateral uniformity of the light sheet provided by DSLIM is higher, which should not be underestimated for samples that are as big as a zebrafish brain. the lateral uniformity of the light sheet provided by DSLIM is higher, which should not be underestimated for samples that are as big as a zebrafish brain. Last but not least, the illumination created by a cylindrical lens is more prone to shadows than the one of DSLIM. The far field, i.e. the angular spectrum, of a typical DSLIM beam extends along two axes. Hence, it is wider than that of the astigmatic light sheet generated by a cylindrical lens, which is squeezed along one axis. Within the geometrical optic approximation, any obstacle casts a shadow along a specific direction. Therefore, a beam characterized by a poorer angular spectrum is more sensitive to shadows. In the specific case of a larva, the obstacles can be skin pigments as well as red blood cells flowing in vessels. The latter are the most problematic: algorithms have been developed for static shadow removal, but when doing functional imaging the fluorescence variations due to a non-homogenous illumination can be attributed to a functional drive.

The system, shown in Figure 4.4 and Figure 4.5, was built in German Sumbre laboratory in the Institut de Biologie of the École Normale Supérieure in Paris and was partially implemented by Adrien Jouary. A CW laser emitting at 488 nm (Phoxx 488-200, Omicron) was used as a source and after an interferential filter (XX.F488, Omicron) it was coupled to a single mode fiber (Qioptiq, KineFlex) to spatially filter it and get a gaussian beam. Its power can be selected via software and was set at 0.3 mW. A telescope with magnification $M = 3.5$ ($f_1 = 35$ mm LA1131-A-ML and $f_2 = 125$ mm LA1433-A-ML, Thorlabs) is used to expand the beam to a radius ($1/e^2$) of 1 mm. The laser is then sent to two orthogonal galvanometric mirrors (Mounted XY 5 mm galvo sets, Cambridge Technology) for the lateral and axial scanning, with the beam covering the whole reflecting surface, without being clamped. The oscillations are adjusted as a function of the exposure time, but are always

4.2. Experimental setup

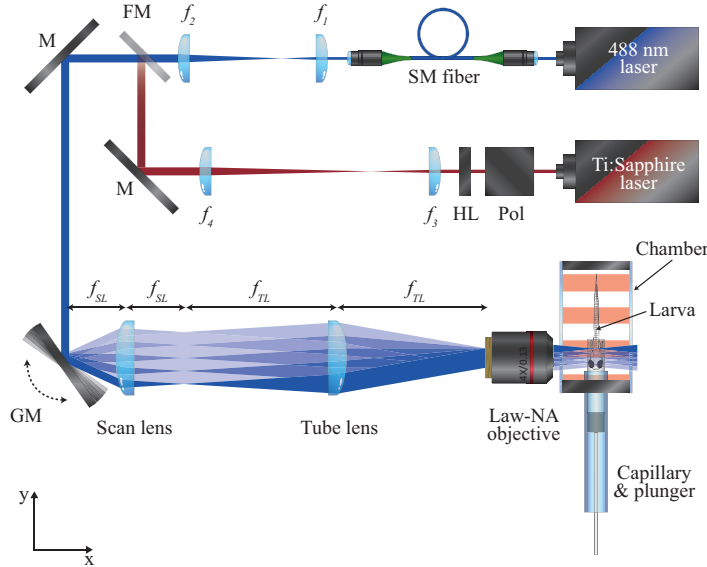


Figure 4.4: Top view of the excitation path of the DSLM setup. Up: top view, excitation path. A laser emitting at 488 nm coupled with a single mode fiber is expanded by a telescope ($f_1 = 35$ mm, $f_2 = 125$ mm). The beam is then quickly scanned by two orthogonal galvanometric mirrors, whose angular displacements are converted into position displacement by a scan lens ($f_{SL} = 75$ mm) and pivoted on the back-focal plane of a 4X low-NA objective by a tube lens ($f_{TL} = 180$ mm). The sample is placed in medium-filled chamber, head-fixed in a agarose cylinder in a capillary. A second path for two-photon excitation exploits a Ti:Sapph laser expanded by a $f_3 = 75$ mm and a $f_4 = 200$ mm lens, and recombines with the one-photon path by a flipping mirror. M=mirror, HL= half-wave plate, Pol=polarizer, FM= flipping mirror, GM= galvanometric mirrors.

performed around the mirrors oscillation axis with a triangular waveform in order to obtain an angular displacement at constant speed. A 2 inches scan lens ($f_{SL} = 75$ mm, AC508-075-A-ML, Thorlabs) is placed at his focal distance from the mirrors. The scan lens translates the angular deflections into position displacements. After it, a tube lens ($f_{TL} = 180$ mm, U-TLU, Olympus), positioned at $f_{SL} + f_{TL}$ from the previous optic element, refocuses and pivots the beam to the entrance pupil of a low-NA (0.16) 4X illumination objective (UPlanSAPO 4X/0.16, Olympus). This ensures that, for all the scanned angles, the entire beam passes through the objective, whose back-focal plane is conjugated to the galvanometric mirrors. By scanning the beam with the faster

Chapter 4. Calcium Imaging in the Brain of Zebrafish Larva

galvanometric mirror over an angular range of 6° , a horizontal light sheet is created, while the other mirror is exploited to move the light sheet vertically through the sample, which is kept steady. In this way, the horizontal sectioning allows to mount the zebrafish dorsal-side up for minimal invasiveness.

The larva is embedded in an agarose cylinder, extruded from a glass capillary (701904 glass capillaries and 701932 plunger, Brand). The agarose is used here, like in the setup for *Arabidopsis* plants, because of its index of refraction similar to the one of water, helping in minimizing the optical interfaces. The cylinder is inserted in a home-made chamber, filled with the Embryo Medium (EM). Two facing sides of the chamber are made of cover slides to allow the beam to enter and exit without optical aberrations and stray-light. A third side is drilled in the central part to allow the capillary to be inserted and removed, as well as rotated to ensure a good positioning for the larva. The bottom of the chamber is made of glass and is covered with a translucent diffusive screen to allow the projection of visual stimuli. The chamber is free-standing mounted on a 3-axis translation stage to permit the sample positioning.

The same system is also provided of a second illumination path for two-photon DSLM. The aim of using IR light is mainly to be able to perform visual stimulation of the larvae without the interference of visible radiation. A femtosecond Ti:Sapphire oscillator with automated dispersion compensation and a repetition rate of 80 MHz (Mai Tai DeepSee, Spectra-Physics) is used as a source. The selected wavelength for two-photon excitation of the GCaMP5G is 940 nm. The laser power is adjusted by properly rotating a half-wave plate (AHWP05M-980) after a polarizer (GTH5M-A) and set to 300 mW. The beam is expanded with a 2.67X magnifying telescope ($f_3 = 75$ mm LA1608-B-ML and $f_4 = 200$ mm LA1708-B-ML, Thorlabs). After that, the beam is sent to a flip mirror and recombines with the one-photon excitation illumination path. All the following optics are kept the same. The laser pulses have been characterized at the sample by means of a measurement technique for ultrashort laser pulses based on Frequency-Resolved Optical Gating or FROG (GRENOUILLE [68]) in order to get the shortest pulse duration possible. In fact, the shorter the pulses the higher is the peak power density at the sample and indeed the higher the fluorescence excitation. The shorter pulses measured had a duration of 78 fs, in line with theoretical calculations based on the spectral band of the laser (690-1040 nm) and on the instrument specifications.

Below the chamber, a pico-projector (PK320, Optoma) was used for visual stimulation during evoked activity experiments. The stimuli were projected on the diffusive screen below the larva. Note that the screen must be at a distance

4.2. Experimental setup

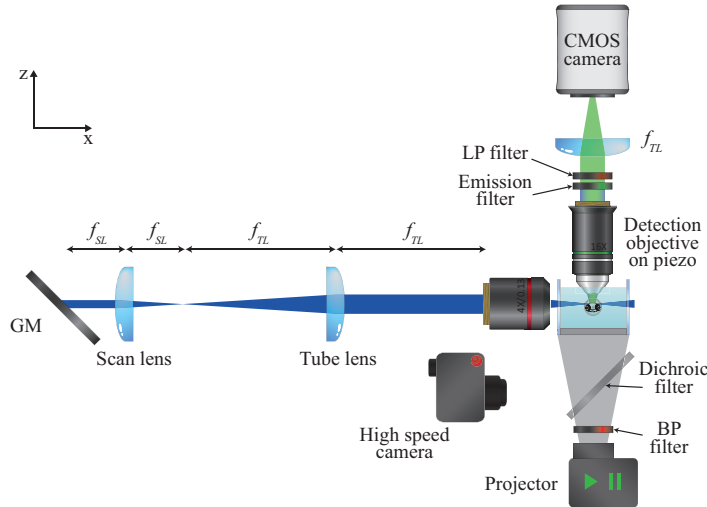


Figure 4.5: Side view of the detection path of the DSLM setup. A 16X water-dipping objective mounted on a piezo sends the fluorescence signal through a band pass emission filter, a low-pass filter to reject IR light, and a tube lens to the CMOS camera. Below the chamber, a projector for visual stimulation and a high-speed camera for tail movements detection are positioned. GM= galvanometric mirrors.

of 5 mm for the fish to properly see it. The stimulation consisted on a square wave grating with a spatial period of 10 mm with maximal contrast. This grid is moving orthogonally to the direction of the stripes and its orientation changed 9 times with an angular displacement of 40° . The light from the projector is filtered (Band-Pass Filter FF01 629/56, Sermrock) in order to avoid any background from the projector in fluorescence images. The system also provides a high-speed camera (Hxg20nir, Baumer) used to monitor the behaviour of the larva. For this purpose, the fish was illuminated through an IR led, invisible for the larva. A small hole in the screen below the sample chamber allowed imaging of the locomotor activity of the larva.

The detection stage, presented in Figure 4.5, is the same for one and two-photon excitation and is mounted vertically on a pole. The pole itself is fixed on a 2-axis translation stage to match the focus of the light sheet. The optical path consists of a high-NA water-dipping objective (16X, 0.8 NA, Nikon), mounted on a piezoelectric translation stage (PI PZ222E). This is of course necessary to finely match the focal plane of the detection objective to the light sheet, as well as to follow its vertical displacements, for example during 3D

Chapter 4. Calcium Imaging in the Brain of Zebrafish Larva

acquisitions. To this purpose, the vertical-scanning galvanometric mirror was synchronized with the piezo. The collected GCaMP5G fluorescent signal is filtered by a band-pass filter (525-50, Semrock) and, in case of two-photon excitation or IR illumination for behavioural imaging, also by a low-pass filter (FF01-680 SP25, Semrock), both for cutting the excitation laser and the light for visual stimulation. The fluorescent image is projected by an Olympus tube lens on a sCMOS camera (Orca Flash 4, Hamamatsu, provided with Camera Link), synchronized with the oscillations of the galvanometric mirrors, whose scanning frequency ensured at least 10 scans per exposure time, and when recording the larva behaviour, also with the monitor camera. To align properly the sample and to observe the wide field image of the specimen, white light can be shined from below the chamber. The head of the fish must be as close as possible to the capillary, which in turn must not intercept the excitation beam.

4.2.3 Sample mounting

The mounting procedure is aimed to head-fix the zebrafish larva in order to allow the imaging experiment with minimum stress for the fish. In the morning the 6 dpf larvae are taken from the incubator and selected on the basis of the best fluorescence expression. The chosen larva is placed in a Eppendorf filled with 2% low melting point agarose, previously prepared and stocked in a thermostat at 40°C. This temperature is just above the solidification temperature of the gel (36°C), and is compatible with the larva survival. The agarose with the sample is then placed on a petri dish and observed through a stereomicroscope. Quickly, before solidification, the larva embedded in agarose is aspirated in a glass capillary with a diameter of 1 mm, being careful not to form air bubbles, which can collapse during the experiment. The larva is sucked from the head, with the body as straight as possible and in the center of the capillary. Embryo medium is immediately poured in the petri dish and delivered to the embryo through the agarose. After solidification of the gel, a cylinder of agarose with the embedded larva is obtained. Note that during the whole procedure, the fish should be maintained dorsal-side up and outside of the glass capillary to minimize stress and to help it breathing (Figure 4.6). For the same reason, the agarose around the tail is cut with a small blade and removed, fact that also allows the tracking of the tail movements. The sample is then ready to be inserted in the imaging chamber filled with embryo medium, where it is extruded and left to settle for a few minutes.

After every experiment, the fish needs also to be freed, for ethical purpose

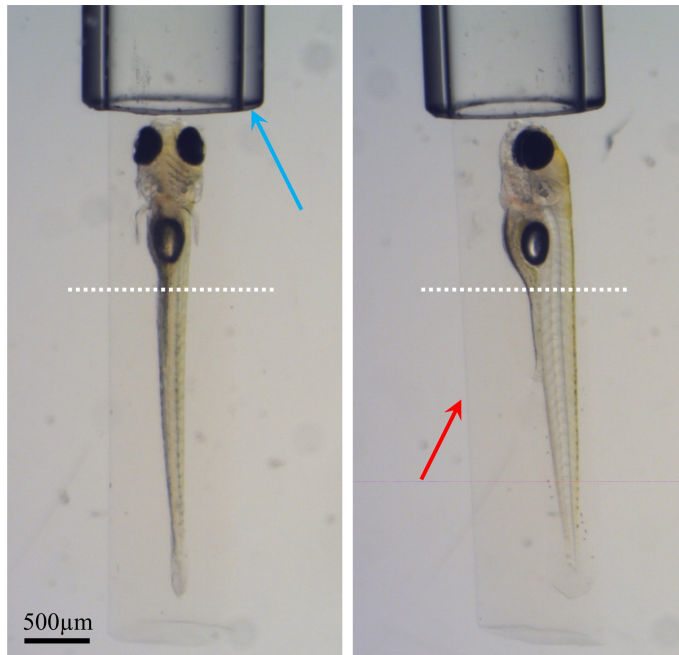


Figure 4.6: *Zebrafish larva embedded in agarose. The larva is head-fixed in agarose (shown by the red arrow) after being aspirated in a glass capillary (shown by the blue arrow). The body should be as straight as possible and in the center of the agarose cylinder. the agarose is usually removed from the tail by cutting it along the dotted line and gently pushing it away from the tail of the fish.*

in first place, secondly to check the larva status. The capillary is placed on a petri dish filled with EM, the sample is extruded and the agarose around it is cut and gently removed. Usually, even after several hours of experiments, the larva immediately starts to swim and behave normally, meaning that the overall technique is minimally invasive. The same larva could even be imaged again on the following days.

4.2.4 Imaging performances

The Orca-Flash4.0 has 2048x2048 pixels with a cell size of $6.5 \times 6.5 \mu\text{m}^2$. The camera can record images up to 100 Hz at full frame at binning 2x2, while the speed roughly doubles when the frame size halves. This kind of high data rate has special requirements for the computer. The camera is connected to a workstation with 1 TB solid-state hard drive for quickly saving the images and

Chapter 4. Calcium Imaging in the Brain of Zebrafish Larva

64 GB of RAM. It must be taken into account that the acquisition software of the camera generates a single file out of each measurement. Indeed the memory requirement was an upper limit for the experiment. Recording images at 100 Hz, full frame at binning 2x2 would lead to 1 TB of data in just 80 minutes. This means that only an image subset can be acquired.

One of the most remarkable advantages of the DSLM implemented is the wide field of view, which enables to look at a section of the whole brain of the larva in a single image. The field of view is $920 \times 920 \mu\text{m}^2$. Hence, one pixel corresponds to $0.45 \mu\text{m}$ when the binning is set at 1x1. It is possible to observe at the same time different brain areas, with different functional and sensory roles, from the telencephalon to the first part of the spinal cord, as shown in Figure 4.7 and Figure 4.8. Single neurons can be distinguished, having a diameter of $7 \mu\text{m}$. The number of pixels per neuron is around 180 (45 at binning 2x2), limiting the average noise. These results are something not achievable with traditional sectioning microscopes, where the point scanning approach limits the image dimension to a single brain sampled with 256×256 pixels (512×512 pixels at best).

Three-dimensional functional recording can also be performed. What usually limits the speed of 3D recording in DSLM, is the time needed by the piezo stage of the detection objective to move and settle. Also, the camera records only when the piezo is stabilized, which can take tens of milliseconds. In the implemented system, the camera was always acquiring at 100 Hz and the piezo-positioner was performing a single smooth movement from the initial to the final position, synchronous with the light sheet. This latter, was generated vertically with a triangular modulation. This led to 3D functional images of $200 \mu\text{m}$ depth at the remarkable speed of 4 Hz. The drawback of this approach is that, since only 20 planes were actually recorded, the images were integrated over $10 \mu\text{m}$, meaning that the axial resolution is limited by the speed of acquisition and not by the light sheet itself. However, $10 \mu\text{m}$ is still compatible with the dimension of the somata, i.e. the neurons bodies. Figure 4.8 shows a subset of planes from a $200 \mu\text{m}$ -thick volume imaged at 4 Hz. The theoretical beam waist of the gaussian beam reaching the sample in one-photon configuration is $2.3 \mu\text{m}$, given a collimated beam diameter at the entrance of the first telescope equal to 0.7 mm, approximating the 4X Olympus objective with a thin lens of $f = 45 \text{ mm}$ and assuming a homogeneous refractive index of 1. However, the beam partially travels inside water after going through the glass optical window of the chamber. The axial profile was therefore assessed by embedding fluorescent beads of a diameter of $0.1 \mu\text{m}$ (Molecular Probes)

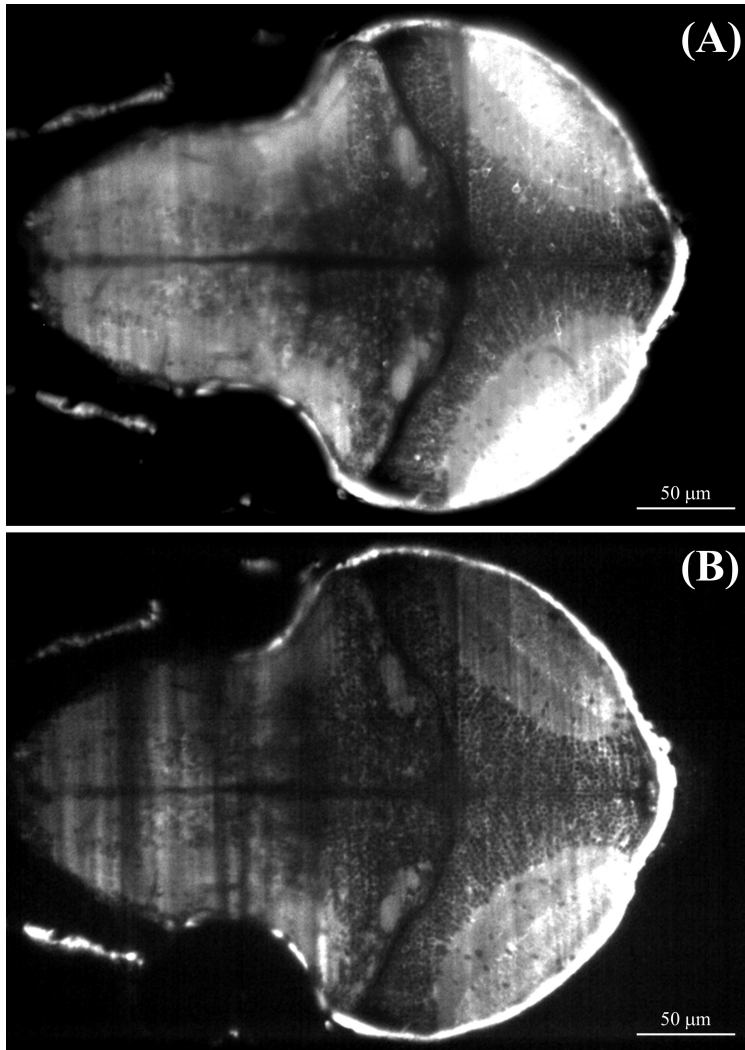


Figure 4.7: *One and two-photon 2D images of zebrafish brain. The same larva was imaged with both ne-photon (A) and two-photon (B) excitation. Single somata can be clearly distinguished all across the brain. different brain areas can be imaged at the same time thanks to the wide field of view. On both images, some stripe effect can be observed: in this specific case, a big shadow is casted on the left hemisphere. Because of the non linearity of the two-photon excitation, shadowing effects are more visible in (B). The displayed images are the result of an average over 2000 frames acquired at 10 Hz.*

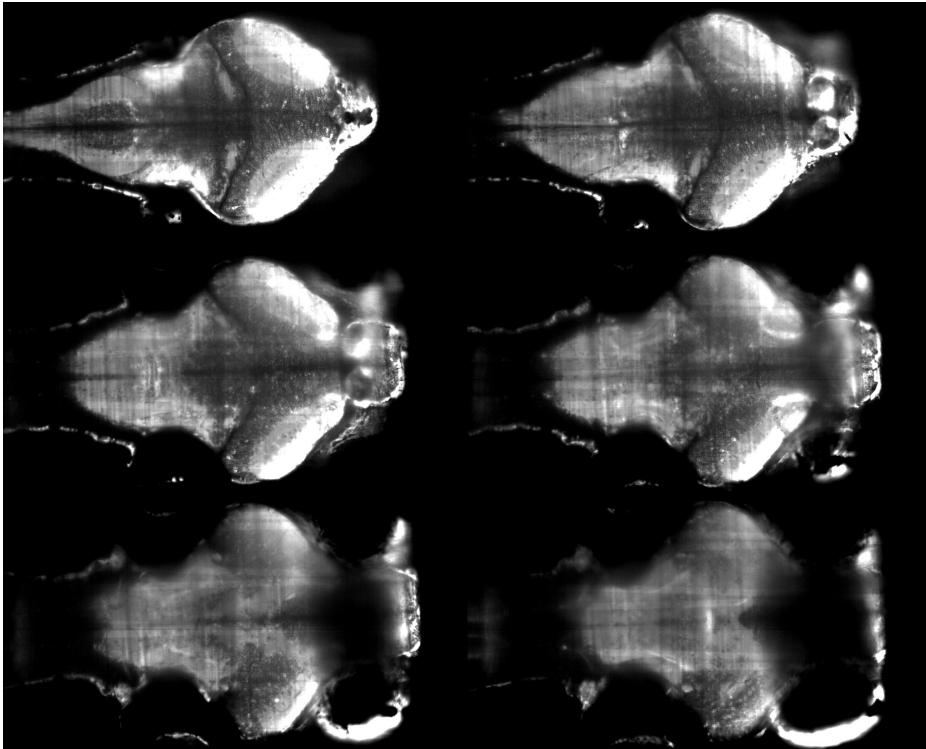


Figure 4.8: *3D imaging of zebrafish brain. The acquisition was done at 4 Hz, recording 20 planes spaced of 10 μm , time exposure per plane equal to 10 ms. Only a subset of the planes (one every 30 μm). Single neurons can still be observed, even when the light sheet is deep in the sample. However, because of the light absorption from the retina, the ventral planes are affected by huge shadows which cover the telencephalon of the larva.*

in a cylinder of agarose, exactly in standard experimental conditions. A volume of gel was imaged by scanning the focused gaussian beam that creates the light sheet along the axial direction (z), while measuring the fluorescence intensity of the beads in the focal plane of the objective. The intensity profile of the bead emission, as a function of the gaussian beam position z , was fitted for the FWHM. In this way, the intensity profile of the excitation beam was explored along the full extent of the FOV as a function of the longitudinal position. Finally, the fit on the data displayed in Figure 4.9 led to a gaussian beam profile with $w_0=2.77 \mu\text{m}$ and a Rayleigh length of $66 \mu\text{m}$. The maximum spot size across the sample is then $17 \mu\text{m}$, given that a 6 dpf larva brain is almost

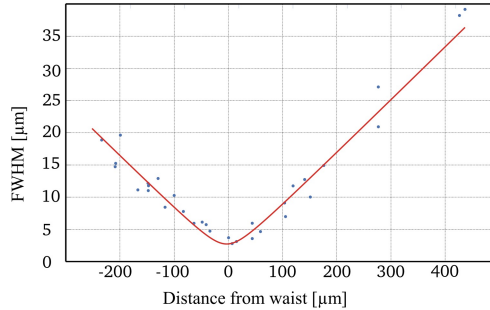


Figure 4.9: Axial light sheet profile. Each blue dot corresponded to a fluorescent bead of $0.1 \mu\text{m}$. Its full width at half maximum (FWHM) was computed by scanning the light sheet in the axial direction and measuring the vertical profile of the fluorescence intensity for each bead. The red line corresponds to a fit matching a gaussian beam profile with $w_0=2.77 \mu\text{m}$. The optical sectioning is thus compatible with single-cell resolution (the typical soma has a diameter of $\sim 7 \mu\text{m}$).

$400 \mu\text{m}$ large.

It is worth noting that with a less focalized beam, centers of absorption or obstacles in general would cast more prominent shadows, ruining the final image. In fact, as it has already been discussed for the case of a cylindrical lens, when a small obstacle intercepts a beam focalized to one point, the fraction of light passing beyond it increases with the NA of the beam. Therefore, with a more collimated beam, sharper shadows will be cast. The first telescope was modified multiple times in order to get a good compromise between these two necessities, finding in the presented data the best solution.

The two-photon optical path was conceived to get the same beam waist of the light sheet of the one-photon DSLM. As discussed in 2, theoretically in order to get the same axial resolution with the two excitation modalities, Eq. 2.8 must be fulfilled. Given the wavelength of the two implemented setups, the condition can be reduced to $NA_{2p}^2 = 1.36 \cdot NA_{1p}^2$. This requires that the IR beam dimension before the objective of illumination is 1.36 fold the one of the 1-photon excitation, condition that was satisfied by setting a beam expander before the galvanometric mirrors. This should give in principle the same field of view of the 1-photon system; however, difference in contrast between the central and peripheral part of the beam is not negligible.

Chapter 4. Calcium Imaging in the Brain of Zebrafish Larva

4.2.5 Preprocessing and signal extraction

For all the experiments, data analysis requires to isolate the fluorescence time course of each neuron in the FOV. To this purpose intensive data preprocessing is required, as it is discussed here upon.

Acquiring 16-bits images made by millions of pixels at a frame rate spanning from 10 to 100 Hz can lead easily to huge datasets. At the end of the day, it is not unlikely to obtain TBs of data. What is even scarier than storing so big files is that they need to be analysed. The experiments were uploaded on a storage server and went through a pipeline which was developed only for the preprocessing, common to all the experiments. This computationally intensive step was performed through a High Throughput Computing (HTC) system based on 328 CPUs. To give an order of magnitude, 80 minutes of recording at 100 Hz, binning 2x2, leads to 1 TB of data and 4-5 days of preprocessing using 100 cores of the HTC system. The chosen approach parallelizes the computation by automatically grouping all the raw images into packets of maximum 5000 images and sending each package to a core of the HTC system to analyse them. The outputs can be put back together on a local computer. All the analyses have been implemented in MATLAB environment.

The following steps are relative to single plane experiments, but can be iterated for 3D analysis.

Image segmentation

Because of the large number of neurons present in one DSLM image, two different automatic or semi-automatic segmentation procedures were applied to identify all the neurons.

The first, more complex but more controlled method, involves the use of the “watershed” algorithm. This algorithm looks at the image as a topographic map where the pixel intensity corresponds to the altitude, with local minima creating basins. These latter are imagined to be flooded by rain until the water level reaches the altitude of a peak or encounters another basin. There, a border is drawn and the whole image will be in this way partitioned, delimiting single neurons. A reference image was generated from averaging 10 s of recording taken in the middle of each experiment. On it, a mask for the area to be segmented was manually drawn. A watershed algorithm was implemented, with constraints on the shape of the Regions Of Interest (ROIs) like eccentricity or maximum area: well separated ROIs delimiting individual somata from the reference image were returned, although sometimes it was necessary to delete

and draw some of the ROIs.

The second technique is useful when many neurons are being imaged and the main aim is to look for groups of neurons. In this case, the masked reference image was covered in hexagons of side length equal to $6.3 \mu\text{m}$, which corresponds to an area roughly equal the soma of a neuron; however, there is no direct correspondence between single neurons and ROIs here. These hexagons were not touching each other and did not discriminate between neuropil, i.e. a dense region of dendrite and axons but containing a low number of neuron bodies, and neuronal somata.

Image registration

The second step in the image preprocessing requires to correct for possible drifts in the coronal $x - y$ plane, while drifts along the z axis cannot be corrected. All the frames were registered by finding the maximum in the cross-correlation with respect to the reference image. Large deviations in the cross-correlation between successive frames were considered as artifacts due to movements of the fish and removed.

Inference of fluorescence events

The preprocessing finishes with the fluorescence time course extraction. Firstly, individual ROIs must be validated by checking that they contain relevant signal. The average of the correlations between the fluorescence of each pixel and the average fluorescence of the ROI was indeed calculated. Figure 4.10(B) shows an example of ROIs colour-coded by this correlation. If the latter was lower than 0.3, the ROI was removed from the analysis. Then the time course of fluorescence signal from each of the remaining ROIs was extracted by evaluating the average intensity across the pixels for each registered frame. Figure 4.10(A) shows the average fluorescence behaviour from all the ROIs of a 6 h experiment: notably, the reduction in the fluorescence is only 6%.

For each relevant ROI a smooth fluorescence baseline $b(t)$ was estimated by computing around every time point a 30 s-long running average of the 8th percentile of the raw fluorescence data. The baseline reflects slow fluctuations in the signal unrelated to the fast calcium transients associated with the neuronal activity. The relative variations in the fluorescence intensity $\frac{\Delta F}{F}$ were indeed computed as

$$\frac{\Delta F}{F} = \frac{F(t) - b(t)}{b(t)} \quad (4.1)$$

Chapter 4. Calcium Imaging in the Brain of Zebrafish Larva

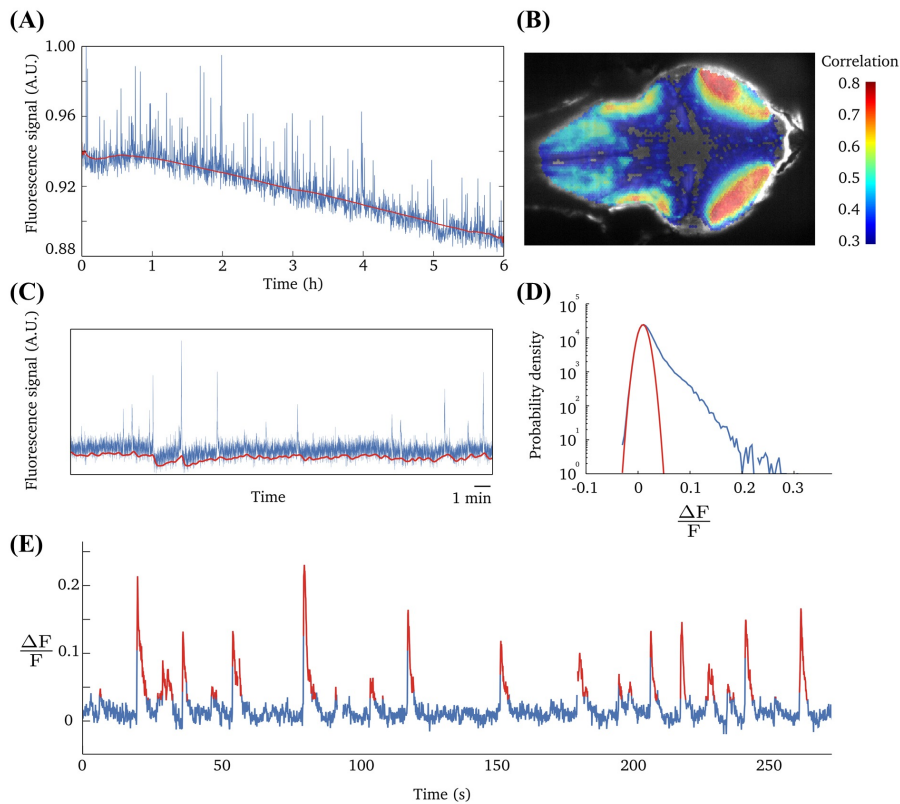


Figure 4.10: *Inference of fluorescence events. (A) Fluorescence signal averaged across all ROIs during the 6h of recording (blue) with running average of the fluorescent signal overlaid (red). The relative decrease in baseline fluorescence during 6 h is less than 6%. (B) Average pairwise correlation between pixels in each ROI. ROIs with a correlation below 0.3 were discarded. (C) Typical fluorescence signal from a single ROI (blue) with its baseline overlaid (red). (D) Probability density of the relative fluorescence changes $\frac{\Delta F}{F}$ of a typical ROI (blue) and the corresponding gaussian fit on values of $\frac{\Delta F}{F}$ smaller than μ (red). (E) Example of a typical time course of the $\frac{\Delta F}{F}$ (blue) for one ROI, with significant fluorescence transients. The signal above $3\sigma_{noise}$ are highlighted in red and represent the activation events.*

and a typical outcome is showed in Figure 4.10(C). In order to find statistically relevant signal variations, for each ROI the distribution of the obtained $\frac{\Delta F}{F}$ was plotted and presented a positively skewed distribution (Figure 4.10(D)) peaked at a value μ . Since in principle the fluorescence variations are positive, data

points smaller than μ were considered white gaussian noise. Hence, to estimate the noise contribution, these points were fitted with a normal distribution of mean μ and standard deviation σ_{noise} . Values of $\frac{\Delta F}{F}$ below $3\sigma_{noise}$ were set to 0, while those above $3\sigma_{noise}$ are considered the relevant activation events. ROIs with noise poorly fitted or with large noise level were discarded. Finally, the fluorescence transients were extracted by setting a threshold on each single fluorescence series. A typical trace obtained after analysis is shown in Figure 4.10(E). For most analysis, in fact what is needed is the timing of the activity events. The usual way to present a large number of traces is the raster plot, a graph displaying the activity of all the neurons of interest over time.

4.3 Experimental results

4.3.1 High speed recording of neuronal pattern in the optic tectum

From a biological point of view, the aim of this work is to explore the neuronal interactions emerging during spontaneous activations. As already stated, brain dynamics are very fast: electrophysiology has the advantage to be able to look at action potential variations, but is limited to the analysis of few neurons at the same time. In the scenario of calcium dynamics, being able to sample transients of fast calcium probes would allow one to indirectly look at action potentials with a speed comparable to that of electrophysiology, but from thousands of well spatially-defined neurons simultaneously. Anyhow, one must be aware that calcium dynamics look only at an effect of action potentials.

With standard microscopy recording at 4 Hz it has already been possible to observe ensembles of neurons activating simultaneously during spontaneous events. They resembled the patterns activated by external stimuli even in absence of sensory drive. Whether there could be some structures invisible when acquiring at a low frame rate, like 4 Hz, has never been investigated. A high frame rate may open the possibility to observe structures that resemble waves or even discriminate between neurons activating before others and triggering their activation, like recently shown in the visual cortex of mouse by Okun and coworkers [67]. However, the role of the delays between neuronal activation found in assemblies of the cortex has not yet been elucidated.

As a proof of concept of being able to record at high speed and extract significant information about neuronal dynamics from a large population of neurons, acquisition were performed on the optic tectum of 6 dpf larvae. The optic tectum was chosen since it is the most complex area and largest visual centre of

Chapter 4. Calcium Imaging in the Brain of Zebrafish Larva

the zebrafish brain, thus it is used for developmental and functional studies of vertebrate visual circuits. In zebrafish brain it is the most complex structure: it is used to map the external world and it is involved in spatial detection, motor orientation and attention.

Recordings at 100 Hz with binning 2x2 were executed with the one-photon setup for periods of 1 to 3 h in the absence of sensory stimuli. The blue light of the continuous illumination had a constant intensity and position, thus likely it did not provide salient sensory cues. ROIs typically of 400x400 pixel were acquired around one optic tectum, limiting as much as possible the acquired dataset to the area of actual interest. In case of 3 h recordings, 1080000 images are saved and the dataset can end up being even bigger than half a TB. This type of dataset needs 5 days for the preprocessing with the HTC system. From a computational point of view, it must be specified that it is not only the actual dataset dimension that counts, but also the number of images that have to be opened, processed and saved.

The somata were segmented automatically and after preprocess of the experiment around 500 to 700 were found significant. They showed sparse spontaneous activity with a low average frequency of activations (every 2 minutes) and less than 1% of the entire recorded population being active during those events. However, clear concerted events took place involving subsets of neurons of 2-5% of the population. These neurons showed significant pair-wise temporal correlation. The raster plot displaying the temporal behaviour of each neuron was created and is shown in Figure 4.13. The correlation between traces was calculated and the neurons were sorted maximizing the similarities in the correlation between their temporal behaviour. The ROIs were colour-coded depending on their ordering position after this sorting and displayed on the reference image Figure 4.11. The spontaneous activation of the optic tectum showed a continuous progression of colours, which is index of a spatial organization. In fact, in zebrafish the tectal neurons receive massive organized inputs from the retina of the contralateral eye, creating the so-called retinotopic tectal map of the contralateral visual field. The current theory states that in vertebrates these coarse retinotopic maps are established before the onset of vision, based on molecular cues, and later modified or refined by visual experience [14, 82]. In the analysed experiments, even in absence of retinal inputs, this retinotopy emerges.

The dataset was indeed tested for the existence of previously reported functional assemblies by applying a clustering procedures [78]. The activity time series were represented in a space of reduced dimensionality through Princi-

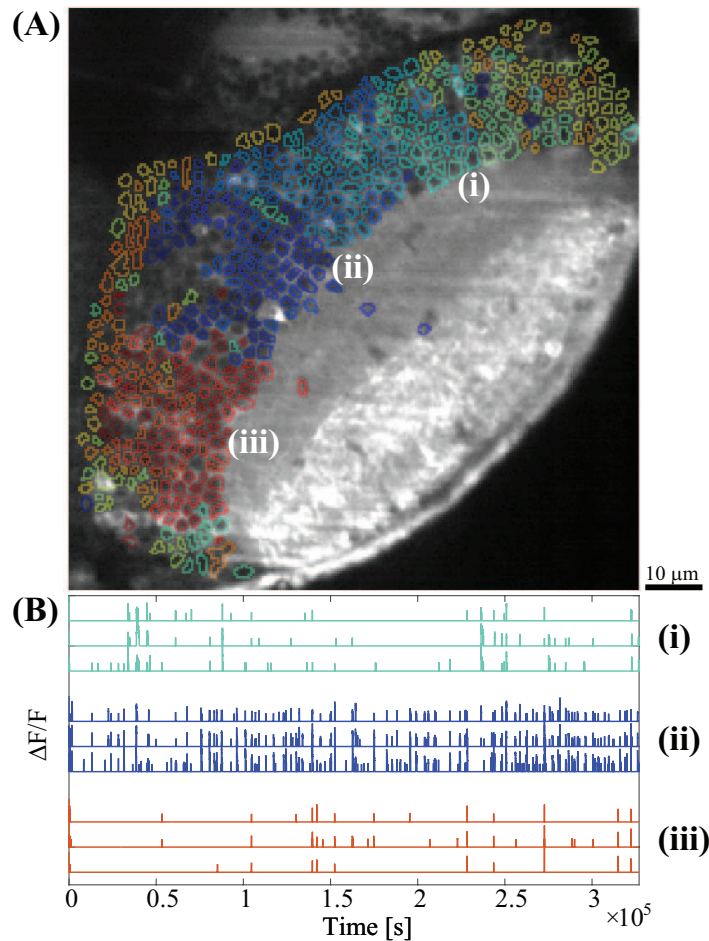


Figure 4.11: Retinotopic organization of the optic tectum. Single neurons have been segmented and colour-coded (A) based on the correlation similarity of their signals. B shows examples of the signal courses from three regions of the optic tectum.

pal Component Analysis (PCA) [52, 71]. Then, a second algorithm, *promax*, was used to partition the PCA space by means of a non-orthogonal factor rotation [34]. The overall procedure extracts collective neuronal activation with significantly correlated dynamics. The neurons involved in one of this highly correlated “assemblies” are a neuronal processing module. In the 100 Hz DSLM recording the PCA-*promax* method extracted 49 ± 3 assemblies, in agreement with what already reported by Romano and coworkers. Also, al-

Chapter 4. Calcium Imaging in the Brain of Zebrafish Larva

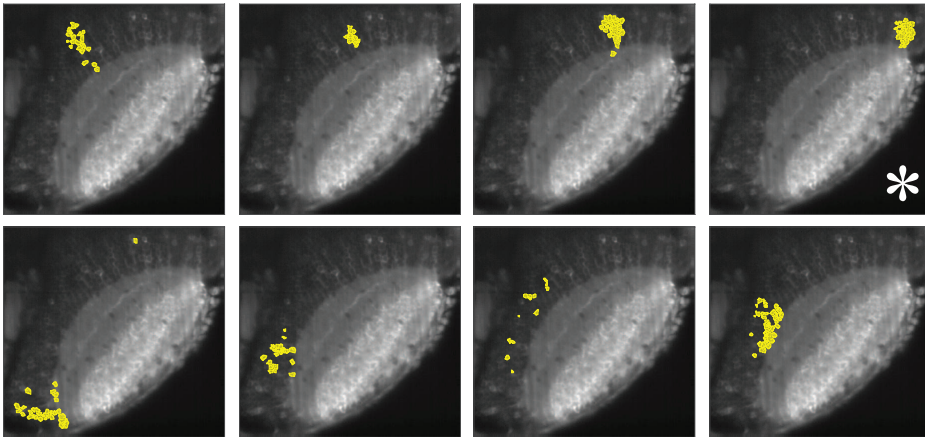


Figure 4.12: *Examples of PCA-promax functional assemblies in the optic tectum. The right one is marked with (*) and will be further analysed later.*

though the position of the neurons was not taken into account, the resulting assemblies are topographically compact. This type of assemblies resemble the neural patterning activated by visual stimulations.

To take advantage of the high speed of the recording, the question that was addressed is if during these concerted activations there were “soloists”, i.e. neurons firing before the others and triggering them. Firstly, a window of concerted activation had to be defined. A binary matrix of the activity of all the neuron was created, where 1 means active and 0 non active. An event histogram is then calculated by summing the binary activation traces of the whole population. A threshold on the event histogram was set to exclude non-significant events. The threshold value was defined by building a shuffled surrogate null model of the binary matrix. In the null model the temporal dynamics were randomized by permuting their time slots multiple times (1000 times, corresponding to a p -value $p = 0.05$ with uncertainty near it $\pm 1\%$). In this way, the number of time slots a neuron was found active is preserved. The event histogram of the null model defines the threshold below which an event on the real model can be explained by casualty (threshold marked in red in Figure 4.13). The events above threshold on the real population event histogram that were longer than 400 ms were considered as significant coactivation events, and a window of observation was opened at the time t they overcame the threshold. In order to be counted as part of the i event, a neuron had to fire significantly during the i time window, which means, more than the average firing rate within the whole

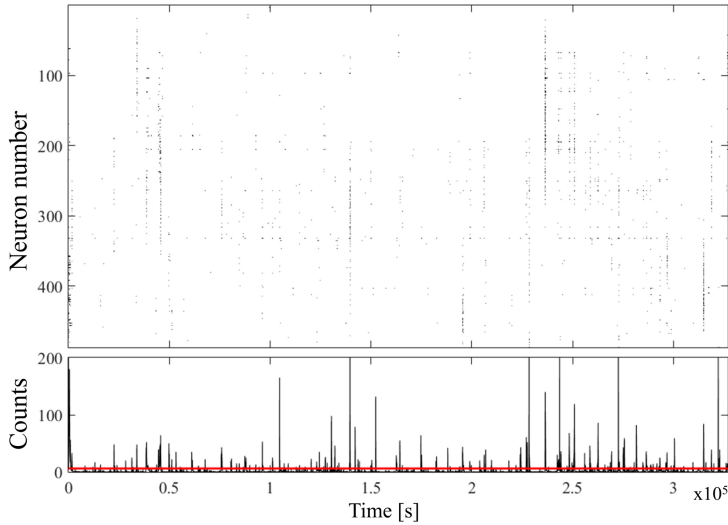


Figure 4.13: *Raster plot of spontaneous activity in the optic tectum. This matrix can be transformed to a binary raster to obtain a graph of the whole population events (lower panel) and to set a threshold for the significant events. The threshold is found by comparison with a null model and is highlighted in red in the lower panel.*

experiment.

The lags for every neuron active during the coactivation windows were evaluated. For each coactivation window, neurons were ordered based on their lag, colour-coded accordingly and overlaid on the reference image, and their time course was plotted. Figure 4.14 shows different coactivation events. Figure 4.14(A) displays an event involving one activation, while for example Figure 4.14(D) reports activity detected as a single event, but that actually involves two different coactivations (see the clear change in the slope of the upper graph). Figure 4.14(B) is too long to be a single event, hence is probably composed of three different clusters of neurons activating one after the other, starting from different layers of the neuropil. Figure 4.14(C) shows instead a coactivation event that looks like a smooth wave. This type of event is actually frequent (Figure 4.15) but has never been observed before in the zebrafish optic tectum. Also, along the same experiment, some brain area showed spatial patterns that frequently repeated themselves with even similar temporal dynamic (Figure 4.16). However, defining a single specific neuron firing before all the others every time was not obvious. As a matter of fact, although the temporal resolution of the system is suitable for the lags that were found, the sampling

Chapter 4. Calcium Imaging in the Brain of Zebrafish Larva

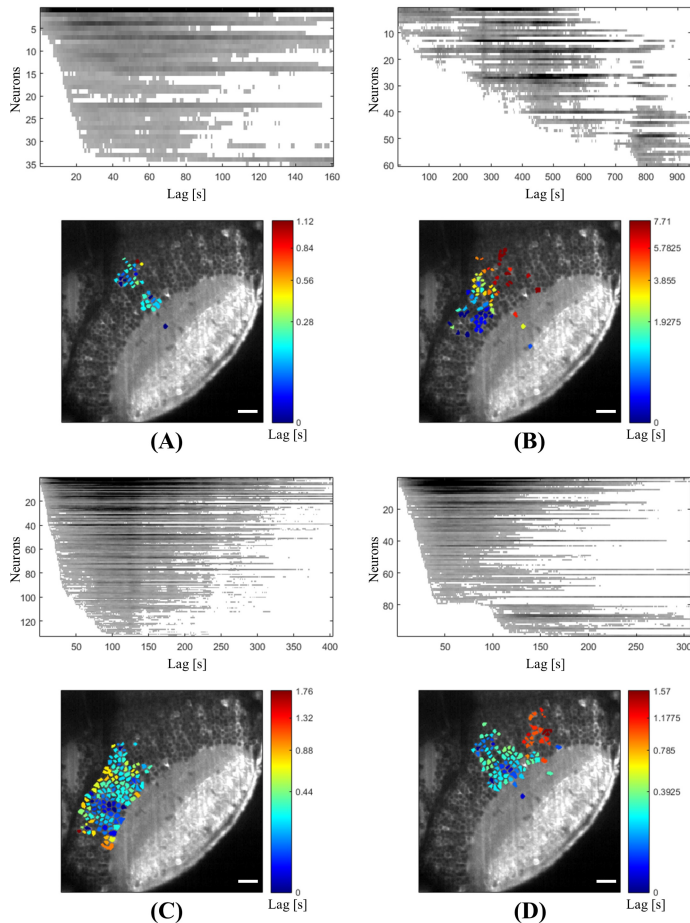


Figure 4.14: Single events maps. For each coactivation window, neurons were ordered based on their lag, colour-coded accordingly and overlaid on the reference image, and their time course was plotted. (A) displays an event involving just one activation, while (B) reports activity likely to come from three different events, starting from different layers of the neuropil. (C) shows instead a coactivation event that looks like a smooth wave. (D) reports activity detected as a single event, but that actually involves two different coactivations (see the clear change in the slope of the upper graph). Scale bars 10 μm .

is actually too high for a slow indicator like the GCaMP5G. Recording the frames at the frequency higher than required, increases the read noise without improving the signal content. A more efficient probing frequency would have

4.3. Experimental results

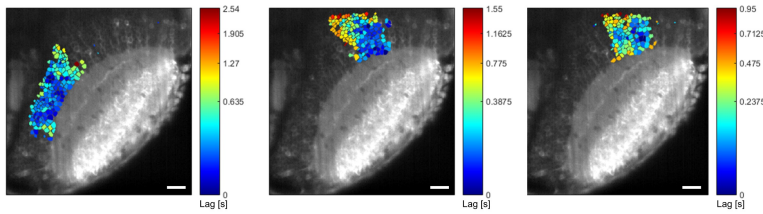


Figure 4.15: *Wave-like patterns in the optic tectum. A spatial progression of Ca^{2+} elevation has been detected, like in the cortex of other vertebrate models. Scale bars $10\ \mu\text{m}$.*

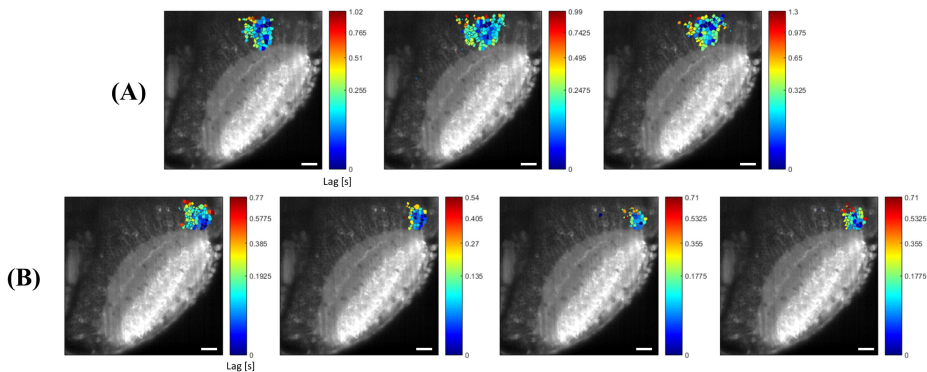


Figure 4.16: *Repeated events of coactivation, taking place with similar spatial dynamics. These neurons belong to a single assembly, marked with (*) in Figure 4.12. Scale bars $10\ \mu\text{m}$.*

been around 20 Hz.

Neurons were also colour-coded on the reference image based on their mean lag. Figure 4.17(B) shows that the somata in the central part of the tectum are those with the larger lag and are also more active Figure 4.17(A). This observation could suggest that the activation of the choristers is higher in this area, while peripheral neurons tend to fire in less complex events. However, this hypothesis should be supported by a more detailed analysis, that in this pilot study was not performed. Hence, inferring from this that soloists and choristers exist is not clear.

Another approach to evaluate onsets of activation events, is to exploit the high temporal resolution to deconvolve the fluorescence traces and really get close to electrophysiological capability of detecting action potential. This has actually been done trace by trace, but an algorithm (a modified version of the

Chapter 4. Calcium Imaging in the Brain of Zebrafish Larva

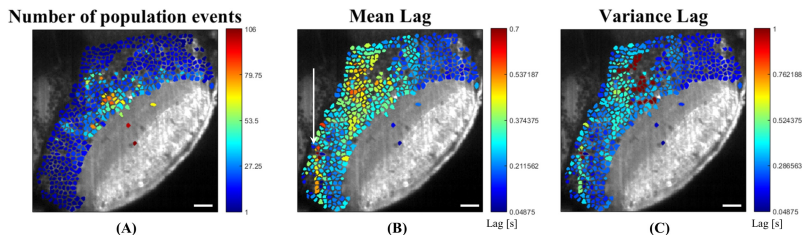


Figure 4.17: Analysis of the lag of neuronal firing during activation events. The number of population events a neuron is involved into (A), the mean lag of activation per neuron (B) and the variance (C) are shown. The white arrow indicates a column of neurons possibly affected by a moving shadow artifact. Scale bars 10 μm .

Fast non-negative deconvolution for spike train inference from Vogelstein and coworkers [98]) working automatically on a massively rich dataset with hundreds of neurons with different firing rate and signal to noise ratio did not give satisfactory results, making it fail mainly with noisy neurons.

Finally, an approach viable but not yet tested for this dataset analysis is to take into account the spatial pattern taking place during coactivation events. In fact, what has already been observed is that the same brain area can show similar patterns frequently repeating themselves, sometimes in the form of waves. For this purpose, the analysis of the spatial pattern of the Ca^{2+} waves could be addressed.

The performed experiment showed the presence of spontaneous activity reflecting the tectal retinotopic map. Compact assemblies of neurons, grouped on a functional basis were found, and coactivation events with repetitive spatial and temporal patterns were observed. However, a reliable statistic on the temporal lag between neurons could not be done because of the long rise and decay time of the GCaMP5G. The use of a more rapid and sensitive marker, such as the one used by Grewe and coworkers [31] could be conveniently employed in such a fast imaging configuration, facilitating also a more proficient extraction of the neuronal spiking time through deconvolution. The 100 Hz-frame rate setup is currently being used to record 3D stacks of whole brain imaging, as the one described in Section 4.2.4.

4.3.2 Long-term recording for the study of neuronal patterns predictive of spontaneous behaviours

Behaviours do not solely occur as a consequence of sensory stimulations. Even in the absence of stimuli, the brain is capable of generating the so-called internally driven behaviours. The motivations can be various, spanning from hunger to fear. In zebrafish larvae, one of the most obvious spontaneous behaviours is navigation. The neuronal basis of spontaneous movements was first characterized in humans by a macroscopic increase in activity measured in premotor regions before the onset of spontaneous movements [86]. In the absence of external stimuli, a larva produces on average 80 tail bouts per hour. Understanding the neuronal mechanisms underlying internally driven behaviours in larvae requires recording for long periods of time both the neuronal activity preceding many spontaneous behaviours and the behaviour itself. Moreover, the study of the involvement of different brain circuits in the generation of internal decision requires monitoring the dynamics of different brain regions.

Here the following question was asked: is it possible to decode the brain circuitry and predict spontaneous movements of the larva before they take place? The one-photon DSLM was indeed used to monitor a large portions of the brain for hours. As stated in Paragraph 4.3.1, it is realistic that the continuous illumination with the blue laser did not triggered any sensory prompts.

As a pilot study, continuous acquisitions at 10 Hz on a single coronal section of 6 dpf-larva brain were performed for up to 6 h with little phototoxicity (see Figure 4.10(A)). Note that imaging for more time is not suggested since neurogenesis and plasticity can start to be significant, hence crosstalk between the ROIs could disturb the analysis. To reduce the data size, a 2x2 binning was used and a ROI of 800x900 pixels was recorded, resulting in around 300 GB size dataset per experiment. At the same time, the tail movements were monitored through a high-speed camera synchronized with the Orca Flash4.0, while the fish was illuminated through an IR led.

The average activity before the onset of spontaneous movements was indeed computed for each segmented ROI. A gradual build up in the activity starting 1.5 s before the onset of movements was detected, as shown in Figure 4.18(A). This time scale is in agreement with the readiness potential recorded in other species [26, 60]. However, this macroscopic observation was not sufficient to predict the onset of movements since spontaneous increase in the activity of a large portion of the neurons occurred also in the absence of movement.

A mass univariate Mann-Whitney test [28] on all ROIs was indeed performed

Chapter 4. Calcium Imaging in the Brain of Zebrafish Larva

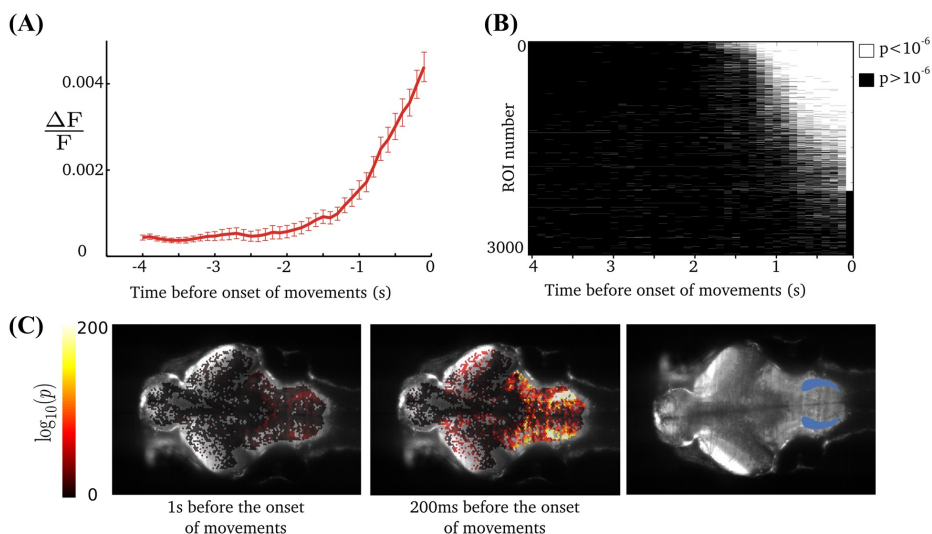


Figure 4.18: Increase in activity prior to spontaneous movement. (A) Average activity pooled over ROIs before the onset of tail movements. (B) Raster plot of the results of the Mann-Whitney test for each ROI, and for each frame before the onset of the movements; white stripes (black) indicate significant (non significant) differences with respect to the median activity of the inert regime; The ROIs are ordered according to their significance 100 ms before the onset. The most significant ROIs just before the onset of movement are also those that display a significant difference the earliest before a movement onset. (C) Left, centre: map of the decimal logarithm of the p -value for each ROI 1s and 200 ms before the onset of movements. Right: location of the neuropil region 3 of the rhombencephalon. This position matches the location of the most significant ROIs. Only movements spaced by a resting time of at least 8 s were considered ($N = 199$).

to find regions for which the activity was significantly higher before the onset of a spontaneous tail movement. An inert regime was defined by frames recorded at least 8 s before any movement. Every ROI in each 100 ms frame before the onset of a movement were then tested for differences from the inert regime. Some brain areas displayed a median activity statistically different from the inert regime 200 ms as well as 1 s before the onset of movements. Figure 4.18(C) shows a logarithmic map of the p -value of each ROI at different moments before the onset. On the right, the region with the strongest difference in activity between the preparation of spontaneous movements and the inert regime, the neuropil of the rhombencephalon, is coloured in blue. The

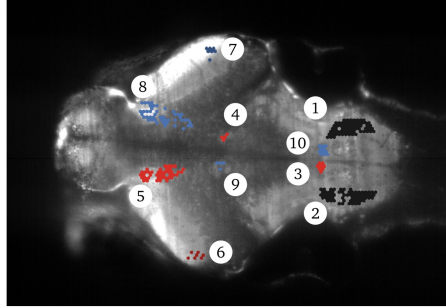


Figure 4.19: *Specificity for the directionality of routine turns. The red and blue colours correspond to grouping done with DLDA. The black group corresponds to the region with the most significant increase in activity before movements (Figure 4.18)(C)). Activity in regions 3 and 10 and in regions 4 and 9 displayed a phase opposition even in absence of spontaneous movements. The phase of the oscillator (i.e. the region that was active) right before the onset of a routine turn was predictive of its direction. Regions 1 and 2 and regions 6 and 7 did not exhibit significant differences between directions of movement. For regions 5 and 8, if the red (blue) side was strongly active the tail movements were likely to be routine turns with positive (negative) deflection.*

neurons capable of predicting the tail movements well in advance (1s before the onset of the movement) were those showing the most significant increase just before the onset of movements. This is depicted in Figure 4.18)(B), where the results of the Mann-Whitney test for each ROI are ordered according to their significance right before the onset. Hence, by looking at the brain activity 1 s before the onset of the movement, we can predict already that the larva is going to move.

These preliminary results validate the whole experimental and analytical methodology. Further and more sophisticated analysis will be performed by direct linear discrimination analysis (DLDA) [44] to predict the direction of tail movements from neuronal activity. It was already possible to distinguish between left and right tail movements during a specific class of turns (routine turn) [40]. The map of significant ROIs is shown in Figure 4.19, where blue and red dots represent areas active in the movements with opposite direction. It presents a bilateral anti-symmetric pattern in several brain regions, some of which displayed oscillations with phase opposition [2], even in absence of spontaneous movements, others activated every time a movement was going to

Chapter 4. Calcium Imaging in the Brain of Zebrafish Larva

happen. Indeed, by looking at the activations of these areas, it has been possible to predict the direction of the tail movement. This analysis is being carried on for all the class of movements (c-bend, scoot, burst etc.).

Given the timing of motor preparation in the order of seconds, brain-wide 3D recordings at higher temporal sampling (typically a complete 200 μm stack at 3 Hz) could accelerate the discovery of relevant anatomical structures involved in internal decisions. Moreover, this could help to integrate the analysis also for other type of tail movements, possibly due to activity in brain regions not included in the plane that was here discussed. A potential pitfall could be that larvae do not move the tail spontaneously but as the result of the feedback of agarose resulting from an attempt to move the eye. Moreover, a two-photon DSLM would give the certainty not to affect the spontaneous behaviour of the larva by not shining visible light on the sample.

4.3.3 Two-photon excitation for visual stimulation analysis

To figure out how the whole network of neurons works, it remains of vital importance to understand how sensory inputs are processed. This necessitates to record neuron activity on the large scale in behaving animals. A typical behaviour linked to the activation of different brain areas is the visuomotor behaviour, which can be assessed in the zebrafish larva by applying visual stimulation. As an example, swimming can be elicited by the presentation of a grating pattern moving from the tail to the head below a restrained larva. Moving the grating in different directions leads to different behaviours. Direction selectivity is in fact an important feature of the visual system, but little is known about how it is encoded in the brain. Light sheet fluorescence microscopy could be useful for elucidating this brain-wide optomotor response. However, visual evocation is probably the most challenging stimulation to be address by LSFM, because of the illumination geometry. Whether visible excitation of the one-photon DSLM stimulates photoreceptors or other photosensitive cells has been the subject of debate in the neuroscience community, because of adaption capability of the brain. While likely this is not an issue for spontaneous activity, in a recent study from Wolf and coworkers [102] it has been shown that potential problems arise from visible illumination during the study of visually driven activity. They suggested instead that near infrared excitation through two-photon DSLM would be more suitable for behavioural neuroscience.

For this purpose, the two-photon DSLM system was used to capture brain ac-

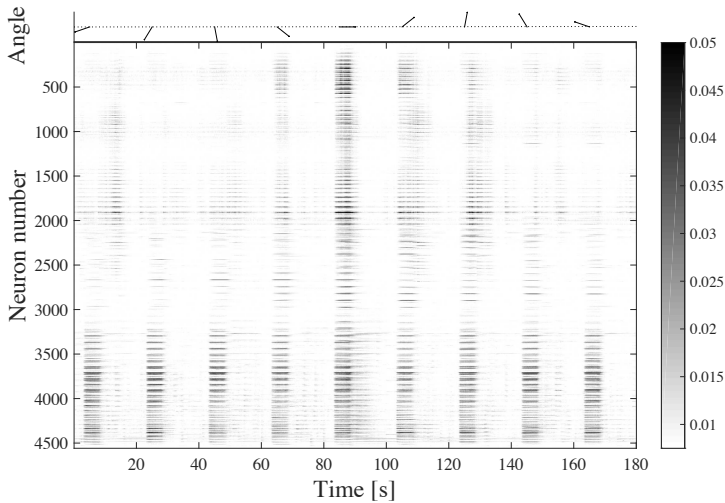


Figure 4.20: Raster plot of visually evoked activity. The fluorescence traces were averaged across trials. Every 20 s the grid presented to the sample, whose orientation is shown in the first row of the graph, was rotated of 40° .

tivity during visuomotor behaviour. A single plane of 800×900 pixels was recorded at 10 Hz for 30 minutes with binning 2×2 , while a visual stimulation was performed on the screen below the sample. This consisted in a grid of dark bars moving in 9 directions: the moving bars were presented for 5 s and after 15 s of rest they were sequentially rotated by 40% . The 9 stimulations were repeated for 10 times. This stimulus application has the effect of making the fish fictively navigate along with the direction of movement.

Segmentation by hexagon overlay was done, and the extracted curves after averaging across trials can be seen in raster plot in Figure 4.20. To evaluate the direction selectivity, the responses were integrated in a 15 s time window right after the stimulation, and an average response to the different grid orientations was evaluated through directional statistics, as previously described by Ringach and coworkers for the macaque [77] and by Montijn and coworker for the mouse visual cortex [58]. The circular variance was evaluated in order to have single number for each orientation-tuning curve that measures the degree of selectivity of a ROI. Each ROI was colour coded on the reference image with the hsv colour model, in which the *hue* is the angle of the grid to which the ROI was mainly responsive, the *saturation* corresponds to the circular variance and the *value* codes the intensity of response. The resulting map is shown

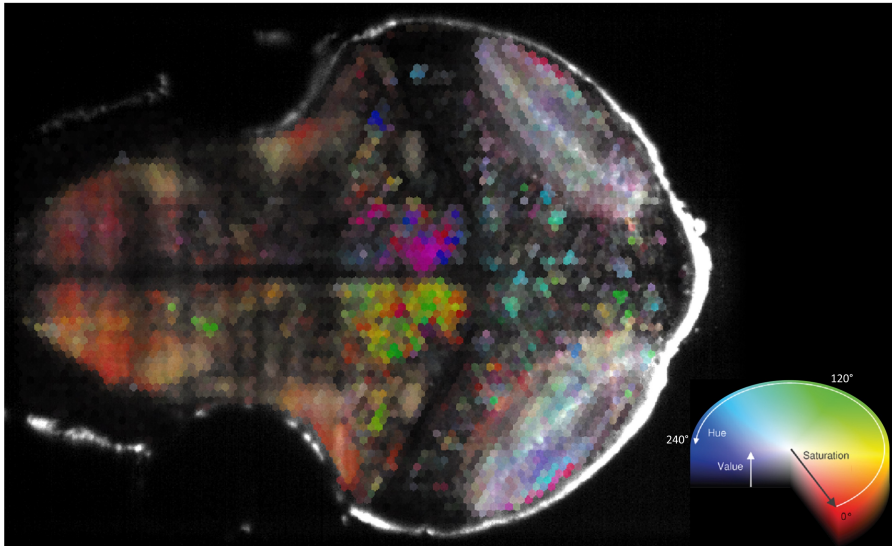


Figure 4.21: *Orientation selectivity map. Each ROI was colour coded on the reference image with the hsv colour model, in which the hue is the angle of the grid to which the ROI was mainly responsive, the saturation corresponds to the circular variance and the value codes the intensity of response. ROIs with saturated colours reflect areas with high orientation selectivity.*

in Figure 4.21. Black ROIs correspond to areas that were not activated by the stimulus; the white ROIs correspond to areas activated by the stimulus, but insensitive to the orientation of the grid; vibrant colours correspond instead to areas responding significantly only to specific grid orientations.

The neuropil of the optic tectum is almost always active during visual stimulation, although few details emerge: two areas on the external part of the neuropil have a saturated hue, and are symmetric on the two brain sides. One of the two encodes the selectivity to forward orientation (red), while the other one shows a preference for the backward stimulation (light blue). This opposite selectivity is clearer when considering the graphs of the response of single ROIs, like those selected in Figure 4.22(C). The graphs are reported in Figure 4.22(A), where the first and second one show the responses of the the left tectum, while the third and fourth correspond to the responses of the right tectum. The red and light blue curves are indeed active during opposite stimulation, and the same behaviour is present in both hemispheres. A morphological explanation of these two patterns is that they lay in two different layers, or lamina, of the tectum,

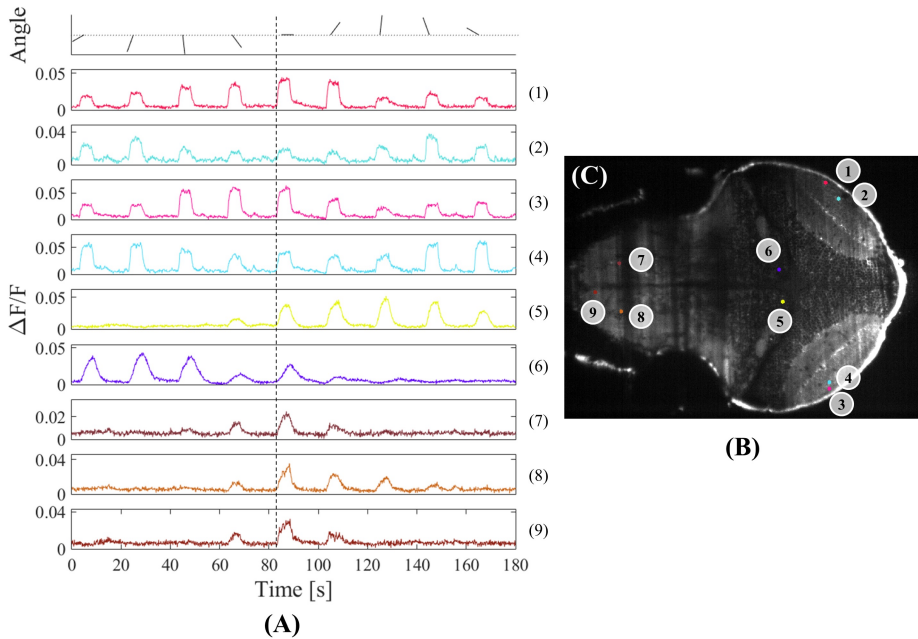


Figure 4.22: Orientation selectivity graphs. Single ROIs were selected (B) and their signal plotted after average over trials (A). The first row displays the angular orientation of the grid, from -160° to 160° . The dashed line highlights the promptness of response of the optic tectum neuropil (1,2,3,4) compared to all the others.

where different dendrite/axons of retinal ganglion cells arborize. This is something in agreement with similar results previously reported [65].

In the somata of the tectum, direction selectivity is not spatially clustered in ensembles of activation, but shows a pattern that can be referred to as “salt and pepper”, where small groups of neurons with different selectivity scattered all over the tectum can be found.

More straightforward is instead the outcome in the hindbrain. A clear left-right lateralization appears, with the left (right) hindbrain associated with a grid moving toward the right (left) direction, which is known to make the fish try to swim to the left (right). This segregation of activity during optomotor behaviour can be found in three areas per hindbrain side in the imaged plane, coloured in purple and yellow. The opposite selectivity is obvious when considering the graphs of the response of single ROIs, reported in Figure 4.22(A.5) and (A.6), where the yellow and the purple curves correspond to these selective areas from the hindbrain: when one is active, the other one is not.

Chapter 4. Calcium Imaging in the Brain of Zebrafish Larva

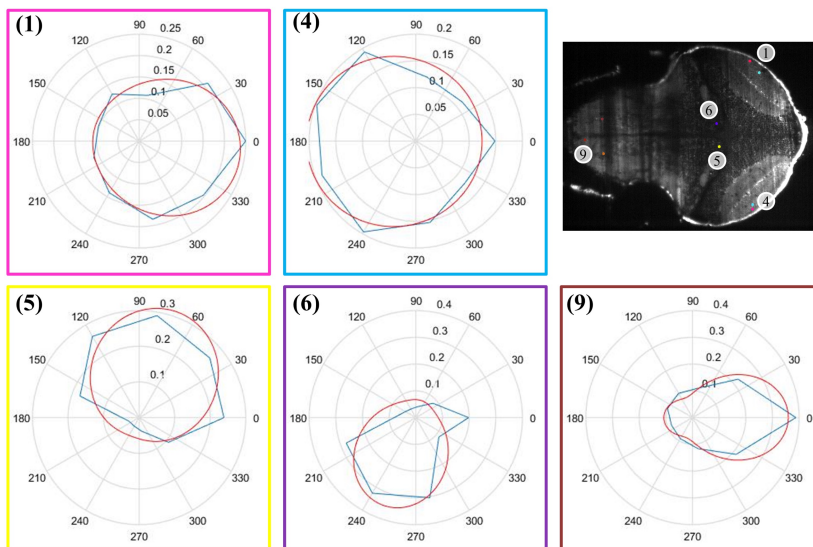


Figure 4.23: Polar plots of orientation selectivity. The number next to the plots corresponds the graphs in Figure 4.22(A). The red curves are the result of a von Mises fit [58], elucidating the preferential orientation to which specific ROIs respond.

The hindbrain neuropil, instead, is sensitive to all the forward movements. This makes sense, since it innervates toward the spinal cord, generating the actual tail movements. It does not react when backward movement (see last three graphs in Figure 4.22(A)).

The orientation selectivity for the highlighted ROIs is summarised in Figure 4.23, where polar plots of some of the selected ROIs show the preferential orientation of the stimulus to which a ROI responds. The preferential orientation is highlighted by the red curve, result of a von Mises fit [58]. Finally, from a temporal point of view, it can be observed from Figure 4.22(A) that the optic tectum shows a step-like response function and is obviously more prompt to respond to the stimulus, while the rest of the brain undergoes a slower build-up in the activity (see dashed line).

From these data it can be hypothesised that the sensory area for direction selectivity is located in the external layers of the neuropil of the optic tectum, where the signal arrives directly from the retina. The neuropil is of course a sensory area, but it appears to be already the first relay of motion processing. The signal is then sent to the somata, without specific spatial selectivity, but in a salt and pepper way. However, few agglomerates of selective neurons can be

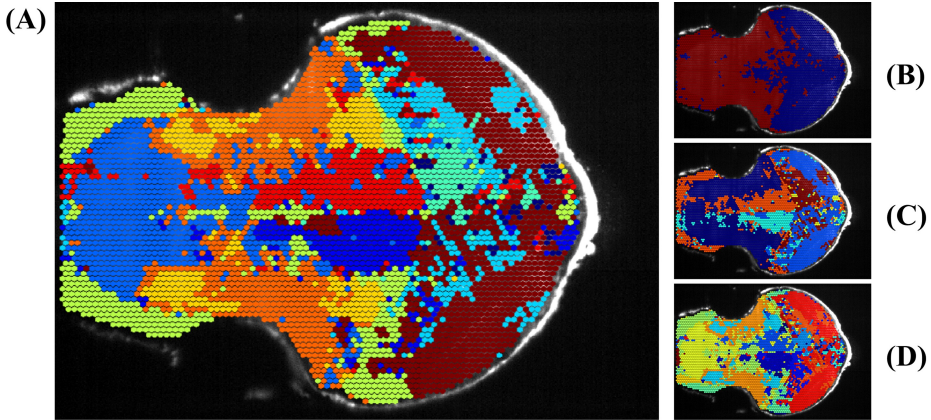


Figure 4.24: Clusterization of the activity with K-means algorithm. (A) shows the clusterization with the optimal number of K (10). With $K = 2$ (B) good separation between the optic tectum and the motor area is provided. (C) and (D) display the clusterization with $K = 6$ and $K = 16$, respectively, and show the same main clusters as (A) as a sign of robustness.

still recognised. Unexpectedly, these groups are mainly selective for backward movements, which are then inhibited in the rest of the brain. The meaningful information for a motor response is then processed by the hindbrain in a lateralized way, and finally transformed in a motor behaviour by the back part of the hindbrain and by the spinal cord.

The performed analysis considers each neurons independently from the others, while a population analysis of covariance could give more insights on the optomotor circuitry. As a first attempt to take into account relationships between neurons, clustering with K-means based on correlation distance was implemented [54]. The most suitable number K of clusters was found by computing a sweep in K space between 1 and 20, and inspecting their silhouette plot. The best match was found to be $K = 10$. Figure 4.24 displays the topographical layout of the obtained clusters, which shows the presence of areas with correlated activity actually corresponding to different functional regions. It is possible to recognize the lateralization in the hindbrain as the main asymmetry in the optomotor response; moreover, the neuropile of this area is divided into different clusters, which are indeed responsive to the same orientation of the grid but with different promptness. The most relevant neuronal clusters proved robust with respect to change in K (see Figure 4.24(C) and (D)), while Figure 4.24(B) show the clusterisation in motor and visual areas obtained with

Chapter 4. Calcium Imaging in the Brain of Zebrafish Larva

$K = 2$.

Although the two-photon DSLM proved suitable to study visual stimulation without artifacts induced by the laser illumination, few issues have still to be solved. On top of all, pigmentation of the larvae skin and retina strongly absorbs the high peak intensity of the laser and, if illuminated with the focalized IR beam, it immediately undergoes ablation. Especially for the eyes, this is unacceptable, since cavitation bubbles can form, hurting or even killing the larva. Melanization inhibitors could be used to avoid the pigments, but obviously this is not viable if performing experiments on visually evoked behaviours. This means that three-dimensional imaging must be limited to the upper part of the brain. Alternatively, a scanning pattern for the light sheet that excludes the eyes, as the one presented by Vladimirov and coworkers [97], could be performed, although difficult to adapt for differently mounted samples.

Another issue is the possible heating of the fish during illumination, which could generate stress on the larva as well as thermal effects on the brain. After 1 hour, the brain starts suffering from the continuous excitation, therefore for long term imaging, illumination only during salient visuomotor responses should be recommended. Hence, to avoid the sample stress, the power of the laser cannot be raised arbitrarily to increase the signal to noise ratio. This limits also the frequency of acquisition, that, with the current GCaMP5G indicator, was set at 10 Hz. Because of the 1:8 contrast of the signal in the Rayleigh length of the focused gaussian beam, the central part of the brain is subjected to higher stress. A possible solution for this problem is the use of two-sided illumination, which would extend the field of view and allow one to reduce the laser power.

4.4 Conclusions

It has been validated that light sheet fluorescence microscopy is a useful tool for calcium imaging in the neuroscience field. It gives the possibility to study both the spontaneous and evoked activity from a large fraction of the zebrafish brain with single cell resolution and with less damage respect to all other techniques. A one-photon DSLM was implemented and exploited for spontaneous activity acquisitions. Thanks to the recording at high frame-rate, it was possible to build a pipeline for imaging with temporal resolution that allowed us to see small temporal differences during events usually considered simultaneous, and to appreciate their temporal and spatial features. Although a reliable statis-

tical analysis is still in progress, this opens the opportunity for the observation of soloists and choristers in the zebrafish tectum. Together with a faster and more sensitive calcium probe, it will be possible to record thousands of neurons with near-millisecond time resolution, uncovering emergent properties of neuronal circuits that can only be studied at high temporal resolution in large network. The same system has been successfully used for behavioural studies of neuronal patterns predictive of spontaneous behaviours, in which the long-term acquisition resulted essential for consistent recording of spontaneous tail movements. It has indeed been possible to identify brain regions predictive of the direction of routine tours, displaying a build-up in the activity around 1 s before the onset of the spontaneous tail movement. Moreover, even during resting time, some brain regions showed oscillations in the activity with a bilateral anti-symmetric pattern over a long time scale (~ 10 s) with the level of activity prior to the onset of tail movements predictive of the turn direction. A possible improvement is freeing the eyes of the larva and monitor also their movements. Another interesting possible application of long term recording could be monitoring neurogenesis and how new born neurons become part of the neural circuitry. For the study of sensory driven brain activity, a two-photon illumination path was added to the DSLM. The use of the IR excitation is important for not compromising the visual perception of the zebrafish larvae during visual stimulation. A moving grid was presented on a screen below the larva, inducing optomotor responses that were monitored along a whole section of the brain. Brain areas responsible of orientation selectivity were identified, as well as motor areas directly translating the stimuli into motor responses. Although correlated regions were identified through k-means algorithm, a more complex analysis taking into account the neuronal covariance could extract more information from a so rich dataset. Another possible application where IR excitation would be imperative is the study of the zebrafish sleep, although hours of recording with the two-photon excitation seems difficult because of heating and photobleaching issues.

From a technical point, what could be interesting to implement is a second light path at 90° with respect to the first one, illuminating the larva in between the eyes. This would allow us to observe the whole brain with no shadows casted by the strongly absorbing pigments of the retinas. Also, 3D recordings should be recommended to fully exploit the light sheet ability to record quickly. By the way, for two-photon measurement the laser must be switched off when arriving around the eyes areas. About the big data issue, a way to be able to save as much data as possible is to parallelize the saving of the data on different hard

Chapter 4. Calcium Imaging in the Brain of Zebrafish Larva

disk, or, especially for evoked activity studies, exploiting the on-board memory of new cameras to acquire few frames, compare them with a reference from time to time and save the buffered frames only if variations in the fluorescence happens and discard them otherwise in order to reduce the dataset dimensions.

Bibliography

- [1] Misha B. Ahrens and Florian Engert. Large-scale imaging in small brains. *Current Opinion in Neurobiology*, 32:78–86, 2015.
- [2] Misha B Ahrens, Michael B Orger, Drew N Robson, Jennifer M Li, and Philipp J Keller. Whole-brain functional imaging at cellular resolution using light-sheet microscopy. *Nat Methods*, 10(5):413–420, 2013.
- [3] Jasper Akerboom, Tsai-Wen Chen, Trevor J. Wardill, Lin Tian, Jonathan S. Marvin, Sevinç Mutlu, Nicole Carreras Caldéron, Federico Esposti, Bart G. Borghuis, Xiaonan Richard Sun, Andrew Gordus, Michael B. Orger, Ruben Portugues, Florian Engert, John J. Macklin, Alessandro Filosa, Aman Aggarwal, Rex A. Kerr, Ryousuke Takagi, Sebastian Kracun, Eiji Shigetomi, Baljit S. Khakh, Herwig Baier, Leon Lagnado, Samuel S.-H. Wang, Cornelia I. Bargmann, Bruce E. Kimmel, Vivek Jayaraman, Karel Svoboda, Douglas S. Kim, Eric R. Schreiter, and Loren L. Looger. Optimization of a GCaMP Calcium Indicator for Neural Activity Imaging. *The Journal of Neuroscience*, 32(40):13819–13840, 2012.
- [4] G J Allen, J M Kwak, S P Chu, J Llopis, R Y Tsien, J F Harper, and J I Schroeder. Cameleon calcium indicator reports cytoplasmic calcium dynamics in Arabidopsis guard cells. *The Plant journal : for cell and molecular biology*, 19(6):735–47, sep 1999.
- [5] Arabidopsis Genome Initiative. Analysis of the genome sequence of the flowering plant Arabidopsis thaliana. *Nature*, 408(6814):796–815, 2000.
- [6] G S Baird, D a Zacharias, and R Y Tsien. Circular permutation and receptor insertion within green fluorescent proteins. *Proceedings of the National Academy of Sciences*, 96(20):11241–11246, sep 1999.

Bibliography

- [7] L. R. Band, D. M. Wells, a. Larrieu, J. Sun, a. M. Middleton, a. P. French, G. Brunoud, E. M. Sato, M. H. Wilson, B. Peret, M. Oliva, R. Swarup, I. Sairanen, G. Parry, K. Ljung, T. Beeckman, J. M. Garibaldi, M. Estelle, M. R. Owen, K. Vissenberg, T. C. Hodgman, T. P. Pridmore, J. R. King, T. Vernoux, and M. J. Bennett. Root gravitropism is regulated by a transient lateral auxin gradient controlled by a tipping-point mechanism. *Proceedings of the National Academy of Sciences*, 109(12):4668–4673, 2012.
- [8] K. Becker, N. Jährling, E. R. Kramer, F. Schnorrer, and H. U. Dodt. Ultramicroscopy: 3D reconstruction of large microscopical specimens. *Journal of Biophotonics*, 1(1):36–42, 2008.
- [9] Michael J Berridge, Peter Lipp, and Martin D Bootman. The versatility and universality of calcium signalling. *Nature Reviews Molecular Cell Biology*, 1(1):11–21, oct 2000.
- [10] Eric Betzig, George H Patterson, Rachid Sougrat, O Wolf Lindwasser, Scott Olenych, Juan S Bonifacino, Michael W Davidson, Jennifer Lippincott-Schwartz, and Harald F Hess. Imaging intracellular fluorescent proteins at nanometer resolution. *Science (New York, N.Y.)*, 313(5793):1642–5, sep 2006.
- [11] Jörg Bewersdorf, Rainer Pick, and Stefan W. Hell. Multifocal multiphoton microscopy. *Optics Letters*, 23(9):655, may 1998.
- [12] Tobias Breuninger, Klaus Greger, and Ernst H K Stelzer. Lateral modulation boosts image quality in single plane illumination fluorescence microscopy. *Optics letters*, 32(13):1938–1940, 2007.
- [13] György Buzsáki. Large-scale recording of neuronal ensembles. *Nature neuroscience*, 7(5):446–451, 2004.
- [14] Jianhua Cang and David A Feldheim. Developmental Mechanisms of Topographic Map Formation and Alignment. *Annu. Rev. Neurosci*, 36:51–77, 2013.
- [15] R Maynard Case, David Eisner, Alison Gurney, Owen Jones, Shmuel Muallem, and Alexei Verkhratsky. Evolution of calcium homeostasis: from birth of the first cell to an omnipresent signalling system. *Cell calcium*, 42(4-5):345–50, jan 2007.
- [16] Alex Costa, Alessia Candeo, Luca Fieramonti, Gianluca Valentini, and Andrea Bassi. Calcium Dynamics in Root Cells of *Arabidopsis thaliana* Visualized with Selective Plane Illumination Microscopy. *PLoS ONE*, 8(10), 2013.
- [17] Irene Costantini, Jean-Pierre Ghobril, Antonino Paolo Di Giovanna, Anna Letizia Allegra Mascaro, Ludovico Silvestri, Marie Caroline Müllenbroich, Leonardo Onofri, Valerio Conti, Francesco Vanzi, Leonardo Sacconi, Renzo Guerrini, Henry Markram, Giulio Iannello, and Francesco Saverio Pavone. A versatile clearing agent for multi-modal brain imaging. *Scientific reports*, 5:9808, jan 2015.
- [18] W Denk, J. Strickler, and W. Webb. Two-photon laser scanning fluorescence microscopy. *Science*, 248(4951):73–76, apr 1990.

- [19] Antony N Dodd, Mia Kyed Jakobsen, Andrew J Baker, Anja Telzerow, Sui-Wen Hou, Laurent Laplace, Laure Barrot, R Scott Poethig, Jim Haseloff, and Alex A R Webb. Time of day modulates low-temperature Ca signals in Arabidopsis. *The Plant journal : for cell and molecular biology*, 48(6):962–73, dec 2006.
- [20] Antony N Dodd, Jörg Kudla, and Dale Sanders. The language of calcium signaling. *Annual review of plant biology*, 61:593–620, jan 2010.
- [21] Hans-Ulrich Dodt, Ulrich Leischner, Anja Schierloh, Nina Jährling, Christoph Peter Mauch, Katrin Deininger, Jan Michael Deussing, Matthias Eder, Walter Zieglgänsberger, and Klaus Becker. Ultramicroscopy: three-dimensional visualization of neuronal networks in the whole mouse brain. *Nature methods*, 4(4):331–336, 2007.
- [22] Christoph J Engelbrecht and Ernst H Stelzer. Resolution enhancement in a light-sheet-based microscope (SPIM). *Optics letters*, 31(10):1477–1479, 2006.
- [23] Florian O Fahrbach, Vasily Gurchenkov, Kevin Alessandri, Pierre Nassoy, and Alexander Rohrbach. Light-sheet microscopy in thick media using scanned Bessel beams and two-photon fluorescence excitation. *Optics express*, 21(11):13824, 2013.
- [24] FO. Fahrbach, P Simon, and A Rohrbach. Microscopy with self-reconstructing beams. *Nature Photonics*, 4(11):780–785, 2010.
- [25] Joseph R Fetcho. Neuroscience: Crystal-clear brains. *Nature*, 485(7399):453–5, may 2012.
- [26] Itzhak Fried, Roy Mukamel, and Gabriel Kreiman. Internally Generated Preactivation of Single Neurons in Human Medial Frontal Cortex Predicts Volition. *Neuron*, 69(3):548–562, 2011.
- [27] Mike Friedrich, Qiang Gan, Vladimir Ermolayev, and Gregory S Harms. STED-SPIM: Stimulated emission depletion improves sheet illumination microscopy resolution. *Biophysical journal*, 100(8):L43–5, apr 2011.
- [28] K. J. Friston, a. P. Holmes, K. J. Worsley, J.-P. Poline, C. D. Frith, and R. S. J. Frackowiak. Statistical parametric maps in functional imaging: A general linear approach. *Human Brain Mapping*, 2(4):189–210, 1995.
- [29] Werner Göbel and F Helmchen. In Vivo Calcium Imaging of Neural Network Function. *Physiology*, 22(51):358–365, dec 2007.
- [30] K. Greger, J. Swoger, and E. H K Stelzer. Basic building units and properties of a fluorescence single plane illumination microscope. *Review of Scientific Instruments*, 78(2), 2007.
- [31] B Grewe, D Langer, H Kasper, Bjorn M Kampa, and Fritjof Helmchen. High-speed in vivo calcium imaging reveals neuronal network activity with near-millisecond precision. *Nature Methods*, 7(5):399–405, 2010.
- [32] Christine Grienberger and Arthur Konnerth. Imaging calcium in neurons. *Neuron*, 73(5):862–85, mar 2012.

Bibliography

- [33] Stefan W. Hell and Jan Wichmann. Breaking the diffraction resolution limit by stimulated emission: stimulated-emission-depletion fluorescence microscopy. *Optics Letters*, 19(11):780, jun 1994.
- [34] Alan E. Hendrickson and Paul Owen White. PROMAX: A QUICK METHOD FOR ROTATION TO OBLIQUE SIMPLE STRUCTURE. *British Journal of Statistical Psychology*, 17(1):65–70, may 1964.
- [35] Samuel T Hess, Thanu P K Girirajan, and Michael D Mason. Ultra-high resolution imaging by fluorescence photoactivation localization microscopy. *Biophysical journal*, 91(11):4258–72, dec 2006.
- [36] D H Hubel. Tungsten microelectrode for recording from single units. *Science*, 125(3247):549–550, 1957.
- [37] Jan Huisken and Didier Y R Stainier. Even fluorescence excitation by multidirectional selective plane illumination microscopy (mSPIM). *Optics letters*, 32(17):2608–2610, 2007.
- [38] Jan Huisken, Jim Swoger, Filippo Del Bene, Joachim Wittbrodt, and Ernst H K Stelzer. Optical Sectioning Deep Inside Live Embryos by Selective Plane Illumination Microscopy. *Science*, 305(August):1007–1009, 2004.
- [39] Raphael Jorand, Gwénaële Le Corre, Jordi Andilla, Amina Maandhui, Céline Frongia, Valérie Lobjois, Bernard Ducommun, and Corinne Lorenzo. Deep and clear optical imaging of thick inhomogeneous samples. *PLoS one*, 7(4):e35795, 2012.
- [40] Adrien Jouary. Comportement moteur induit visuellement et spontané chez la larve du poisson zèbre. 2015.
- [41] F.S. Kao and Teng-ming Chen. A study on the luminescent properties of new green-emitting terbium-activated $\text{CaIn}_2\text{O}_4:\text{xTb}$ phosphors. *Journal of Luminescence*, 96(2-4):261–267, mar 2002.
- [42] Philipp J Keller, Annette D Schmidt, Anthony Santella, Khaled Khairy, Zhirong Bao, Joachim Wittbrodt, and Ernst H K Stelzer. Fast, high-contrast imaging of animal development with scanned light sheet-based structured-illumination microscopy. *Nature methods*, 7(8):637–642, 2010.
- [43] Philipp J Keller, Annette D Schmidt, Joachim Wittbrodt, and Ernst H K Stelzer. Reconstruction of zebrafish early embryonic development by scanned light sheet microscopy. *Science (New York, N.Y.)*, 322(5904):1065–1069, 2008.
- [44] J. Kittler and K. Messer. A new direct LDA (D-LDA) algorithm for feature extraction in face recognition. In *Proceedings of the 17th International Conference on Pattern Recognition, 2004. ICPR 2004.*, pages 545–548 Vol.4. IEEE, aug 2004.
- [45] M R Knight, A K Campbell, S M Smith, and A J Trewavas. Transgenic plant aequorin reports the effects of touch and cold-shock and elicitors on cytoplasmic calcium. *Nature*, 352(6335):524–6, aug 1991.

- [46] Melanie Krebs, Katrin Held, Andreas Binder, Kenji Hashimoto, Griet Den Herder, Martin Parniske, Jörg Kudla, and Karin Schumacher. FRET-based genetically encoded sensors allow high-resolution live cell imaging of Ca²⁺ dynamics. *The Plant Journal*, 69(1):181–192, jan 2012.
- [47] Uros Krzic, Stefan Gunther, Timothy E Saunders, Sebastian J Streichan, and Lars Hufnagel. Multiview light-sheet microscope for rapid in toto imaging. *Nature Methods*, 9(7):730–733, 2012.
- [48] Jörg Kudla, Oliver Batistic, and Kenji Hashimoto. Calcium signals: the lead currency of plant information processing. *The Plant cell*, 22(3):541–63, mar 2010.
- [49] Joseph R. Lakowicz, editor. *Principles of Fluorescence Spectroscopy*. Springer US, Boston, MA, 2006.
- [50] H M Lam, J Chiu, M H Hsieh, L Meisel, I C Oliveira, M Shin, and G Coruzzi. Glutamate-receptor genes in plants. *Nature*, 396(6707):125–6, nov 1998.
- [51] Loren L. Looger and Oliver Griesbeck. Genetically encoded neural activity indicators. *Current Opinion in Neurobiology*, 22(1):18–23, 2012.
- [52] Vítor Lopes-dos Santos, Sergio Conde-Ocazonez, Miguel A L Nicolelis, Sidarta T. Ribeiro, and Adriano B L Tort. Neuronal Assembly Detection and Cell Membership Specification by Principal Component Analysis. *PLoS ONE*, 6(6):e20996, jun 2011.
- [53] Giovanna Loro, Ilaria Drago, Tullio Pozzan, Fiorella Lo Schiavo, Michela Zottini, and Alex Costa. Targeting of Cameleons to various subcellular compartments reveals a strict cytoplasmic/mitochondrial Ca²⁺ handling relationship in plant cells. *The Plant journal : for cell and molecular biology*, 71(1):1–13, jul 2012.
- [54] J. MacQueen. Some methods for classification and analysis of multivariate observations. In *Proceedings of the Fifth Berkeley Symposium on Mathematical Statistics and Probability, Volume 1: Statistics*. The Regents of the University of California, 1967.
- [55] Alexis Maizel, Daniel von Wangenheim, Fernán Federici, Jim Haseloff, and Ernst H K Stelzer. High-resolution live imaging of plant growth in near physiological bright conditions using light sheet fluorescence microscopy. *The Plant journal : for cell and molecular biology*, 68(2):377–85, oct 2011.
- [56] a Miyawaki, J Llopis, R Heim, J M McCaffery, J a Adams, M Ikura, and R Y Tsien. Fluorescent indicators for Ca²⁺ based on green fluorescent proteins and calmodulin. *Nature*, 388(6645):882–887, 1997.
- [57] Gabriele B Monshausen, Mark A Messerli, and Simon Gilroy. Imaging of the Yellow Cameleon 3.6 indicator reveals that elevations in cytosolic Ca²⁺ follow oscillating increases in growth in root hairs of Arabidopsis. *Plant physiology*, 147(4):1690–8, aug 2008.
- [58] Jorrit S Montijn, Martin Vinck, and Cyriel M A Pennartz. Population coding in mouse visual cortex: response reliability and dissociability of stimulus tuning and noise correlation. *Frontiers in computational neuroscience*, 8:58, jan 2014.

Bibliography

- [59] H Morise, O Shimomura, F H Johnson, and J Winant. Intermolecular energy transfer in the bioluminescent system of *Aequorea*. *Biochemistry*, 13(12):2656–62, jun 1974.
- [60] Yoshiko Murakami, Hasan Tawamie, Yusuke Maeda, Christian Buttner, Rebecca Buchert, Farah Radwan, Stefanie Schaffer, Heinrich Sticht, Michael Aigner, André Reis, Taroh Kinoshita, and Rami Abou Jamra. Null Mutation in PGAP1 Impairing Gpi-Anchor Maturation in Patients with Intellectual Disability and Encephalopathy. *PLoS Genetics*, 10(5):e1004320, may 2014.
- [61] Toshio Murashige and Folke Skoog. A Revised Medium for Rapid Growth and Bio Assays with Tobacco Tissue Cultures. *Physiologia Plantarum*, 15(3):473–497, jul 1962.
- [62] T Nagai, A Sawano, E S Park, and A Miyawaki. Circularly permuted green fluorescent proteins engineered to sense Ca²⁺. *Proceedings of the National Academy of Sciences*, 98(6):3197–3202, mar 2001.
- [63] Takeharu Nagai, Shuichi Yamada, Takashi Tominaga, Michinori Ichikawa, and Atsushi Miyawaki. Expanded dynamic range of fluorescent indicators for Ca²⁺ by circularly permuted yellow fluorescent proteins. *Proceedings of the National Academy of Sciences*, 101(29):10554–10559, jul 2004.
- [64] J Nakai, M Ohkura, and K Imoto. A high signal-to-noise Ca(2+) probe composed of a single green fluorescent protein. *Nature biotechnology*, 19(2):137–41, 2001.
- [65] Nikolas Nikolaou, Andrew S. Lowe, Alison S. Walker, Fatima Abbas, Paul R. Hunter, Ian D. Thompson, and Martin P. Meyer. Parametric Functional Maps of Visual Inputs to the Tectum. *Neuron*, 76(2):317–324, oct 2012.
- [66] S. Ogawa, T. M. Lee, A. R. Kay, and D. W. Tank. Brain magnetic resonance imaging with contrast dependent on blood oxygenation. *Proceedings of the National Academy of Sciences*, 87(24):9868–9872, dec 1990.
- [67] Michael Okun, Nicholas A. Steinmetz, Lee Cossell, M. Florencia Iacaruso, Ho Ko, Péter Barthó, Tirin Moore, Sonja B. Hofer, Thomas D. Mrsic-Flogel, Matteo Carandini, and Kenneth D. Harris. Diverse coupling of neurons to populations in sensory cortex. *Nature*, 521(7553):511–515, apr 2015.
- [68] P O’Shea, M Kimmel, X Gu, and R Trebino. Highly simplified device for ultrashort-pulse measurement. *Optics letters*, 26(12):932–934, 2001.
- [69] Jonathan Palero, Susana I C O Santos, David Artigas, and Pablo Loza-Alvarez. A simple scanless two-photon fluorescence microscope using selective plane illumination. *Optics express*, 18(8):8491–8, apr 2010.
- [70] Thomas Panier, Sebastián A Romano, Raphaël Olive, Thomas Pietri, Germán Sumbre, Raphaël Candelier, and Georges Debrégeas. Fast functional imaging of multiple brain regions in intact zebrafish larvae using selective plane illumination microscopy. *Frontiers in neural circuits*, 7(April):65, 2013.

- [71] Adrien Peyrache, Karim Benchenane, Mehdi Khamassi, Sidney I. Wiener, and Francesco P. Battaglia. Principal component analysis of ensemble recordings reveals cell assemblies at high temporal resolution. *Journal of Computational Neuroscience*, 29(1-2):309–325, 2010.
- [72] Christoph Plieth. Signal percolation through plants and the shape of the calcium signature. *Plant signaling & behavior*, 5(4):379–385, 2010.
- [73] Michelle Beth Price, John Jelesko, and Sakiko Okumoto. Glutamate receptor homologs in plants: functions and evolutionary origins. *Frontiers in plant science*, 3:235, jan 2012.
- [74] Zhi Qi, Nicholas R Stephens, and Edgar P Spalding. Calcium entry mediated by GLR3.3, an Arabidopsis glutamate receptor with a broad agonist profile. *Plant physiology*, 142(3):963–71, nov 2006.
- [75] Magaly Rincón-Zachary, Neal D Teaster, J Alan Sparks, Aline H Valster, Christy M Motes, and Elison B Blancaflor. Fluorescence resonance energy transfer-sensitized emission of yellow cameleon 3.60 reveals root zone-specific calcium signatures in Arabidopsis in response to aluminum and other trivalent cations. *Plant physiology*, 152(3):1442–58, mar 2010.
- [76] Dario L. Ringach. Spontaneous and driven cortical activity: implications for computation. *Current Opinion in Neurobiology*, 19(4):439–444, 2009.
- [77] Dario L. Ringach, Robert M. Shapley, and Michael J. Hawken. Orientation Selectivity in Macaque V1: Diversity and Laminar Dependence. *J. Neurosci.*, 22(13):5639–5651, jul 2002.
- [78] Sebastián A. Romano, Thomas Pietri, Verónica Pérez-Schuster, Adrien Jouary, Mathieu Haudrechy, and Germán Sumbre. Spontaneous neuronal network dynamics reveal circuit s functional adaptations for behavior. *Neuron*, 85(5):1070–1085, 2015.
- [79] V A Romoser, P M Hinkle, and A Persechini. Detection in living cells of Ca²⁺-dependent changes in the fluorescence emission of an indicator composed of two green fluorescent protein variants linked by a calmodulin-binding sequence. A new class of fluorescent indicators. *The Journal of biological chemistry*, 272(20):13270–4, may 1997.
- [80] Rüdiger Rudolf, Marco Mongillo, Rosario Rizzuto, and Tullio Pozzan. Looking forward to seeing calcium. *Nature reviews. Molecular cell biology*, 4(7):579–586, 2003.
- [81] Michael J Rust, Mark Bates, and Xiaowei Zhuang. Sub-diffraction-limit imaging by stochastic optical reconstruction microscopy (STORM). *Nature methods*, 3(10):793–5, oct 2006.
- [82] Edward S. Ruthazer and Hollis T. Cline. Insights into Activity-Dependent Map Formation from the Retinotectal System: A Middle-of-the-Brain Perspective. *Journal of Neurobiology*, 59(1):134–146, 2004.

Bibliography

- [83] R Salomé, Y Kremer, S Dieudonné, J-F Léger, O Krichevsky, C Wyart, D Chatenay, and L Bourdieu. Ultrafast random-access scanning in two-photon microscopy using acousto-optic deflectors. *Journal of neuroscience methods*, 154(1-2):161–74, jun 2006.
- [84] Giovanni Sena, Zak Frentz, Kenneth D Birnbaum, and Stanislas Leibler. Quantitation of cellular dynamics in growing Arabidopsis roots with light sheet microscopy. *PloS one*, 6(6):e21303, jan 2011.
- [85] C.J.R. Sheppard and A. Choudhury. Image Formation in the Scanning Microscope. *Optica Acta: International Journal of Optics*, 24(10):1051–1073, oct 1977.
- [86] Hiroshi Shibasaki and Mark Hallett. What is the Bereitschaftspotential? *Clinical Neurophysiology*, 117(11):2341–2356, nov 2006.
- [87] O Shimomura, F H Johnson, and Y Saiga. Extraction, purification and properties of aequorin, a bioluminescent protein from the luminous hydromedusan, Aequorea. *Journal of cellular and comparative physiology*, 59:223–39, jun 1962.
- [88] H. Siedentopf and R. Zsigmondy. Über Sichtbarmachung und Größenbestimmung ultramikroskopischer Teilchen, mit besonderer Anwendung auf Goldrubingläser. *Annalen der Physik*, 315(1):1–39, 1902.
- [89] L. Silvestri, a. Bria, L. Sacconi, G. Iannello, and F. S. Pavone. Confocal light sheet microscopy: micron-scale neuroanatomy of the entire mouse brain. *Optics Express*, 20(18):20582, 2012.
- [90] Werner Spalteholz. *Über das Durchsichtigmachen von menschlichen und tierischen Präparaten und seine theoretischen Bedingungen, nebst Anhang: Über Knochenfärbung*. S. Hirzel, Leipzig, 1914.
- [91] Kiwamu Tanaka, Sarah J Swanson, Simon Gilroy, and Gary Stacey. Extracellular nucleotides elicit cytosolic free calcium oscillations in Arabidopsis. *Plant physiology*, 154(2):705–19, oct 2010.
- [92] Thai V. Truong, Willy Supatto, David S. Koos, John M. Choi, and Scott E. Fraser. Deep and fast live imaging with two-photon scanned light-sheet microscopy. *Nature methods*, 8(9):160, 2011.
- [93] R. Y. Tsien. A non-disruptive technique for loading calcium buffers and indicators into cells. *Nature*, 290(5806):527–528, apr 1981.
- [94] Roger Y Tsien. New calcium indicators and buffers with high selectivity against magnesium and protons: design, synthesis, and properties of prototype structures. *Biochemistry*, 19(11):2396–2404, may 1980.
- [95] Alexei Verkhratsky and Emil Toescu. *Integrative Aspects of Calcium Signalling*. Plenum Press, New York, oct 1998.
- [96] Tom Vettenburg, Heather I C Dalgarno, Jonathan Nylk, Clara Coll-Lladó, David E K Ferrier, Tomáš Cížmár, Frank J Gunn-Moore, and Kishan Dholakia. Light-sheet microscopy using an Airy beam. *Nature methods*, 11(5):541–4, 2014.

- [97] Nikita Vladimirov, Yu Mu, Takashi Kawashima, Davis V Bennett, Chao-Tsung Yang, Loren L Looger, Philipp J Keller, Jeremy Freeman, and Misha B Ahrens. Light-sheet functional imaging in fictively behaving zebrafish. *Nature Methods*, 11(9):883–884, jul 2014.
- [98] Joshua T Vogelstein, Adam M Packer, Timothy a Machado, Tanya Sippy, Baktash Babadi, Rafael Yuste, and Liam Paninski. Fast nonnegative deconvolution for spike train inference from population calcium imaging. *Journal of neurophysiology*, 104(6):3691–3704, 2010.
- [99] A H Voie, D H Burns, and F A Spelman. Orthogonal-plane fluorescence optical sectioning: three-dimensional imaging of macroscopic biological specimens. *Journal of microscopy*, 170(Pt 3):229–236, 1993.
- [100] P White. Calcium Channels in the Plasma Membrane of Root Cells. *Annals of Botany*, 81(2):173–183, feb 1998.
- [101] Thorsten Wohland, Xianke Shi, Jagadish Sankaran, and Ernst H K Stelzer. Single plane illumination fluorescence correlation spectroscopy (SPIM-FCS) probes inhomogeneous three-dimensional environments. *Optics express*, 18(10):10627–41, may 2010.
- [102] Sébastien Wolf, Willy Supatto, Georges Debrégeas, Pierre Mahou, Sergei G Kruglik, Jean-marc Sintes, Emmanuel Beaurepaire, and Raphaël Candelier. Whole-brain functional imaging with two-photon light-sheet microscopy MiXCR : software for comprehensive adaptive immunity profiling. *Nature Publishing Group*, 12(5):379–380, 2015.
- [103] C Wyart, F Del Bene, E Warp, E K Scott, D Trauner, H Baier, and E Y Isacoff. Optogenetic dissection of a behavioural module in the vertebrate spinal cord. *Nature*, 461(7262):407–410, 2009.
- [104] Rafael Yuste. From the neuron doctrine to neural networks. *Nature Reviews Neuroscience*, 16(8):487–497, jul 2015.